Alpine tectono-metamorphic evolution of the Corsica basement

Journal of METAMORPHIC GEOLOGY

Alpine tectono-metamorphic evolution of the Corsica basement

Journal:	*Journal of Metamorphic Geology*
Manuscript ID	JMG-22-0025
Wiley - Manuscript type:	Original Article
Date Submitted by the Author:	10-May-2022
Complete List of Authors:	Rossetti, Federico; Universita degli Studi Roma Tre Dipartimento di Scienze Cavazza, William; Universita degli Studi di Bologna Dipartimento di Scienze Biologiche Geologiche ed Ambientali Vincenzo, Gianfranco Di; Istituto di Geoscienze e Georisorse Consiglio Nazionale delle Ricerche Lucci, Federico; Universita degli Studi di Bari Aldo Moro Dipartimento di Scienze della Terra e Geoambientali THEYE, Thomas; Universitat Stuttgart Institut fur Anorganische Chemie
Keywords:	Crustal shortening, low-grade metamorphism, Ar-Ar geochronology, Alpine orogeny, Corsica

Alpine tectono-metamorphic evolution of the Corsica basement

Federico Rossetti[1,*], William Cavazza[2], Gianfranco Di Vincenzo[3], Federico Lucci[4], Thomas Theye[5]

[1]Dipartimento di Scienze, Università Roma Tre, Roma, Italy

[2]Dipartimento di Scienze Biologiche, Geologiche e Ambientali, Università degli Studi di Bologna, Bologna, Italy

[3]Istituto di Geoscienze e Georisorse, CNR, Pisa, Italy

[4]Dipartimento di Scienze della Terra e Geoambientali, Università degli Studi di Bari "Aldo Moro", Bari, Italy

[5]Institut für Anorganische Chemie, Universität Stuttgart, Stuttgart, Germany

Running title: Alpine tectonics of the Corsica basement

Corresponding Author:
Federico Rossetti
Dipartimento di Scienze
Sezione di Scienze Geologiche
Università Roma Tre
Largo S. L. Murialdo, 1
00146 Roma (ITALY)
Phone: +390657338043
FAX: +390657338201
e-mail: federico.rossetti@uniroma3.it

Abstract

The Alpine orogenic edifice of Corsica (northern Tyrrhenian Sea) offers the possibility to investigate the mode through which continental crust responds to the propagation of regional shortening at convergent plate margins. The geology of Corsica has been traditionally described separating domains affected by the Alpine tectonism (Alpine Corsica) from those that did not experience the Alpine tectono-metamorphic overprint (Hercynian Corsica), but recent studies show that most of Hercynian Corsica was thermally reset in post-Eocene times, questioning this scheme. The continental units formed at the expenses of the stretched continental margin of the European plate and consist of Hercynian granitoid basement rocks and cover sequences (Permian volcaniclastics and Mesozoic sedimentary successions). By integrating meso- and micro-structural investigations with metamorphic thermobarometry and Ar-Ar geochronology along seriate structural transects running across the basement section exposed below the Alpine orogenic wedge, we document middle-late Eocene (ca. 50-33 Ma) westward-verging syn-metamorphic (low-grade blueschist facies) thick-skinned, basement-involved thrusting. Significantly, crustal shortening in the continental basement predated of ca. 15-10 Ma the subduction zone metamorphism in the oceanic-derived Schistes Lustrés Complex. When the P-T-t-deformation history as reconstructed from the Corsica basement is integrated with the regional scenario of the Alpine-Apennine orogeny, a tectonic reconstruction is proposed framing the Alpine orogeny in Corsica within the Apennine-Maghrebian subduction system in the retroside (retrowedge) of the Apennine orogenic wedge.

Key words: Crustal shortening, low-grade metamorphism, Ar-Ar geochronology, Alpine orogeny, Corsica

1. Introduction

The mode and timing through which regional convergence is accommodated in the continental crust are key issues to define how orogenic processes and continental accretion occur in space and time. At crustal scale, tectonic shortening can be accommodated through uniform thickening (pure-shear deformation mode) or underthrusting (simple shear deformation mode; e.g. Allmendinger and Gubbels, 1996). Both thin- (basement not involved) and thick-skinned (basement-involved) structural styles are recognized in active and fossil orogenic belts (e.g., Allmendinger and Gubbels, 1996; Pfiffner, 2006), with implications on continental rheology (e.g., Babeyko and Sobolev; 2005; Mouthereau et al., 2013; Lowry and Marta Pérez-Gussinye, 2011; Lacombe and Bellhasen, 2016) and the geodynamics at convergent plate margins (e.g., Nemčok et al., 2013; Lacombe and Bellhasen, 2016).

As a part of the Eurasia paleomargin during the Alpine Cenozoic convergence processes involving the Eurasian, Iberian and African plates, the island of Corsica in the northern Tyrrhenian Sea (Fig. 1a) (e.g., Faccenna et al., 2001; Rosembaum et al., 2002; Lacombe and Jolivet, 2005; Handy et al., 2010; Molli and Malavieille, 2010; Carminati et al., 2012; Turco et al., 2012; Malusà et al., 2015; Jolivet et al., 2021) is an ideal case study to investigate how the continental lithosphere responds to propagation of regional shortening at convergent plate margins. Plate convergence along the western end of the Alpine orogen and subsequent rifting and drifting has exposed on the island of Corsica a wide swath of crystalline basement complex originally covered by the Alpine orogenic wedge (Jolivet et al., 1990; 1998; Molli and Malavieille, 2010; Vitale Brovarone et al., 2013; Rossetti et al., 2015; Di Rosa et al., 2020a). This has made possible observation on shortening-related structures underlying the Alpine orogenic wedge.

The geology of Corsica has been classically described separating domains affected by the Alpine tectonism (Alpine Corsica) from those that did not experience the Alpine tectono-metamorphic overprint (Hercynian Corsica) forming the foreland of the Alpine orogen as a part of the European plate (e.g. Duran Delga, 1984; Rossi et al., 1994; Vitale Brovarone et al., 2013) (Fig. 1b). This simplistic subdivision contrasts with the available thermo-chronometric data (Cavazza et al., 2001; Zarki-Jhaki et al., 2004; Fellin et al., 2006; Danisik et al., 2007), which document that most of the Hercynian Corsica was thermally reset, demonstrating that virtually all the island was covered by the Alpine orogenic wedge and/or by foreland basins (Fig. 1c).

While the Alpine tectono-metamorphic evolution of the Mesozoic-Cenozoic cover rocks of the former European continental margin has been recently assessed (Di Rosa et al., 2019, 2017;

2020a; Malasoma et al., 2020; Marroni et al., 2020), the structural style, timing and thermo-baric environments of the Alpine deformation in the Hercynian continental basement is still poorly documented, despite a mounting body of structural, petrographic and geochronological evidence of Alpine tectonism (Malasoma et al., 2006; 2019; Malasoma and Marroni, 2007; Garfagnoli et al., 2009; Di Vincenzo et al., 2016; Di Rosa et al., 2017; 2020b; Frassi et al., 2022). Deciphering the pressure-temperature-time-deformation (P-T-t-d) history of the Corsica basement during the Alpine orogeny is essential to frame in a coherent scenario the Alpine tectonic/geodynamic evolution in the hinterland of the Alps-Apennine (see Vitale Brovarone and Herwatz, 2013).

In this study, we describe a coherent set of Alpine-age tectono-metamorphic structures affecting both Alpine and Hercynian Corsica, as traditionally defined (Figs. 1b and 2). We describe an early-late Eocene (50-33 Ma) westward-verging syn-metamorphic thick-skinned, basement-involved thrusting. Implications of these results are framed within the regional scenario of the Alpine-Apennine orogenic system.

2. Geological background

Corsica Island is a fragment of the former southern continental margin of the Eurasia plate, involved first in the formation of the Alpine convergent margin during consumption of the Mesozoic Alpine Tethys (Ligurian–Piedmont branch) oceanic realm and successively in the Oligocene-Miocene rifting and drifting processes leading to opening of the Liguro-Provençal and Tyrrhenian back-arc basins (Doglioni et al., 1997; Rosembaum et al., 2002; Carminati et al., 2012; Faccenna et al., 2001; Lacombe and Jolivet, 2005; Molli and Malaiveille 2010).

The Alpine orogenic construction caused the formation of a west-verging (present-day coordinates) orogenic wedge (Fig. 2), formed at the expenses of both the ocean-derived and the former continental margin units, thrusted onto the Hercynian Corsica (Vitale Brovarone et al., 2013; Di Rosa et al., 2002; Jolivet et al., 1990; Molli et al., 2006; Rossetti et al., 2015). The nappe edifice consists, from top to bottom, of (i) non-metamorphic or slightly metamorphosed ophiolite units (Balagne, Nebbio and Macinaggio units), (ii) high-pressure (eclogite to blueschist facies) subduction channel units of the Schistes Lustrés Complex, a tectonic mélange made of oceanic- and continental units, and (iii) European continental crust tectonic slices, made of the Tenda and the external continental units (Durand Delga, 1984; Jolivet et al., 1990; Vitale Brovarone et al., 2013; Di Rosa et al., 2020a). The latter complex of units, also referred to as Lower units, consists of various tectonic slices made of Permian-Carboniferous igneous rocks intruded into Pan-African

metamorphic host rocks, unconformably covered by Permian volcanics and volcaniclastic deposits (Rossi et al., 1994; Paquette et al., 2003; Di Rosa et al., 2020b) and by Mesozoic to Eocene sedimentary successions (e.g., Bezert and Caby, 1988; Rossi et al., 1994; Cavazza et al., 2018; Di Rosa et al., 2020a). These continent-derived tectonic slices are affected by a diffuse Alpine tectono-metamorphic overprint, with peak conditions equilibrated within the low-grade blueschist metamorphic facies (Tribuzio and Giacomini, 2002; Molli et al., 2006; Maggi et al., 2012; Rossetti et al., 2015; Di Rosa et al., 2019).

The age of subduction zone HP/LT metamorphism is constrained is late Eocene (ca. 37-34 Ma), based on U-Pb zircon (Martin et al., 2011) and Lu-Hf garnet and lawsonite (Vitale Brovarone and Herwatz, 2013) dating of the eclogite- and blueschist facies rocks of the Schistes Lustrés Complex. A minimum late Eocene age (35 Ma) is also indicated by Ar-Ar phengite geochronology from the Schistes Lustrés Complex (Brunet et al., 2000). The tectonic assembly of the ophiolite domain units onto the Hercynian Corsica is primarily constrained by the activity of the ductile-to-brittle East Tenda Shear Zone (ETSZ), the Alpine shear zone boundary between the continental margin of the European plate and the Ligurian-Piedmont ocean. The ETSZ experienced a polyphase tectono-metamorphic evolution, typified by syn-blueschist top-to-the-W thrusting, overprinted by ductile-to-brittle top-to-the-E extension (Gibbons and Horak, 1984; Jolivet. et al., 1990; Gueydan et al., 2003; Maggi et al., 2014; Molli et al., 2006; Rossetti et al., 2015; Beadouin et al., 2020). Most of the available geochronological data on the syn-blueschist shear zones clusters in the latest Eocene-earliest Oligocene (35-32 Ma; Ar-Ar phengite geochronology: Brunet et al., 2000; Beaudoin et al., 2020; Rb-Sr geochronology: Rossetti et al. 2015), considered as the age of the terminal Alpine overthrusting (Brunet et al., 2000; Rossetti et al., 2015; Beadouin et al., 2020). Older U-Pb rutile ages (ca. 54 ± 8 Ma; Maggi et al. 2012), together with the maximum Ar-Ar phengite ages (ca. 45 Ma; Brunet et al., 2000), suggest an early Eocene stage for the ETSZ nucleation. The post-orogenic top-to-the-E reactivation of the ETSZ culminates during the early Miocene, synchronously with syn-greenschist extensional shearing in the Schistes Lustrés (Rossetti et al., 2015).

Tectono-metamorphic data from the frontal, N-S striking thrust zone bounding the contact zone between the oceanic-derived Alpine nappe stack and Hercynian Corsica (here after referred to as Alpine deformation front, ADF; Fig. 2) document a polyphase evolution in the metasedimentary cover units of the Corsica basement, associated with a progressive top-to-the-west ductile-to-brittle shearing, equilibrated under low-grade blueschist to greenschist facies conditions (Di Rosa et al., 2019; 2020a-b). Significantly, distinct pressure–temperature-

deformation histories characterize the different tectonic units, indicating different burial and exhumation trajectories during the crustal slicing associated with the overthrusting of the Schistes Lustrés Complex onto the European plate margin (Di Rosa et al., 2019). Petro-tectonic evidence has shown that Alpine deformation and low-grade greenschist to blueschist metamorphism have also affected the Hercynian granitoid basement of Central Corsica, in the footwall of the main Alpine contact (Garfagnoli et al., 2009; Malasoma and Marroni, 2006; Di Vincenzo et al, 2016). Di Vincenzo et al. (2016) documented late Eocene (ca. 37-35 Ma) high-angle, NS-striking mylonitic shear zones, developed under P-T conditions of ≥300 °C and 0.5-0.6 GPa, and attributed to Alpine strike-slip reactivation of the Hercynian basement. ^{40}Ar-^{39}Ar minimum ages of ~46 Ma from microstructurally muscovite relics were also assigned to the Alpine tectono-metamorphic evolution (Di Vincenzo et al, 2016).

Biostratigraphic data from the Corsica continental margin cover units constrain the Alpine orogenic tectonics to pre-Priabonian (>38 Ma) (Ferrandini et al., 2010) times, although post-Bartonian (<38 Ma) deformation was also reported (Bezert & Caby, 1988). An upper age limit for the ductile Alpine tectono-metamorphic evolution is provided by the sedimentation of the early Miocene deposits of the Saint Florent and Francardo Basins, sealing the early thrust contacts (Dallan & Puccinelli, 1995; Ferrandini et al., 1998; Cavazza et al., 2001). This is in line with the available thermochronological data, indicating exhumation of the deep roots of the Alpine orogen during the late Eocene-Miocene (Fellin et al., 2006 Cavazza et al., 2001; Zarki-Jakni et al., 2004; Danisik et al., 2007).

3. Materials and Methods

We investigated the structural architecture and the tectono-metamorphic signature of the continental basement of central Corsica along three seriate E-W trending geological transects (transect-1 to -3), running across the ADF into the easternmost portion of the Hercynian basement complex (Fig. 2), with the aim to compare structures and provide ultimate thermobaric and geochronological constraints on the tectono-metamorphic coupling between Alpine and Hercynian Corsica. The geology of the study area is presented in Di Rosa et al. (2017; 2020a) and Malasoma et al. (2020), where the structural architecture of the tectonic boundary zone between the Schistes Lustrés and the external continental units is detailed. We focus our study exclusively on the Hercynian basement units (Hercynian granitoids and Permian volcanic deposits) either

exposed at the footwall or in the immediate hanging wall of the ADF (transect-1 to -3 in Fig. 2). The hanging wall units define the so-called Corte slices (Di Rosa et al., 2019, 2020a).

The research rationale is based on a multidisciplinary approach that combines field-based, meso- and micro-structural investigation with metamorphic thermobarometry (inverse and forward modelling tecniques) and Ar-Ar geochronology. Samples for laboratory work were collected based on the textural and mineralogical evidence at the outcrop scale. Table 1 reports the location, textures and petrography of the studied samples. Appendix-A details the analytical protocols and methods adopted in the study. In the following, mineral abbreviations follow Whitney and Evans (2010), complemented by Wm for white mica.

4. Structures in the field

This section describes the structural architecture along the three geological transects and detail the tectono-metamorphic setting of the sampling sites. Transect-1 and transect-2 illustrate the deformation structures across the ADF entering Hercynian Corsica, whilst transect-3 is located exclusively within the Hercynian basement complex (Fig. 2).

4.1 Transect-1

Structure in the Lower units (here made of the Castiglione Popolasca unit; Di Rosa et al., 2020a) is characterized by a stack of west-verging ductile-to-brittle thrust slices that involve the Hercynian granitoid rocks and its Permian volcaniclastic covers. Overall, a tectonic doubling of the stratigraphic column is documented. Eocene metabreccias, unconformably covering the basement rocks, are also involved in the compressional deformation (see also Di Rosa et al., 2019) (Fig. 3a). Moving from west to east, a marked increase in the deformation intensity is observed in the Permian volcaniclastics in a transition from D_1 to D_2 deformation (Figs. 3a-b). To the east, the main structural fabric is a penetrative, sub-vertical S_1, NNW-SSE striking (N02°, 83°; n=19) metamorphic foliation that transposes the S_0 layering (S tectonites). The S_1 foliation is axial planar to upright isoclinal folds with sub-horizontal hinge lines, trending sub-parallel to the S_1 foliation (N353°, 18; n= 23). The L_1 lineations, defined by Qz-Wm alignments, are poorly evident but systematically trend down-dip (Fig. 3b-d). The S_1 foliation is deformed by a spaced D_2 crenulation cleavage defined by a S_2 foliation trending sub-parallel to S_1 and shallowly dipping to the east (N353°, 19°; n=16) (Figs. 3d). To the west, the intensity of the D_2 deformation increases in the Permian

volcaniclastics structurally lying below the Hercynian granitoids. There, the S_0 foliation is transposed by S_1 and progressive transition from east-dipping S_2 crenulation to shear foliation is observed, with development of a ca. 100 m thick panel of S-L and S-C tectonites, dipping shallowly (ca. 30°) to the east (S_2 mean strike: N01°, 27°, n= 56). The L_2 stretching lineations are dip-parallel (N81°, 28°; n=56), and made of Qz-Wm alignments. This shear zone separates two tectonic slices of Hercynian granitoids (Figs. 3a-b, e). The sense of shear is systematically top-the-W as documented by the S-C fabric and the asymmetry of F_2 intrafoliar folds (Fig. 3e).

The Hercynian granitoid rocks below the major tectonic contact dominantly show primary equigranular texture. Brittle deformation structures are widespread and mostly characterized by conjugate sets of sub-vertical NE-SW and NW-SE striking fault systems and joints, with mutual cross-cutting relationships. Slickenlines, dominantly defined by wear and abrasion tracks, are either sub-horizontal or dip-parallel (Fig. 3b). Shear criteria, as provided by synthetic Riedel shears, grooves and abrasion structures, indicate dextral-reverse and sinistral-reverse kinematics for the NE-SW and NW-SE striking fault systems, respectively. These fault systems overprint subparallel discrete (up to 5-meter-thick) anastomosing zones of ductile shearing (mylonites and protomylonites; Fig. 3f-g) that are observed up to ca. 4 km from the ADF. Such ductile zones of shearing bear oblique stretching lineations, provided by Qz-Wm mica alignments. Shear criteria as dominantly provided by S-C fabrics and sigma-type porphyroclasts (quartz and K-feldspar) document dextral-reverse and sinistral-reverse kinematics for the NE-SW and the NW-SE striking shear zones, respectively (Figs. 3b, f-g). Significantly these ductile shear zones are observed in sites of extensive structurally controlled fluid flow as documented by a pervasive network of syn-metamorphic veining and marked alteration halos. The vein filling is dominantly made of Qz-Wm ± Cb, whilst the alteration halos consists of Wm-Stp-Ep-Ttn±Amp (see below) (Fig. 3h).

4.2 Transect-2

Transect-2 runs across the tectonic contacts between the Schistes Lustrés Complex and the Lower units (here made of the Ghisoni unit; Di Rosa et al., 2020a) and between the latter and the Hercynian basement (Figs. 2 and 4a). The contact between the Schistes Lustrés and the Lower units is marked by a dm-thick cataclastic zone striking NNW-SSE, dipping steeply to the ENE. Entering the Lower units, a NNW-SSE striking S_1 sub-vertical foliation is observed in the Permian volcaniclastics. Moving towards the west, the Permian volcaniclastics are in tectonic contact with slightly deformed granitoid rocks, where an incipient subhorizontal, shallowly SE-dipping

secondary foliation is observed (CO34 in Fig. 4a). Farther west, isotropic primary igneous fabrics are predominant within the granitoid rocks. Major ductile shear localisation occurs ca. 3 km west of the fault-controlled contact between the Schistes Lustrés and the Lower units. Here, a ca. 50 m thick zone of ductile shearing is defined by strongly mylonitized granitoids with a gneissic texture, where porphyroclastic Qz-Ksp aggregates occur within a fine-grained white mica matrix (Sample CO36 in Fig. 4). Finite deformation (D_2) is partitioned between domains of coaxial and non-coaxial shearing, which deform an early-formed, east-dipping sub-vertical S_1 foliation (Fig. 4b). S_2 foliation dips shallowly towards the east (mean: N08°, 31°; n= 32), bearing dip-parallel L2 stretching lineations (N78°, 32°; n=32) defined by Qz-Wm aggregates. The sense of shear, as deduced by the S-C fabric, sigma-type porphyroclasts and fold asymmetry is systematically top-to-the-W (Figs. 4c-d). To sum-up, the reconstructed structural architecture along Transect-2 documents a major tectonic doubling of the continental basement units, with major shear strain localization along the contact between the Hercynian granitoids and the Permian volcaniclastics (Fig. 4a).

4.3 Transect-3

Transect-3 runs along the Défilé de l'Inzecca, across the same tectonic units described in Transect-2. The basement section was already studied by Garfagnoli et al. (2009). Its structural architecture is dominated by a penetrative sub-vertical D_1 plano-linear fabric with formation of S-L tectonites that almost completely obliterate the primary igneous fabric in both the Hercynian granitoids and the Permian volcaniclastics (Fig. 5a). The S_1 foliation strikes NNW-SSE, dipping steeply either to ENE or WSW (mean: N153°, 83°; n=52), and bears dip-parallel L_1 stretching lineations (mean: N252°, 81°; n=42; Figs. 5b), dominantly made of Qz-Wm associations in gneiss and Ab-Ep in volcanoclastics. A gneissic texture is well evident in the granitoid rocks, defined by Qz-Fsp porphyroclast embedded within Wm folia. In section normal to foliation and parallel to the stretching lineations, cm-sized Qz and Fsp porphyroclasts systems dominantly show phi-type geometries and both up- and down-dip kinematic criteria (dominantly provided by sigma-type clasts) are present, attesting dominant coaxial stretching during formation of the composite S_1-L_1 fabric (Figs. 5c-d). In the Permian volcaniclastics, the D_1 fabric consists of S_1-L_1 tectonites that overprint the primary layering. Vertical stretching is documented by L_1, dip-parallel stretching lineation as provided by Qz-Pl-Ep associations, boudinage and nearly horizontal quartz veining. The S_1 foliation is axial planar to subvertical isoclinal folds with sub-horizontal hinge lines, trending ca. NS (Figs. 5b-g). Various generations of quartz veins are recognized, with early segregated veins

289 that are transposed along the S_1 foliation. A spaced S_2 crenulation foliation is observed to refold
290 the S_1 foliation. The S_2 strikes ca. N-S and dips shallowly to the E (Fig. 5b). As documented by the
291 decrease in the S_2 spacing, the intensity of the S_2 crenulation increases when moving to the E,
292 towards the contact with the Schistes Lustrés Complex (Fig. 5a, h)
293

294 ## 5. Sample microtexture and petrography

295 Microstructures, petrography and mineral chemistry of representative samples collected
296 along the three investigated samples are described below. Further details on microstructures are
297 provided in Supplementary Material#1. Mineral chemistry as obtained from electron microprobe
298 analyses (EMPA), and the recalculation of the mineral formulas are provided in the Supplementary
299 Material#2.
300

301 ### *5.1 Transect-1*

302 Sample CO24 is representative of the S_1 fabric in the Permian volcaniclastics (Fig. 3a, 3d-c).
303 The sample microfabric is characterized by a penetrative disjunctive foliation, defined by the syn-
304 kinematic assemblage made of aligned Wm (up to 40% vol.) and fine-grained re-crystallized Qz (in
305 higher strain domains), Ab, ± Stp ± Rt, which envelopes up to mm-sized Qz and Fsp porphyroclasts
306 (Fig. 6a, 7a). Fracturing of Qz-Fsp porphyroclasts is commonly observed with fracture sealing
307 largely operated by recrystallized Qz ± Wm. Residual igneous microstructures are commonly
308 observed, as documented by preserved twinning in Kfs, oscillatory growth zoning in Pl and
309 euhedral shapes of the Qz-Fsp grains. Pristine igneous quartz grains show undulatory extinction
310 and evidence of dynamic recrystallisation, dominantly assisted by bulging recrystallisation. Post-
311 tectonic growth of Cb (ca. 1-2% vol.) is also commonly documented (Supplementary Material#1).
312 The Wm (n=36) composition is characterized by Si ranging 3.34-3.49 atoms per formula unit
313 (apfu), corresponding to X_{Ms} = 0.41-0.57, X_{Cel} = 0.37-0.51, X_{Prl} <0.10, X_{Pg}<0.11 (Fig. 8a, d-e;
314 Supplementary Material#2).
315 Sample CO25 is a D_2 S-C tectonite, representative of the progressive shear strain localization
316 in the Permian volcaniclastics (Table 1; Fig.3a, e). At the thin section scale, the syn-metamorphic
317 fabric is transpositive and characterized by a significant increase in Wm abundance (up to 70 vol%,
318 associated with a very fine-grained (average 10 μm) matrix made of recrystallized Qz (Fig. 6b). Shear
319 sense criteria are provided by oblique foliation, sigma-type Fsp porphyroclasts and S-C fabrics and
320 systematically indicate a top-to-the-W sense of shear (Fig. 6b). The metamorphic assemblage is

completed by Chl (ca. 10 %vol), Ab, Ep, Stp, Ttn, Ap (< 5% vol). Stp is observed as mostly unoriented clusters of elongated crystals and along the S_1 foliation. Chl form late clusters in association with Ttn, Ep, Ap, often forming pseudomorphic replacement at the expenses of former igneous grains (Fig. 7b). Post-tectonic growth of Cb is also observed. The composition of the syn-tectonic Wm (n=30) shows Si ranging 3.34-3.51 apfu, corresponding to X_{Ms} = 0.47-0.64, X_{Cel} = 0.34-0.51, X_{Prl} <0.02, X_{Pg}<0.05 (Fig. 8d-e). The composition of Stp is characterized by X_{Mg} = 0.13 and $X_{Fe^{3+}}$ [$(Fe^{3+}/(Fe^{3+}+Fe^{2+})$] = 0.35. Ep shows X_{Ps} [$Fe^{3+}/(Fe^{3+}+Al^{3+})$] =0.35 with Mn^{3+} 0.03 apfu, and Chl is characterized by Si ranging 2.76-2.91 apfu and XMg between 0.23-0.27 (Supplementary Material#2).

Samples CO38 and CO55 are protomylonites, representative of the ductile shear strain localization in the Hercynian granitoid basement (Table 1; Fig. 3a). At thin section scale, sample microtextures are characterized by a network of anastomosing array of inter- and intra-grain fracture network affecting the igneous Fsp-QZ matrix, coexisting with spaced bands (up to 150 μm in thickness) of ductile shear strain localization (Fig. 6c). The crack-filling mineral assemblage dominantly consists of Qz ± Wm ± Stp and late Cb (Fig. 7c). The vein selvage is made of Bt-Chl-Ttn ± Cb, Amp, Ep, Ab, Ap associations. Quartz in veins either preserve fibrous textures or document evidence of dynamic recrystallization and grain size reduction, primarily assisted by bulging recrystallisation. Igneous quartz exhibits undulose extinction, deformation bands, sub-grain formation and core-mantle structures indicative of subgrain rotation recrystallisation (Fig. 6c; Supplementary Material#1). Replacement of igneous Mag by the assemblage made of stilpnomelane-amphibole-epidote-titanite ± ilvaite after igneous magnetite is also observed (Fig. 7d). The ductile shear bands are defined by anastomosed fine-grained recrystallized Qz in association with Wm ± Stp (Fig. 6c). The Wm is entirely syn-kinematic and commonly oriented parallel to the mylonitic foliation (Fig. 6c). It occurs in two generations: (i) the Wm1 (n=6), represented by a minor cluster of cores with lower Si (3.26-3.33 apfu) corresponding to X_{Ms} = 0.49-0.61, X_{Cel} = 0.27-0.34, X_{Prl} <0.17, X_{Pg} < 0.01; and (ii) the Wm2 (n=14), forming rims of Wm1 and main foliation, which show higher Si (3.35-3.50 apfu) and corresponding to X_{Ms} = 0.38-0.60, X_{Cel} = 0.36-0.50, X_{Prl} <0.11, X_{Pg} < 0.02 (Fig. 8d-e; Supplementary Material#2). The Stp composition is characterized by X_{Mg} = 0.24-0.33 and X_{Fe3+} = 0.38-0.45 apfu. Chl shows X_{Mg} =0.20 and Bt is characterized by TiO_2= 0.55-0.92 wt% with X_{Mg} = 0.24-0.25. The Amp shows low Al_2O_3 (1.07-1.29 wt.%), low CaO (6.38-7.09 wt%), high FeO^t (20.99-21.04 wt.%) and Na_2O (3.19-3.31 wt.%), belonging to the sodic-calcic group with a chemical composition corresponding to Wnc (Hawthorne et al., 2012) (Supplementary Material#2).

353

354 ***5.2 Transect-2***

355 Sample CO35 is from a fractured granitoid (Table 1). The fracture network is dominantly
356 inter-grain, with up to 0.5 cm alteration halos, making up to 30% vol. of rock. The fracture filling is
357 dominantly made of Qz-Wm, with associated Stp-Ep-Amp-Ttn-Ab + Grt, Ap. Two generation of
358 metamorphic Wm are documented both in the metamorphic matrix and as vein segregation (Fig.
359 7e). Wm1 (n=8) represents cores showing low Si (3.05-3.29 apfu) and corresponding to X_{Ms} = 0.68-
360 0.89, X_{Cel} = 0.06-0.29, X_{Prl} <0.02, X_{Pg} < 0.03. The Wm2 (n=19) consists of rims and overgrowth,
361 fracture filling and main foliation. Wm2 has higher Si (3.41-3.59 apfu) corresponding to an increase
362 of celadonite compound: X_{Ms} = 0.40-0.56, X_{Cel} = 0.42-0.59, X_{Prl} <0.02, X_{Pg} < 0.02 (Fig. 8d-e;
363 Supplementary Material#2). Metamorphic Ep is observed to rim early igneous All and Mag, in
364 association with Grt and late Amph (Figs. 7f). Ep shows Fe^{3+} ranging 0.89-1.19 apfu and Mn^{3+} 0.01-
365 0.04, respectively, corresponding to X_{Ps} = 0.30-0.40. Grt is essentially an Adr-Grs ($Adr_{55-78}Grs_{22-38}$)
366 solid solution. The low Si content and low total indicate the presence of hydrogarnet component.
367 Stoichiometric constraints result in 5 to 10% of SiO_4 tetrahedra being replaced by $(OH)_4$. The Amp
368 chemistry corresponds to Na-Amp (Rbk; Supplementary Material#2)

369 Sample CO36 is representative of the D2 mylonitic shear fabrics in the Hercynian granitoids
370 (Table 1; Fig. 4). The syn-tectonic mineral assemblage consists of Qz-Wm-Stp-Ep, Ttn, Ab. Texturally
371 late fibrous Amp crystallization and post-tectonic Cb growth are also observed. The microtexture is
372 dominated by a fine-grained aggregate of recrystallized Qz grains (up to 40% vol.), associated with
373 syn-tectonic Wm that wrap around and rim Qz-Fsp porphyroclasts and crenulated Wm microlithons
374 (Fig. 6d). Fsp grains are extensively affected by intragranular fractures that are filled by recrystallized
375 quartz. Relic igneous quartz grains show evidence of pronounced undulose extinction, distinct
376 subgrains and core-mantle structures indicative of subgrain rotation recrystallisation
377 (Supplementary Material#1). Shear senses are dominantly provided by oblique foliation and sigma-
378 type Fsp-Qz porphyroclasts, systematically pointing to top-to-the-W shearing (Figs 6d-e). Similarly
379 to sample CO-35, two generations of metamorphic Wm is commonly observed (Fig 7g-h). The Wm1
380 (n=11) forms the cores showing low-Si (3.02-3.32 apfu) and corresponding to a muscovitic
381 composition (X_{Ms} = 0.62-0.90, X_{Cel} = 0.03-0.32, X_{Prl} <0.02, XPg < 0.12) (Fig. 8a-b). The Wm2 (n=26)
382 overgrowths Wm1 and defines the main foliation. The Wm2 shows higher Si (3.35-3.58 apfu),
383 corresponding to X_{Ms} = 0.39-0.62, X_{Cel} = 0.36-0.58, X_{Prl} <0.04, X_{Pg} < 0.01(Fig. 8b, d-e; Supplementary
384 Material#2). The Stp composition is characterized by XMg = 0.31-0.36 and XFe3+ = 0.41-0.47 apfu

(Supplementary Material #2c). Epidote is characterized by high Fe^{3+} (0.75-0.95), with X_{Ps} = 0.25-0.32. The Amp corresponds to Act compositions (Supplementary Material#2).

5.3 Transect-3

Sample CO42 is representative of the D_1-D_2 composite fabric in the Hercynian granitoids (Table 1; Fig. 5). The sample microfabrics is dominated by a continuous foliation (S_1) made of alternating fine-grained recrystallized Qz grains and Wm folia that envelop fractured Fsp and highly strained Qz porphyroclast systems (Fig. 6f). Early igneous quartz grains show evidence of pronounced internal strain and recovery, as documented by ondulose extinction, deformation bands and subgrain formation. Dynamic recrystallisation is dominantly documented by core-and-mantle structures, defined by fine-grained quartz aggregates surrounding large relic quartz grains produced by sub grain rotation recrystallisation (Supplementary Material#1). Shear sense indicators are not univocal, confirming the dominant coaxial nature of D_1 deformation as observed at the mesoscale (Fig. 5c). Igneous textures are locally preserved. The syn-tectonic mineral assemblage consists of Wm-Qz- Ab-Stp-Amp + Ep, Ttn, and Ap. Late Cb growth is also observed (Fig. 7i). Wm composition (n= 66) is characterized by Si ranging 3.47-3.61 apfu, corresponding to X_{Ms} = 0.26-0.45, X_{Cel} = 0.47-0.61, X_{Prl} <0.13 and negligible XPg (<0.01) (Figure 8c-d; Supplementary Material#2). Stp shows X_{Mg} = 0.25-0.41 and $X_{Fe^{3+}}$ = 0.35-0.48. Ep shows X_{Ps}=0.14-0.19 with Mn^{3+} < 0.02 apfu. A two-stage Amp crystallization is documented, with Ca-Na-Amph (Wnc) replacing early segregated Na-Amp (Rbk) (Supplementary Material#2).

6. Metamorphic Thermobarometry

The thermo-baric environment during syn-metamorphic deformation of the Hercynian basement of Corsica was assessed through phase equilibria (pseudosection) modelling by using the software Perple_X (Connolly, 2005; https://www.perplex.ethz.ch/, version 6.9.1 updated on March 07 2022). We used the bulk composition of samples CO24, CO36 and CO42, which are considered representative of the different textures associated with development of the composite D_1-D_2 fabric along the three investigated transects (Fig. 2). The bulk sample compositions were simplified to the Na_2O–CaO–K_2O–FeO–MgO–Al_2O3–SiO_2–H_2O–TiO_2–O_2 (NCKFMASHTO) system by removing MnO (0.01-0.05 wt%) and correcting CaO for the presence of apatite and post-tectonic calcite (up to 1-2 % vol. in some samples). This procedure completely removes CaO from sample CO24, and only leaves small amounts of CaO in samples CO36 and CO42 (Table 2). We adopted the

hp633ver.dat thermodynamic dataset (Holland & Powell, 2011; 2018), and the following solid solution models as described in the file solution_model.dat: Bi(W) for biotite, Chl(W) for chlorite, Mica(W) for white mica (White et al., 2014), Ep(HP11) for epidote (Holland & Powell 2011); cAmph(G) for clinoamphibole (Green et al., 2016), feldspar for ternary feldspar (Fuhrman & Lindsley, 1988), Sp(WPC) for spinel (White et al., 2002), Pu for pumpellyite, and Stlp for stilpnomelane. Quartz, ilmenite, rutile, and titanite were considered as pure phases. The fluid phase was considered as pure H_2O and considered to be present in excess.

We are aware that solid solution models for complex minerals such as mica or amphibole are poorly known at low T, with particular reference to the role of Fe^{3+} content in silicate minerals. For stilpnomelane solid solution model, ferric iron is not even considered. In case of amphiboles, the applied solid solution model fails to predict the analyzed compositions in the considered P-T range, except for riebeckite. As further complication, the contents of Fe^{2+} and Fe^{3+} in minerals are not directly analyzed but calculated from microprobe analyses based on stoichiometric constraints, and are probably of low precision, particularly for white mica, stilpnomelane, and amphibole. In order to estimate the contents of ferric iron of the whole rock compositions, for samples Co36 and Co42 we calculated T-Fe_2O_3 pseudosections (at constant P (0.6 GPa, see below); Supplementary Material#3). Bearing in mind the above-mentioned uncertainties, we consider the results of the thermodynamic modelling as semi-quantitative.

6.1 Sample CO24

Sample CO24 is representative of the thermo-baric environment leading to development of S_1 foliation in the volcanoclastic covers (Figs. 2, 3a, c-d). The mineral assemblage defining the S_1 foliation consists of Qz-Wm + Stp +Rt, which defines a P-T field restricted by the stability of Stp that is limited to high temperature by the Bt-in isograd and to high-pressure by the Stp-out isograds, respectively. Considering the isopleths as defined by the Si content in Wm (3.39-3.49 apfu), the corresponding thermobaric environment is constrained at ca. 0.5-0.6 GPa and T< 350 °C (Fig. 9a).

6.2 Sample CO36

Sample CO36 refers to the D2 progressive shear strain localization in the continental basement (Figs. 2, 4). The syn-tectonic mineral assemblage is made of Qz-Wm-Stp-Ep-Ttn-Ab. Choosing a sectioning value of 0.6 GPa, pseudosection modelling in the T-Fe_2O_3 space indicates

that a low Fe_2O_3 content <0.1 wt.% is required for the stability of the above assemblage. The temperature range is limited between ca. 300-370 °C, as imposed by the lack of Bt and Pmp in the metamorphic assemblage (Supplementary Material#3). A value of Fe_2O_3= 0.1 wt% is therefore considered to construct the P-T pseudosection. Results show that the syn-tectonic metamorphic assemblage made of Wm-Ep-Stp-Ttn occurs within a narrow P-T field of P=0.45-0.65 GPa and T of ca. 300-330°C, as constrained by the absence of Amp at high-pressure and absence of Pmp at lower temperature and Bt at higher temperature, respectively (Fig. 9b).

6.3 Sample CO42

Sample CO42 is representative of the development of the D_1 fabric in the continental basement (Figs. 2, 5). The syn-tectonic mineral assemblage is made of Qz-Wm-Stp-Ep ± Amp, Ttn, Ab. The pseudosection modelling in the T-Fe_2O_3 space at constant P of 0.6 GPa shows that the Stp-Amp-Ep assemblage is stable for 0.3 < Fe_2O_3< <0. 9 wt% at temperatures below 350°C, limited by occurrence of Bt in the metamorphic assemblage at higher temperature and Ep at lower temperature, respectively (Supplementary Material#3). A value of Fe_2O_3= 0. 6 wt% is chosen to construct the P-T pseudosection. Considering the Si isopleths in Wm for this sample (Si apfu ranging 3.50-3.60) and absence of Bt in the metamorphic assemblage, results constrain formation of the S_1 foliation at P=0.5-0.7 GPa and T of ca. 300°C (Fig. 9c).

7. ^{40}Ar-^{39}Ar Geochronology

Laser in-situ analyses were completed on the samples used for pseudosection modelling. White mica of sample CO24 (Transect-1) yielded a significant age interval (Fig. 10), in the range of 37.6±0.5 Ma to 43.6±0.4 Ma. Some older ages, up to ~50 Ma may be due to contamination by K-feldspar, which yielded ages older than 100 Ma where unequivocally identified (Supplementary Material#4). The five younger ages define a weighted mean of 38.0±0.2 Ma. White mica from sample CO36 (Transect-2) gave a younger age interval when compared to white mica from Transect-1, ranging from 32.5±0.2 Ma to 37.8±0.3 Ma. A slightly older age (43.2±1.8 Ma) is affected by a large uncertainty due to the low gas yield, likely due to contamination by a low K phase(s). The first youngest peak in the cumulative plot distribution (Fig. 10) is defined by three analyses, yielding a weighted mean age of 33.3±0.2 Ma. Sample CO42 (Transect-3) gave white-mica ages mainly within 38.6±0.4 to 48.9±0.3 Ma. Some older ages, as old as ~56-60 Ma, analogously to samples CO24, maybe due to contamination by K-feldspar.

8. Discussion

The Alpine tectono-metamorphic evolution reconstructed at the footwall of the ADF is dominated by development of a low-grade, composite D_1-D_2 ductile plano-linear fabric, characterized by the pervasive development of S-L tectonites that transpose the primary fabrics in the Hercynian granitoid basement and the Permian-Triassic volcaniclastic cover.

The D_1 deformation is dominantly attested by formation of a panel of N-S striking subvertical S_1 foliation, sub-parallel to the ADF, and bearing dip-parallel L_1 stretching lineations. Locally, deformation partitioning is documented during development of the D_1 fabrics when moving from the Permian volcaniclastic into the granitoid basement, where conjugate sets of subvertical NE-striking dextral and SE-striking sinistral mylonitic zones are observed to accommodate the D_1 deformation (see also Di Vincenzo et al., 2016; Fig. 3b). Overall, the D1 finite strain documents pure shear dominated deformation fabrics recording subvertical stretching in response to an E-W directed maximum shortening direction. A continuum of deformation is attested by the progressive overprinting of the quartz veins that, formed orthogonally to the L_1 stretching direction, are shortened and folded along the S_1 foliation and later overprinted by new vein generations (Figs. 3c and 5f-h). The D_2 deformation overprints the D_1 fabric in a general regime of simple shear, associated with development of E-dipping foliations and ductile shear zones, accommodating a general top-to-the-W tectonic sense of transport both in the granitoid basement and the Permian volcaniclastic cover. The intensity of the D_2 deformation increases westward approaching the ADF, suggesting a tectonic linkage with the overthrusting of the Alpine Corsica Domain onto the Hercynian Corsica.

When integrated with the available literature data (Garfagnoli et al., 2009; Di Rosa et al., 2020a; Malasoma et al., 2006; 2020), the structural data collected in this study point to a continuum of ductile deformation during the Alpine basement-involved thrusting in the Hercynian Corsica. Shortening in the continental crust was first accommodated by (i) pure-shear dominated strain at deeper crustal levels and then (ii) top-to-the-W shear strain localization, evolving from ductile shearing to brittle overthrusting at shallower crustal conditions. Top-to-the-W thrusting involved also the Mesozoic and Cenozoic cover units (see also Di Rosa et al., 2019; 2020a; this study).

8.1 Metamorphic environment and deformation conditions

Low-T conditions during the progression of the D_1-D_2 deformation makes the assessment of the corresponding thermo-baric environment through thermodynamic modelling challenging. However, considering (i) the occurrence of Stlp and the absence of Bt in the main syn-tectonic assemblage, which limit the thermal peak to < 400°C; and (ii) the Si-in-Ph isopleths as proxy of the burial pressure, we can conclude that Alpine deformation/metamorphism occurred at ca. 0.5-07 GPa and 330-370 °C (Fig. 9). These P-T estimates are in good agreement with those obtained by Di Vincenzo et al. (2016), thus providing a consistent picture of the tectono-metamorphic overprint of Hercynian Corsica at the footwall of the ADF. The restricted Wm composition imposes a cooling exhumation path, similarly to what reconstructed for the ETSZ (Maggi et al., 2012). Similar along-strike peak P conditions are reconstructed at the footwall of the ADF, where progressive burial and exhumation cooling can be proposed for the Hercynian basement of western Corsica (Fig. 9).

Considering an average rock density of 2700 kg/km, the peak P-T conditions recovered from the continental basement of Corsica conform to a paleo-geothermal gradient of ca. 11°C/km, typical of the low geotherm in active and fossil convergent plate margins (Penniston-Dorland et al., 2015; Agard et al., 2018). When the P-T estimates are compared with those available from literature, it is evident that the Corsica basement was equilibrated at shallower depths according to a warmer geothermal gradient with respect to the Mesozoic cover rocks (Di Rosa, 2019) and the metamorphic units of the Tenda Massif (Molli et al., 2006; Maggi et al., 2012; Rossetti et al., 2015), but recorded a similar cooling exhumation trajectory at lower pressures (Fig. 11)

The low-T deformation environments reconstructed through thermodynamic modelling are in line with the microtextural evidence of the studied samples, which documents, regardless of the strain intensity and fabric type (either D_1 or D_2), brittle deformation in feldspar as opposed to ductile flow and fine-grained dynamic recrystallisation in quartz (Fig. 6 and Supplementary Material#1), and white mica crenulation. Dynamic recrystallization in quartz was dominantly assisted by bulging grain boundary (BLG) and subgrain rotation (SGR) recrystallization in the highest strain domains (sample CO36 and CO42), compatible with environmental temperatures at the transition between the BLG and SGR zones, at about 400 ±30 °C (Stipp et al., 2002). Taken together, these microtextural constraints attests that ductile processes were not activated in Fsp and deformation temperatures were well below 400-450 °C (e.g., O'Hara, 1990; Passchier & Trow, 2010).

At such low-T conditions, structurally controlled fluid flow and fluid-mediated deformation promoted metamorphic recrystallization and rheological weakening of the Corsica basement

during the low-grade Alpine tectono-metamorphic evolution. Significantly, brittle precursor localized the ductile shearing in the basement units, as documented by the field and microtextural evidence of extensive fracturing and veining associated with development of the Alpine tectono-metamorphic fabric (Fig. 3h, 5f-h; .6a, c, e, f), providing further evidence of ductile strain localization initially controlled by brittle behavior of granitoid rocks (Mancktelow and Pennacchioni 2005; Fusseis and Handy, 2008; Sarkar et al., 2020). In particular, formation of Ph-rich bands of deformation and mylonites (Fig. 6) documents that fracturing of feldspar followed by fluid-assisted breakdown to white mica was the dominant process leading to reaction softening and shear strain localization in the Corsica basement (e.g., Wintsch et al., 1995; Gueydan et al., 2003; Holyoke and Tullis, 2006; O'Hara, 2007).

A relatively high water/rock ratio during progress of the D_1-D_2 tectono-metamorphic evolution can be deduced by a general hydration of the granitoid basement rocks, with the diffuse blastesis of Ph-Amp-Ep associations. Further evidence of fluid-rock interaction is provided by the occurrence of secondary Ca-rich mineral assemblages (Adr-rich garnet, epidote, Ca-amphibole, ilvaite and late carbonates), which indicate intensive alteration of the early magmatic assemblages (Cpx - Mag) in the basement rocks by the chemically reactive infiltrating fluids and variable redox conditions (e.g., Barton & Berger, 1984; Delgado Martín & Soleri Gil, 2010).

Similarly to other studies dealing with formation of microstructures during mylonitization of granitoid precursors, the fluid-rock interactions, reaction weakening and partitioning of deformation are recognized key elements for strain softening and localization during shear zone nucleation and development (e.g., Janecke and Evans, 1988; O'Hara, 1990, 2007; Wintsch et al., 2005, 2007; Johnson et al., 2008; Goncalves, 2012; Maggi et al., 2014; McAlleer e al., 2017; Papeschi & Musumeci, 2019).

8.2 Age of crustal shortening

Based on the P-T estimates and microtextural evidence, deformation in the investigated samples developed under temperature conditions insufficient to alter by volume diffusion the Ar isotope record of white mica. In fact, several field-based studies have documented that Wm can preserve crystallization ages up to at least ~500 °C (e.g. Di Vincenzo et al. 2004; Augier et al. 2005; Villa et al. 2014). Given that the strongly peraluminous character of the investigated rock samples does not represent a primary feature of the igneous protoliths (Di Vincenzo et al., 2016), the ^{40}Ar-

^{39}Ar ages from Wm record the time of (re)-crystallization during fluid-assisted deformation. Both samples CO24 (Transect-1) and CO42 (Transect-3) are characterized by deformation features representative of the D_1 fabric, by Wm with phengitic compositions and by the lack of muscovitic Wm relicts. Even excluding ages older than ~44 Ma in sample CO24 and ~47 Ma in sample CO42, our results extend back the development of Alpine syn-deformational phengitic white mica and consequently crustal shortening of western Corsica to the early Lutetian (at ca. 48 Ma). Sample CO36 from transect-2, is dominated by the D2 progressive shear deformation and mainly yielded Priabonian ages. This sample is however characterized by the occurrence of two Wm generations, a dominant phengitic Wm2 aligned along the main D2 foliation and rare muscovitic relics representing syn-burial remnants. A possible explanation for this apparent inconsistency is that either (1) data record a Priabonian burial or, more likely, (2) muscovitic relics were coincidentally not sampled during data collection. Following hypothesis (2), ^{40}Ar-^{39}Ar data constrain the development of the D_2 deformation to the Priabonian (ca. 33-38 Ma) and the last increments of syn-D_2 shearing to not earlier than the Priabonian-Rupelian transition.

Ages older than the Bartonian, have been previously reported for phengitic Wm of the Tenda Massif and the Schistes Lustrés Unit (Monte Pinatelle area) by Brunet et al. (2000). More recently, Maggi et al. (2012) reported two Ypresian nominal ages from two poorly-defined U-Pb isochrons using synkinematic rutile fractions and acmite, phengite and oxide-sulfide coating derived from blueschist-facies top-to-the-W phyllonitic shear bands within the East Tenda Shear Zone (Maggi et al., 2012; Fig. 1). Maggi et al. (2012) assigned the excess of scatter in the data arrays to secondary disturbance. On the other hand, the deformation ages recovered in this study only partially overlap with the U-Pb zircon and Lu–Hf garnet and lawsonite ages as derived from eclogites of the Schistes Lustrés, which provided Prabonian-Rupelian ages (ca. 34-37 Ma; Martin et al., 2011; Vitale Brovarone and Herwartz, 2013).

8.3 Tectonic reconstruction

Our petrotectonic reconstruction frames convergent deformation in the Western Corsica basement during the Eocene-Oligocene. We provide evidence that pure shear dominated deformation of the Corsica basement predated simple shear strain localization. During early-middle Eocene times (ca. 50 to 40 Ma), the Hercynian continental crust was first homogenously shortened during development of a steeply dipping high strain deformation zone in response to a

609 roughly E-W directed maximum compression direction (D_1). Top-to-the-W ductile shearing (D_2)
610 occurred later, with the last shear increments during the early Oligocene at ca. 32-33 Ma,
611 synchronous with activation of the syn-blueschist, top-to-the-W reverse shearing along the ETSZ
612 (Rossetti et al., 2015). Therefore, the coupling between the different tectonic units of the Alpine
613 orogen in Corsica occurred nearly synchronously during the late Eocene-early Oligocene (34-32
614 Ma) and in a restricted P-T interval (ca. 0.5-07 GPa and 300-400°C; Fig. 11), when the deepest and
615 cooler units of the Shistes Lustrés were exhumed at shallower crustal conditions, overthrusted and
616 tectonically assembled along the ETSZ onto the W Corsica basement. At this stage, the Alpine
617 shortening was accommodated through non-coaxial shearing and W-directed thrusting along the
618 entire Alpine orogenic system of Corsica, propagating westward across the basement complex.
619 The final tectonic coupling caused formation of a late Eocene-early Oligocene, W-verging nappe
620 stack, characterized by an inverted sequence of metamorphic units (from top to bottom:
621 blueschist- to eclogite-facies Schistes Lustrés, blueschist-facies Tenda Massif, and greenschist-to-
622 blueschist-facies Western Corsica basement) bounded by major, crustal-scale top-to-the-W shear
623 zones, equilibrated under low-grade HP greenschist (W Corsica) to blueschist facies (ETSZ)
624 metamorphic conditions, respectively. The composite Alpine ductile D_1/D_2 fabric in the Corsica
625 basement is truncated by brittle thrusts, related to the later thick-skinned thrusting involving the
626 basement and cover units during continuous shortening (Bezert and Caby, 1988; Rossi et al., 1994;
627 Di Rosa et al., 2020a; Frassi et al, 2022; this study). Transition from orogenic construction to post-
628 orogenic extensional thinning in Corsica occurred during the late Oligocene-early Miocene, as
629 documented by the extensional reactivation of the ETSZ (Rossetti et al., 2015).
630 When integrated at regional scale, the P-T-t-deformation history as reconstructed from the
631 metamorphic units of the Alpine orogen in Corsica has significant implications as to the timing of
632 the subduction zone metamorphism and the tectonic/geodynamic evolution along the Mesozoic-
633 Cenozoic active margin developed during convergence of the African and European plates (see
634 also Vitale Brovarone and Herwatz, 2013). Paleotectonic reconstructions frame the Alpine
635 orogeny in Corsica either as the southward prosecution of the Western Alps governed by
636 southeast-dipping ("Alpine") subduction (e.g., Doglioni et al., 1998; Molli & Malavieille, 2010;
637 Handy et al., 2010; Carminati et al., 2012; Marroni et al., 2017) or as the retroward tectonic
638 accretion above the backstop of the accretionary wedge produced by the north-dipping
639 ("Apennine-Maghrebian") subduction (Principi and Treves, 1984; Jolivet al., 1998; Jolivet &
640 Faccenna, 2000; Faccenna et al., 2001; 2004; Rossetti et al., 2004; Lacombe & Jolivet, 2005; Vitale

Brovarone & Hervatz, 2013; van Hinsbergen et al., 2014; Bestani et al., 2016; Jolivet et al., 2021). The first scenario involves a subduction flip during the Cenozoic, with the early structured Alpine belt passively overthrusted onto the growing Apennine-Maghrebian orogenic wedge, whereas the second scenario considers a continuous northward subduction in Cenozoic times. In both configurations, the Oligocene-Miocene geodynamics is controlled by the Maghrebian-Apennine slab roll-back and crustal thinning in the back-arc domain.

Eocene-Oligocene orogenic metamorphism in the Corsica basement (from ca. 50 to 32 Ma) broadly overlaps (i) with the age of the orogenic metamorphism affecting both the oceanic- and continental-derived units in the hinterland of the Maghrebian-Apennine accretionary wedge, as documented in Calabria (ca. 50-35 Ma; Schenk, 1980; Rossetti et al., 2001a; 2004; Heymes et al., 2010), in the Alboran Domain of the Betic-Rif belt (ca. 50-40 Ma; Augier et al., 2005; Li and Massonne, 2018; Marrone et al., 2021a, b; Bessiere et al., 2022), and the Eastern Kabylia region (ca. 32-21 Ma; Bruguier et al., 2017); and (ii) with the oldest calcalkaline magmatism in Provence, Sardinia, and Alboran Domain, showing Bartonian-Rupelian ages (ca. 40–32 Ma; Lustrino et al., 2009; 2017) (Fig. 1). The Apennine-Maghrebian subduction was thus active since at least Eocene times, a time span compatible with efficient subduction slab retreat and the Oligocene-Miocene back-arc opening of the Liguro–Provençal, Alboran, and Tyrrhenian basins (e.g., Doglioni et al., 1997; Faccenna et al., 2001; Jolivet & Faccenna, 200; Gattacecca et al., 2007; Lacombe & Jolivet, 2005; Malinverno & Ryan, 1986; Seranne et al., 1999; Rosebaum et al., 2002; Royden, 1993).

We confirm earlier studies (Maggi et al., 2012) providing evidence that the early-middle Eocene (ca. 50-40 Ma) orogenic metamorphism in the Corsica basement predated of ca. 10-15 Ma the late Eocene subduction zone metamorphism in the oceanic-derived units of the Schistes Lustrés (ca. 37-34 Ma; Martin et al., 2012; Vitale Brovarone and Herwatz, 2013). The latter was instead nearly synchronous with the timing of blueschist metamorphism recorded in the Liguride ophiolites (late Eocene-early Oligocene (ca. 35-28 Ma; Ar-Ar phengite dating in Rossetti et al., 2001a, b) but younger than the Oligocene-early Miocene orogenic metamorphism recorded in the Adria-derived continental units (ca. 30-20 Ma; Ar-Ar phengite dating in Brunet et al., 2000; Rossetti et al., 2004) exposed in the hinterland of the Apennine chain. Moreover, when the Corsica basement was involved in the Alpine orogeny, the Europe-derived continental units where accreted to the Adria plate, as documented in the Calabrian–Peloritan belt of the southern Apennines (Fig.1; Schenk, 1980; Dietrich, 1988; Rossetti et al., 2001; Vignaroli et al., 2008; 2012; Heymes et al., 2010). Finally, similarly to the Corsica case, the transition from orogenic accretion

673 to crustal thinning in the Calabrian–Peloritan belt is late Oligocene-early Miocene (Platt and
674 Compagnoni, 1990; Thomson, 1994; Rossetti et al., 2004; Heymes et al., 2010).
675 Since the orogenic structuration of the Europe-derived basement (foreland of the Alpine
676 orogen) of Corsica pre-dated the subduction zone metamorphism of the oceanic-derived domain
677 (hinterland), the south-dipping "Alpine" subduction setting is not a feasible solution to frame the
678 Alpine orogenic construction in Corsica (see also Vitale Brovarone and Herwatz, 2013). The
679 Cenozoic Apennine-Maghrebian subduction system formed along the convergent margin that
680 accommodated the subduction of the Ligurian branch of the Tethyan realm below the European
681 plate therefore appears as the more appropriate setting. The orogenic structure of Corsica is
682 therefore interpreted as produced in the retrowedge of the E-verging Apennine orogenic wedge,
683 as produced by the retroward-directed accretion against the backstop of the European plate. In
684 this scenario, the transition from pure-shear to simple-shear dominated style of deformation in
685 the Corsica basement - as determined in this paper - is interpreted as the response of continuous
686 shortening in the backstop region of the orogenic wedge, where the upper-plate material is first
687 shortened at depth (buttressing effect), progressively exhumed in the wedge axial zone, and then
688 accreted against the rigid backstop (Fig. 12). The Mesozoic cover rocks were detached from their
689 basement during progress of the Alpine shortening and metamorphosed at depth, similarly to
690 what has been reconstructed for the Oman obduction margin (e.g., Agard et al., 2010). Likewise,
691 the continent-derived units of the Tenda Massif, forming the basal thrust of the obducted Schistes
692 Lustrés Complex (Molli et al., 2006; Rossetti et al., 2015), were part of a crustal sliver separated
693 from the western Corsica basement, confirming previous paleotectonic reconstructions proposing
694 that the Alpine convergent margin overprinted a stretched continental margin (Vitale Brovarone
695 et al. 2013).
696
697 **8.4 Questioning Hercynian Corsica**
698 The traditional subdivision of the island into "Alpine" and "Hercynian" Corsica implies (by
699 definition) the absence of Alpine-age deformation in its western part. These terms and the
700 underlying assumption have largely dominated geological thinking and are ingrained in the
701 literature despite early notice of the existence of significant Alpine deformation within the
702 Hercynian granitoids (e.g. Deprat, 1905). In recent years, a mounting body of structural and
703 radiometric evidence has shown that the Hercynian basement complex of central Corsica and its
704 late Paleozoic cover suffered significant Alpine-age ductile shear (Malasoma et al., 2006, 2019;

Malasoma and Marroni, 2007; Garfagnoli et al., 2009; Di Vincenzo et al., 2016; Di Rosa et al., 2017, 2019; 2020b; Frassi et al., 2022; this study). Notably, the entire Hercynian basement of Corsica was affected by the thermal (tectono-metamorphic) effects of Alpine-age shortening and/or burial underneath the sediments of the foreland basin (Fig. 1c). Coherent thermochronometric datasets point to the former existence of a widespread tectono-sedimentary cover (up to 7-8 km thick) now lost to erosion (Cavazza et al., 2001; Zarki-Jakni et al., 2004; Fellin et al., 2006; Danisik et al., 2007). The structural, radiometric, and thermochronologic evidence outlined above show that the whole of Corsica was directly affected by the Alpine orogeny. We thus propose the abandonment of the traditional terms “Alpine” and “Hercynian Corsica” as they are altogether incorrect and misleading.

9. Conclusions

The P-T-t-deformation history of the Corsica basement presented in this paper indicates that Alpine orogenic construction spans from early/middle Eocene to early Oligocene times (ca. 50 to ca. 32 Ma). Crustal shortening in the continental basement predated of ca. 15-10 Ma the subduction zone metamorphism in the oceanic derived Schistes Lustrés Complex. These new structural and temporal constraints frame the Alpine orogeny in Corsica within the Cenozoic Apennine-Maghrebian subduction system, in the retroside of the Apennine orogenic wedge.

Acknowledgements

Sara Marrone participated to the field work. We wish to thank Moritz Schmelz for help in thin section preparation.

Appendix - A: Analytical protocols and methods

Electron Microprobe Analyses (EMPA)

Mineral phases were analyzed with a Cameca SX100 electron microprobe at the Faculty of Chemistry, Universität Stuttgart. Operating conditions were 15 kV and 10-15 nA, counting times of 20 s both for peak and background, spot sizes of 1-5 µm. Compositions were determined relative to synthetic oxides, and minerals, used also for routine calibration and instrument stability monitoring. Repeated analyses of the standards resulted in one-sigma (1σ) standard deviations close to the ones calculated from counting statistics. For the major minerals, calculated 1σ (%) precisions are (i) better

than 1.5 % for Si; (ii) better than 2% for Al; (iii) 1 to 5% for Ca, Mg, Fe, Mn, Ti, Na and K, applying the above-mentioned conditions. The chemical formulas of white mica (Wm) were calculated on the basis of 11 oxygens and Σ (Si, Al, Ti, Cr, Mn, Mg, Fe) = 6.02 cations, assuming Fe^{3+}= [9.96-2*(Si+Ti)-(Al+Cr)-2*(Ca+Ba)-(Na+K)], and a stoichiometric fixed trioctahedral substitution (X_{Tri} = 0.02). The molar fractions of paragonite (X_{Pg} = atomic [Na/(Na+K+Ca+Ba)]), pyrophyllite (X_{Prl} = [1-(Na+K+Ca+Ba)]), muscovite (XMs = $Al^{[IV]}$- {X_{Pg}+X_{Prl}+(X_{Tri}/2)+Ti+[(Ca+Ba)/(Na+K+Ca+Ba)]}) and celadonite (XCel = 1-{X_{Ms}+X_{Pg}+X_{Prl}+(X_{Tri}/2)+Ti+[(Ca+Ba)/(Na+K+Ca+Ba)]}) were then calculated. The chemical formulas of chlorite (Chl) were calculated based on 10 cations (Σ [Si, Al, Ti, Cr, Mn, Mg, Fe]) assuming Fe^{3+}(apfu) = [8 – 2*(Si+Ti)-Al^{Tot}]. The chemical formulas of stilpnomelane (Stp) were calculated on the basis of 120 cations (Σ [Si, Al, Ti, Mn, Mg, Fe]), assuming (Si+$Al^{[IV]}$)=72 apfu, Fe^{3+}={[Al^{Tot}+2*Fe^{Tot}+2*(Mg+Mn)+2*(Si+Ti)+2*(Ba+Ca)+K+Na]/3}-64 and OH = (Fe^{2+}+Mg+Mn). The chemical formulas of feldspar (Fsp) were calculated based on 8 oxygens assuming Fe^{3+}=Fe^{Tot}. The chemical formulas of titanite (Ttn) were calculated based on 5 oxygens, assuming Si= 1 apfu and Fe^{3+}=Fe^{Tot}. The chemical formuls of epidote (Ep) were calculated based on 12.5 oxygens and assuming Fe^{3+}=Fe^{Tot}. The pistacite component (X_{Ps} = atomic [Fe^{3+}/(Al+Fe_{3+})]) was then calculated. The chemical formulas of biotite (Bt) were calculated based on 11 oxygens assuming Fe^{2+}=Fe^{Tot}. The chemical formulas of ilvaite (Ilv) were calculated based on 8.5 oxygens and assuming (Al+Fe^{3+}) = 1 apfu. The chemical formulas of ilmenite (Ilm) were calculated based on 2 cations (Σ [Al, Ti, Mn, Mg, Fe]) assuming Fe^{3+}(apfu) = [2 – (2* Ti)-Al]. The chemical formulas of garnet (Grt) were calculated based on 8 cations with H_2O wt% determined through the deficiency of Si in the tetrahedral site [Si^{4+} + (H^+/4)] = 3 apfu. Feldspar, biotite, titanite, ilmenite and magnetite structural formulae were calculated using existing routines in Calcmin_32 software (Brandelink, 2009). White mica, chlorite, stilpnomelane, epidote, garnet and ilvaite structural formulae were calculated through opportune routines compiled during this work and then implemented in the Calcmin_32 software (Brandelik, 2009). The chemical formulae of amphibole were calculated through the ACES2013 Excel spreadsheet (Locock, 2014), using the 13-CNK normalization scheme and with Fe^{3+} estimation following the electroneutrality criterion (Hawthorne et al., 2012). Amphibole classification is after Wintsch et al., (1999) and Hawthorne et al. (2012).

Whole-rock geochemistry

Whole-rock major element analyses were performed at the Activation Laboratories (Ontario, Canada), by means of ICP emission following the 4Lithores analytical protocol (lithium

metaborate/tetraborate fusion ICP whole rock) For major elements the precision is estimated better than 2% for values higher than 5 wt %, and better than 5% in the range 0.1-5 wt %. Further details can be found at https://actlabs.com/geochemistry/lithogeochemistry-and-whole-rock-analysis/lithogeochemistry/#d2c5f444686baec86.

^{40}Ar–^{39}Ar geochronology

^{40}Ar–^{39}Ar in-situ analyses were completed at IGG-CNR (Pisa, Italy). Following back-scattered electron (BSE) imaging, rock chips ~9 mm in diameter was drilled from polished thick (~0.4 mm thick) sections using a diamond core drill. Samples, after cleaning by alternating deionized water and methanol, were wrapped in aluminum foil and irradiated for 60 hours in the TRIGA reactor at the University of Pavia (Italy), along with the monitor Fish Canjon Tuff sanidine (FCs). In-situ ^{40}Ar-^{39}Ar analyses were completed through an ultraviolet laser beam, produced by a pulsed Nd:YAG laser (frequency quadrupled and Q-switched). The ultraviolet laser, operating at 20 Hz and 0.5–1 mJ per pulse, was focused to ~10 μm and repeatedly rastered, by a computer-controlled x–y stage, over areas of ~0.010-0.015 mm^2 (typical 100x100 μm^2) and a few ten micrometres deep. Argon isotope compositions were determined simultaneously through a multi-collector noble gas mass spectrometer ARGUS VI (Thermo Fisher Scientific). Ar isotopes from 40 to 37 were acquired using Faraday detectors, equipped with 10^{12} Ω resistors for ^{40}Ar and ^{38}Ar and 10^{13} Ω resistors for ^{39}Ar and ^{37}Ar. Faraday detectors were cross calibrated for the slight offset using air shots. ^{36}Ar was measured using a Compact Discrete Dynode (CDD) detector. The CDD was calibrated daily for its yield by measuring four to six air pipettes prior to the first analysis. Blanks were monitored every one to two runs and were subtracted from succeeding sample results. Data corrected for post-irradiation decay, mass discrimination effects, isotope derived from interfering neutron reactions and blank are listed in Supplementary Material#3. Uncertainties on single runs are 2σ analytical uncertainties, including in-run statistics and uncertainties in the discrimination factor, interference corrections and procedural blanks. Uncertainties on weighted means also include the uncertainty on the fluence monitor (2σ internal errors). Ages were calculated using an age of 28.201 Ma for the FCs (Kuiper et al., 2008), using decay constants of Min et al. (2000) and an atmospheric ^{40}Ar/^{36}Ar ratio of 298.56 ± 0.31 (Lee et al., 2006). More details about mass spectrometer calibration and analysis can be found in Di Vincenzo et al. (2021).

Figure Captions

Figure 1 – (a) The Western Mediterranean region with the main Alpine orogenic belts (red lines indicating the orogenic fronts) and distribution of the exhumed orogenic roots (purple areas). The study area is indicated by a yellow rectangle. (b) Geological sketch map of the Corsica Island (modified after Cavazza et al., 2018); (c) Maximum temperatures experienced by the Corsica rocks during the Alpine tectonics as derived from low-T thermochronology and Raman spectroscopy of carbonaceous materials. The areal distribution of maximum temperatures indicates that virtually all the island was covered either by the Alpine orogenic wedge or by foreland deposits. Source of data: Cavazza et al. (2001), Zarki-Jhaki et al. (2004), Fellin et al. (2006), Danisik et al. (2007) Viatle Brovarone et al. (2013), Jourdan et al. (2018).

Figure 2 – Geological map of the study area at the junction between Alpine and Hercynian Corsica (modified and re-adapted after (Vitale Brovarone et al., 2013), with indicated the three geological transects and representative samples described in this study. The metamorphic lineations and associated sense of shear are after Jolivet et al. (1990), Molli et al. (2006), Maggi et al. (2014) Rossetti et al. (2015); Beaudoin et al. (2020), this study.

Figure 3 – (a) Geological map of the Ponte Castirla area (modified and readapted after Rossi et al., 1994) showing distribution of the main ductile and brittle structural fabrics along Transect-1. West-verging, ductile-to-brittle thrust contacts are mapped out and a tectonic doubling of the basement stratigraphy is evident. The unconformable Eocene sediments are also involved in thrusting. The geological cross section illustrates the structural architecture of the Corsica basement across Transect-1. Location of the studied samples are also shown. Moving westward, transition from S_1-L_1 plano-linear fabric to D_2 mylonites (S_2 foliation) is observed in the basement units. (b) Equal-area (lower-hemisphere projection) stereoplots showing the ductile (D_1, D_2) and brittle fabrics reconstructed along Transect -1. (c) Subvertical principal S_1 foliation and incipient E-dipping S2 foliation in the Permian volcaniclastics (sample CO24). (d) D_2 S-C tectonites developed in Permian volcaniclastics (sample CO25). Sense of shear is top-to-the-W. The inset shows D_2 crenulation folding in shear lithons. (e) Protomylonite fabric in Hercynian granitoids (sample Co-38).

Figure 4 – (a) Geological cross section illustrative of the structural architecture across Transect-2 and sample location. (b) Characters of the D_2 deformation in the Hercynian granitoids. Transition

from D_2 crenulation (lower portion) to ductile shearing (upper portion) is evident. (c) Sigma-type feldspar porphyroclasts indicating top-to-the-W shearing. (d) Equal-area (lower-hemisphere projection) stereoplot of the D_2 plano-linear fabric.

Figure 5 - (a) Geological cross section illustrative of the structural architecture across Transect-3 and sample location. (b) Equal-area (lower-hemisphere projection) stereoplot of the D_1 (left) and D_2 (right) structures. (c) Gneissic texture (S-L tectonites) in the Hercynian granitoids (exposure paralle to L_1 and normal to S_1. Porphyroclastic feldspar (Fsp) – quartz (Qz) systems define the main S_1 foliation. Kinematic criteria are not univocal, indicating overall pure-shear (coaxial) deformation. (d) L_1 stretching lineations in granitoids made of Qz- Wm aggregates trending at high angle (pitch 104°) to the S_1 strike. (e) Subvertical S_1 foliation in the Permian volcaniclastics. Note the sub-horizontal Qz veins and intrafoliar F_1 folds. (f) Detail showing isoclinal F_1 folds in the Permian volcaniclastics. Note the deformed, early segregated quartz veins. (g) D_1 boundinage and stretching in Permian volcaniclastics. (h) S_2 foliation, axial planar to W-verging folds, overprinting a continuous S_1 foliation and early segregated quartz veins in the Permian volcaniclastics.

Figure 6 - Sample Microtextures. (a) Thin section scan of sample CO24, showing the S_1 foliation as defined by aligned white mica embedding quartz and fractured fedspar porphyroclasts. Kinematic criteria as provided by sigma-type clasts are not univocal, indicating overall pure shear (coaxial) deformation. (b) The sample CO24 at microscale (crossed polars). The S_1 foliation is defined by aligned white mica layers and finely-recrystallised quartz enveloping fractured feldspar grains. Post-tectonic calcite (Cc) growth is observed. (c) Oblique foliation and S-C fabric defined by aligned white mica folia and recrystallized quartz in sample CO25 (crossed polars). Note syn-tectonic stilpnomelane growth along the C surfaces. (d) Microtexture of sample CO38 (crossed polars), showing fractured feldspar grains with recrystallized quartz veins. Domains of shear strain localization formed by fine-grained recrystallized quartz and white mica enveloped the large feldspar porphyroclasts. In the high strain domains, quartz shows evidence of undulose extinction, deformation bands and evidence of dynamic recrystallisation, dominantly assisted by grain boundary bulging (BLG). (e) Microtexture of sample CO36 (crossed polars), showing feldspar porphyroclasts with recrystallized quartz veins. Relict igneous quartz show evidence of subgrain formation (SG) and evidence of dynamic recrystallisation dominantly assisted by subgrain rotation. The shear bands are defined by fine-grained recrystallized quartz and white mica. The sense of

shear, as defined by S-C structures, oblique foliation, and sigma-type porphyroclasts, is top-to-the-W. (f) Thin section scan of sample CO42, showing the S_1 foliation as defined by white mica folia and quartz ribbons enveloping porphyroclastic feldspar grains. Stilpnomelane is aligned along the S1. (g) Microtexture of sample CO42 (crossed polars) showing fractured igneous quartz and feldspar grains, embedded in a matrix made of white mica and finely recrystallized quartz that define the S_1 foliation. The relict quartz show evidence of undulose extinction, subgrain formation and dynamic recrystallisation. The white mica is crenulated.

Figure 7 - Sample microtextures. (a) Back-scattered electron (BSE) image of sample CO24, showing elongated quartz and fractured (igneous) feldspar. White mica defines the main S1 foliation and together with quartz fill the cracks in feldspar. (b) BSE image of sample CO25, showing a pseudomorphic replacement made of white mica, chlorite, titanite, apatite along the main S1 foliation. (c) BSE image of sample CO55 showing a quartz-white mica- stilpnomelane veins cutting across a K-feldspar grain. (d) Coronitic overgrowth of the assemblage made of stilpnomelane-amphibole (winchite)-epidote-titanite after igneous magnetite in sample CO38 (natural light). (e) BSE image showing chemical zoning of white mica and epidote in sample CO35. (f) The assemblage epidote-garnet-amphibole (riebekite) overgrowing igneous allanite and magnetite in sample CO35 (natural light). (g) BSE image showing two generations of white mica in sample CO36. (h) BSE image showing two generation of epidote in sample CO36. (i) Decussate texture defined by amphibole (riebekite) and stilpnomelane in sample CO42 (natural light).

Figure 8 – White mica texture and composition in dated samples. (a) sample CO24. (b) Sample CO36. (c) Sample CO42. (d) Right: Si vs. Al + Fe^{3+} diagram for the analyzed Wm; Left: Celadonite – Pyrophyllite – Muscovite diagram showing the composition of the analyzed Wm.

Figure 9 – NCKFMASHTO P–T pseudosections calculated for the dated samples (bulk rock composition shown in Table 2). The fields are contoured with isopleths of phengite (Si apfu) compositions. Occurrence of stilpnomelane and absence of pumpellyite at low-T and biotite at high-T, respectively, constrain the overall thermobaric evolution. Mineral abbreviations are after Whitney and Evans (2010).

Figure 10 - Summary of in-situ ^{40}Ar-^{39}Ar data on rock chips of samples CO24, CO36 and CO42: cumulative probability distribution and ranked distribution. Uncertainties are 2σ. Ages refer to the youngest peak for each sample. Data are compared with the cumulative probability distribution of samples previously investigated by Di Vincenzo et al. (2016).

Figure 11 – Alpine P-T-t paths of the Corsica basement units as available from the literature compared with the P-T-t data as reconstructed in this study. The tectonic coupling of the different tectonic slices is constrained at ca. 0.4 GPa and T lower that 300°C during continuous cooling and W-directed ductile-to-brittle shearing (thrusting).

Figure 12. Schematic tectonic reconstruction of the Alpine orogeny in Corsica framed within the retrowedge of the Apennine orogenic wedge (doubly verging orogen). (a) Shortening of the continental margin as induced by buttressing against the rigid backstop of the European plate (upper-plate). In this stage (D_1 deformation, at ca. 50-40 Ma) the basement units were homogenously horizontally shortened and vertically stretched (yellow strain ellipse). (b) Continuous shortening resulted in the progressive exhumation of the early underplated HP oceanic units (Schistes Lustrés) that were progressively overthrusted and assembled against the basement units along the ETSZ. This stage corresponds to the the top-to-the-W simple-shear stage (D_2 deformation, at ca. 33-32 Ma) in the early deformed basement units (Not scale; location of structures is only indicative).

Supplementary Material#1: Fsp and Qz microfabrics in the studied samples.

Supplementary Material#2: EMPA and representative chemical formulas of syn-metamorphic mineral phases

Supplementary Material#3: T- Fe2O3 pseudosections for samples CO36 and CO42 (calculated at 0.6 GPa)

Supplementary Material#4: Ar-Ar in-situ-data

927 ## References

928 Agard, P., Searle, M.P., Alsop, I., & Dubacq, B. (2010). Crustal stacking and expulsion tectonics during
929 continental subduction: P-T deformation constraints from Oman. Tectonics, 29 TC5018 1-19,
930 doi:10.1029/2010TC002669.
931 Agard, P., Plunder, A., Angiboust, S., Bonnet, G., & Ruh, J. (2018). The subduction plate interface:
932 rock record and mechanical coupling (from long to short timescales). Lithos, 320–321, 537–566.
933 https://doi.org/10.1016/j.lithos.2018.09.029
934 Allmendinger, R.W., & Gubbels, T. (1996). Pure and simple shear plateau uplift, Altiplano-Puna,
935 Argentina and Bolivia. *Tectonophyscs, 259*, 1-13.
936 Augier, R., Agard, P., Monié, P., Jolivet, L., Robin, C. & Booth-Rea, G. (2005). Exhumation, doming
937 and slab retreat in the Betic Cordillera (SE Spain): in situ 40Ar/39Ar ages and P–T–d–t paths for
938 the Nevado-Filabride complex. Journal of Metamorphic Geology, 23, 357–381, doi:
939 10.1111/j.1525-1314. 2005.00581.x
940 Austrheim, H. (1987). Eclogitization of lower crustal granulites by fluid migration through shear
941 zones. *Earth and Planetary Science Letters, 81*(2-3), 221-232.
942 Babeyko, A. Y. & Sobolev, S. V. (2005). Quantifying different modes of the late Cenozoic shortening
943 in the central Andes. *Geology*, 33, 621-624.
944 Barton, M. & Bergen, M.J. (1984). Secondary ilvaite in a dolerite dyke from Rogaland, SW Norway.
945 *Mineralogical Magazine*, *48*, 449–456.
946 Beaudoin, A., Scaillet, S., Mora, N., Jolivet, L., & Augier, R. (2020). In situ and step-heating $^{40}Ar/^{39}Ar$
947 dating of white mica in low-temperature shear zones (Tenda massif, Alpine Corsica, France).
948 Tectonics, 39, e2020TC006246. https://doi.org/10.1029/2020TC006246
949 Bestani, L., Espurt, N., Lamarche, J., Bellier, O., & Hollender, F., (2016). Reconstruction of the
950 Provence Chain evolution, southeastern France, Tectonics, 35, 1506–1525,
951 doi:10.1002/2016TC004115
952 Bezert, P., & Caby, R. (1988). Sur l'âge post-Bartonien des événements tectonometamorphiques
953 alpins en bordure orientale de la Corse cristalline (Nord de Corte). *Bulletin de la Société*
954 *Geologique de France*, 8, 965–971.
955 Brandelik, A. (2009). CALCMIN–an EXCEL™ Visual Basic application for calculating mineral structural
956 formulae from electron microprobe analyses. *Computer and Geosciences, 35*, 1540-1551.
957 Bruguier, O., Bosch, D., Caby, R., Vitale-Brovarone, A., Fernandez, L., Hammor, D., et al. (2017). Age
958 of UHP metamorphism in the Western Mediterranean: Insight from rutile and minute zircon
959 inclusions in a diamond-bearing garnet megacryst (Edough Massif, NE Algeria). Earth and
960 Planetary Science Letters, 474, 215–225. https://doi.org/10.1016/j.epsl.2017.06.043
961 Brunet, C., Monié, P., Jolivet, L., Cadet, J.P. (2000). Migration of compression and extension in the
962 Tyrrhenian Sea, insights from $^{40}Ar/^{39}Ar$ ages on micas along a transect from Corsica to Tuscany.
963 *Tectonophysics, 321*, 127–155, doi:10.1016/S0040-1951(00)00067-6
964 Carminati, E., Lustrino M., & Doglioni, C. (2012). Geodynamic evolution of the central and eastern
965 Mediterranean: Tectonics vs. igneous petrology constraints. *Tectonophysics, 579*, 173–192.
966 Cavazza, W., Zattin, M., Ventura, B., Zuffa, G.G., 2001. Apatite fission-track analysis of Neogene
967 exhumation in northern Corsica (France). Terra Nova 13, 51–57.
968 Cavazza W., Gandolfi G., & Paganelli L. (2018). Reconstructing the Alpine orogenic wedge and its
969 foreland basin: The petrologic transition from Cretaceous passive-margin to Eocene foreland
970 sedimentation in northern Corsica (France). In: R.V. Ingersoll, T.F. Lawton and S.A. Graham (Eds.),
971 Tectonics, sedimentary basins, and provenance: A celebration of the career of William R.
972 Dickinson. Geol. Soc. Am. Spec. Pap., 540. https://doi.org/10.1130/2018.2540(31)

973 Connolly, J.A.D., 2005. Computation of phase equilibria by linear programming: A tool for
974 geodynamic modeling and its application to subduction zone decarbonation. Earth Planetary
975 Science Letters 236, 524–541
976 Delgado Martín, J., & Soleri Gil, A. (2010). Ilvaite stability in skarns from the northern contact of the
977 Maladeta batholith, Central Pyrenees (Spain). *European Journal of Mineralogy, 22* (3), 363-380,
978 doi: 10.1127/0935-1221/2010/0022-2021
979 Danisik, M., Kuhlemann, J., Dunk, I., Szekely, B., & Frisch, W. (2007). Burial and exhumation of
980 Corsica (France) in the light of fission track data. *Tectonics, 26*, TC1001.
981 http://dx.doi.org/10.1029/2005TC001938.
982 Deprat, M. (1905). L'origine de la protogine de Corse. Comptes Rendue Ac. Sc., 141 (2), 151-153.
983 Dietrich, D. (1988). Sense of overthrust shear in the Alpine nappes of Calabria (southern Italy).
984 Journal of Structural Geology, 10(4), 373–381. https://doi.org/10.1016/0191-8141(88)90015-6
985 Di Rosa, M., Frassi, C., Malasoma, A., Marroni, M, Meneghini, F., & Pandolfi, L. (2020a). Syn-
986 exhumation coupling of oceanic and continental units along the western edge of the Alpine
987 Corsica: A review. Ofioliti, 2020, 45 (2), 71-102 - doi: 10.4454/ofioliti.v45i2.533
988 Di Rosa M., Meneghini F., Marroni M., Frassi C., & Pandolfi L. (2020b). The coupling of high-pressure
989 oceanic and continental units in Alpine Corsica: evidence for syn-exhumation tectonic erosion at
990 the roof of the plate interface. Lithos, 354-355, 105328,
991 https://doi.org/10.1016/j.lithos.2019.105328.
992 Di Rosa, M., De Giorgi, A., Marroni, M., and Vidal, O. (2017). Syn- convergence exhumation of
993 continental crust: Evidence from structural and metamorphic analysis of the Monte Cecu area,
994 Alpine Corsica (Northern Corsica, France). Geological Journal, 52, 919–937, doi:
995 10.1002/gj.2857Di
996 Di Vincenzo G., Folco L., Suttle M.D., Brase L. & Harvey R. P. (2021). Multi-collector $^{40}Ar/^{39}Ar$ dating
997 of microtektites from Transantarctic Mountains (Antarctica): a definitive link with the
998 Australasian tektite/microtektite strewn field. Geochimica Cosmochimica Acta, doi:
999 doi.org/10.1016/j.gca.2021.01.046
1000 Di Vincenzo, G., Carosi, R. & Palmeri, R. (2004). The relationship between tectono-metamorphic
1001 evolution and argon isotope records in white mica: constraints from in-situ ^{40}Ar–^{39}Ar laser
1002 analysis of the Variscan basement of Sardinia. *Journal of Petrology, 45*, 1013–1043, doi: 10.1093/
1003 petrology/egh002
1004 Di Vincenzo G., Grande A., Prosser G., Cavazza W., & DeCelles, P.G. (2016). $^{40}Ar/^{39}Ar$ laser dating of
1005 ductile shear zones from central Corsica (France): Evidence of Alpine (middle to late Eocene) syn-
1006 burial shearing in Variscan granitoids. *Lithos, 262,* 369-383.
1007 Doglioni, C., Gueguen, E., Sabat, F., & Fernandez, M. (1997). The Western Mediterranean
1008 extensional basins and the Alpine orogen. Terra Nova, 9(3), 109–112.
1009 https://doi.org/10.1046/j.1365-3121.1997.d01-18.x
1010 Doglioni, C., Mongelli, F., & Pialli, G. (1998). Boudinage of the Alpine belt in the Apenninic back-arc
1011 Memorie della Società Geologica Italiana, 52, 457-468
1012 Durand-Delga, M., 1984. Principaux traits de la Corse Alpine et corrélations avec les Alpes Ligures.
1013 *Memorie della Società Geologica Italiana, 28*, 285–329.
1014 Faccenna C, Becker, TW, Lucente, FP, Jolivet, L, & Rossetti, F. (2001). History of subduction and back-
1015 arc extension in the Central Mediterranean. *Geophysical Journal International*, *145*, 809–820,
1016 doi: 10.1046/j.0956-540x.2001.01435.x.
1017 Faccenna, C., Piromallo, C., Crespo-Blanc, A., Jolivet, L. & Rossetti, F. (2004). Lateral slab deformation
1018 and the origin of the western Mediterranean arc. Tectonics, 23, TC1012,
1019 doi:10.1029/2002TC001488

Fellin, M.G., Vance, J.A., Garver, J.I., & Zattin, M. (2006). The thermal evolution of Corsica as recorded by zircon fission-tracks. *Tectonophysics, 421*, 299–317.

Ferrandini, M., Ferrandini, J., Loye-Pylot, M.D., Butterlin, J., Cravette, J., & Janin, M.C. (1998). Le Miocène du Bassin de Saint-Florent (Corse): Modalités de la transgression du Burdigalien Superieur et mise en évidence du Serravalien. Geobios, 31, 125–137.

Ferrandini, J., Ferrandini, M., Rossi, P., & Savary-Sismondini, B. (2010). Definition and dating of the Venaco Formation (Corsica, France): a Priabonian gravity flow deposit. Comptes Rendus Geosciences, 342, 921–929.

Frassi, C., Di Rosa, M., Farina, F., Pandolfi, L., & Marroni, M. (2022): Anatomy of a deformed upper crust fragment from western Alpine Corsica (France): insights into continental subduction processes. International Geology Review. doi:: 10.1080/00206814.2022.2031315

Fuhrman, M.L., & Lindsley, D.H. (1988). Ternary-feldspar modeling and thermometry. American Mineralogist, 73, 201-215

Fusseis, F., & Handy, M.R. (2008). Micromechanisms of shear zone propagation at the brittle–viscous transition. *Journal of Structural Geology, 30*, 1242-1253, doi: 10.1016/j.jsg.2008.06.005.

Fusseis, F., Handy, M.R., & Schrank, C. (2006) Networking of shear zones at the brittle-to-viscous transition (Cap de Creus, NE Spain). *Journal of Structural Geology, 28*, 1228-1243.

Garfagnoli, F., Menna, F., Pandeli, E., & Principi, G. (2009). Alpine metamorphic and tectonic evolution of the Inzecca-Ghisoni area (southern Alpine Corsica, France). *Geological Journal*, 44, 191–210.

Gibbons, W., & Horak, J. (1984). Alpine metamorphism of Hercynian horneblende granodiorite beneath the blueschist facies Schistes Lustrés nappe of NE Corsica. Journal of Metamorphic Geology, 2, 95-113.

Gonçalves, P., Oliot, E., Marquer, D., & Connolly, J. A. D. (2012). Role of chemical processes on shear zone formation: an example from the Grimsel metagranodiorite (Aar massif, Central Alps). Journal of Metamorphic Geology, 30(7), 703-722.

Gueydan, F., Leroy, Y.M., Jolivet, L., & Agard, P. (2003). Analysis of continental midcrustal strain localization induced by microfracturing and reaction softening. *Journal of Geophysical Research 108*, doi:10.1029/2001JB000611.

Handy, M.R., Schmid, S., Bousquet, R., Kissling, E., & Bernoulli, D. (2010). Reconciling platetectonic reconstructions of Alpine Tethys with geological–geophysical record of spreading and subductions in the Alps. Earth-Science Reviews. http://dx.doi.org/10.1016/j.earscirev.2010.06.002.

Hawthorne, F. C., Oberti, R., Harlow, G. E., Maresch, W. V., Martin, R. F., Schumacher, J. C., & Welch, M. D. (2012). Nomenclature of the amphibole supergroup. American Mineralogist, 97(11-12), 2031-2048.

Heymes, T., Monié, P., Arnaud, N., Pêcher, A., Bouillin, J. P., & Compagnoni, R. (2010). Alpine tectonics in the Calabrian-Peloritan belt (southern Italy): New 40Ar/39Ar data in the Aspromonte Massif area. Lithos, 114(3–4), 451–472. https://doi.org/10.1016/j. lithos.2009.10.011.

Holyoke, C.W., Tullis, J., 2006. Mechanisms of weak phase interconnection and the effects of phase strength contrast on fabric development. J. Struct. Geol. 28, doi: 10.1016/j.jsg.2006.01.008.

Holland, T.J.B., & Powell, R. (2011) An improved and extended internally consistent thermodynamic dataset for phases of petrological interest, involving a new equation of state for solids. Journal of Metamorphic Geology 29:333-383. doi:10.1111/j.1525-1314.2010.00923.x

Holland, T.J.B., Green, E.C.R., Powell, R. (2018). Melting of Peridotites through to Granites: A Simple Thermodynamic Model in the System KNCFMASHTOCr, *Journal of Petrology*, *59*, 881–900, https://doi.org/10.1093/petrology/egy048

1067 Janecke, S.U. & Evans, J.P. (1988). Feldspar-influenced rock rheologies. Geology, 16, 1064-
1068 1067.
1069 Johnson, S., Marsh, J., & Vernon, R. (2008). From tonalite to mylonite: coupled mechanical and
1070 chemical processes in foliation development and strain localization. In: (Ed.) Declan De Paor,
1071 *Journal of the Virtual Explorer, 30*, doi: 10.3809/jvirtex.2009.00208
1072 Jolivet, L., Dubois, R., Fournier, M., Goffé, B., Michard, A., Jourdan, C. (1990). Ductile extension in
1073 Alpine Corsica. Geology, 18, 1007–1010.
1074 Jolivet, L., Faccenna, C., Goffé, B., Mattei, M., Rossetti, F., Brunet, C., Storti, F., Funiciello, C., Cadet,
1075 J.P., D'Agostino, N., & Parra, T. (1998). Mid crustal shear zones in postorogenic extension:
1076 examples from the northern Tyrrhenian Sea case. Journal of Geophysical Research 103, 12123–
1077 12160.
1078 Jolivet, L., & Faccenna, C. (2000). Mediterranean extension and the Africa-Eurasia collision.
1079 Tectonics, 19(6), 1095–1106. https://doi.org/10.1029/2000TC900018
1080 Jolivet, L., Baudin, T., Calassou, S., Chevrot, S., Ford, M., Issautier, B., Lasseur, E., Masini, E.
1081 Manatschal, G., Mouthereau, F. Thinon, I., & Vidal O. (2021). Geodynamic evolution of a wide
1082 plate boundary in the Western Mediterranean, near-field versus far-field interactions. Bulletin
1083 de la Société Géologique de France, 192 doi: https://doi.org/10.1051/bsgf/2021043
1084 Kuiper K. F., Deino A., Hilgen F. J., Krijgsman W., Renne P. R. & Wijbrans J. R. (2008). Synchronizing
1085 rock clocks of earth history. *Science, 320*, 500–504.
1086 Lacombe, O. & Bellahsen, N. (2016). Thick-Skinned tectonics and basement-involved fold-thrust
1087 belts: Insight from selected Cenozoic orogens. *Geological Magazine, 153*, 763–810.
1088 Lacombe, O., Jolivet, L. (2005). Structural and kinematic relationships between Corsica and the
1089 Pyrenees-Provence domain at the time of the Pyrenean orogeny. *Tectonics, 24*.
1090 Lee J. Y., Marti K., Severinghaus J. P., Kawamura K., Yoo H. S., Lee J. B. & Kim J. S. (2006). A
1091 redetermination of the isotopic abundances of atmospheric Ar. *Geochimica Cosmochimica Acta,*
1092 *70*, 4507–4512.
1093 Li, B., & Massonne, H. J. (2018). Two Tertiary metamorphic events recognized in high-pressure
1094 metapelites of the Nevado-Filabride Complex (Betic Cordillera, S Spain). Journal of Metamorphic
1095 Geology, 36(5), 603–630. https://doi.org/10.1111/jmg.12312
1096 Locock, A. J. (2014). An Excel spreadsheet to classify chemical analyses of amphiboles following the
1097 IMA 2012 recommendations. Computers & Geosciences, 62, 1-11.
1098 Lowry, A. R. & Perez-Gussinyé, M. (2011). The role of crustal quartz in controlling Cordilleran
1099 deformation. *Nature, 471*, 353-357.
1100 Lustrino, M., Morra, V., Fedele, L., & Franciosi, L. (2009). Beginning of the Apennine subduction
1101 system in central western Mediterranean: Constraints from Cenozoic “orogenic” magmatic
1102 activity of Sardinia, Italy. *Tectonics, 28*, doi: 10.1029/2008tc002419.
1103 Lustrino M., Fedele L., Agostini S., Di Vincenzo G., Morra V. (2017) Eocene-Miocene igneous activity
1104 in Provence (SE France): 40Ar/39Ar data, geochemical-petrological constraints and geodynamic
1105 implications. Lithos 288-289, 72-90. http://dx.doi.org/10.1016/j.lithos.2017.07.008
1106 Maggi, M., Rossetti, F., Corfu, F., Theye, T., Andersen, T.B., Faccenna, C. (2012). Clinopyroxene-rutile
1107 phyllonites from the East Tenda Shear Zone (Alpine Corsica, France): pressure-temperature-time
1108 constraints to the Alpine reworking of Variscan Corsica. *Journal of the Geological Society, London*,
1109 169, 723–732, doi:10.1144/jgs2011-120.
1110 Maggi, M., Rossetti, F., Ranalli, G., & Theye, T. (2014). Feedbacks between fluid infiltration and
1111 rheology along a regional ductile-to-brittle shear zone: the East Tenda Shear Zone (Alpine Corsica.
1112 *Tectonics, 33*, 253-280.
1113 Malasoma, A., Marroni, M., Musumeci, G., & Pandolfi, L. (2006). High pressure mineral assemblage
1114 in granitic rocks from continental units, Alpine Corsica. France. *Geological Journal 41*, 49–59.

1115 Malasoma, A., & Marroni, M. (2007). HP/LT metamorphism in the Volparone Breccia (Northern
1116 Corsica, France): evidence for involvement of the Europe/Corsica continental margin in the
1117 Alpine subduction zone. *Journal of Metamorphic Geology 25*, 529–545.
1118 Malasoma A., Morelli G., Di Rosa M., Marroni M., Pandeli E., Principi, G. & Pandolfi L. (2020). The
1119 stratigraphic and structural setting of metamorphic continental units from Alpine Corsica: clues
1120 from the area between Asco and Golo valleys (Central Corsica, France). Journal of Maps, 16, 313-
1121 323.
1122 Malusà, M. G., Faccenna, C., Baldwin, S. L., Fitzgerald, P. G., Rossetti, F., Balestrieri, M. L., Danisik,
1123 M., Ellero, A., Ottira, G., & Piromallo, C. (2015). Contrasting styles of (U) HP rock exhumation
1124 along the Cenozoic Adria-Europe plate boundary (Western Alps, Calabria, Corsica).
1125 Geochemistry, Geophysics, Geosystems, 16(6), 1786–1824. https://doi.org/10.
1126 1002/2015GC005767
1127 Mancktelow, NS, & Pennacchioni, G. (2005) The control of precursor brittle fracture and fluid-rock
1128 interaction on the development of single and paired ductile shear zones *Journal of Structural*
1129 *Geology, 27,* 645-661.
1130 Marrone, S., Monié, P., Rossetti, F., Lucci, F., Theye, T., Bouybaouene, M. L., & Zaghloul, M. N. (2021a). The
1131 Pressure-Temperature-time-deformation history of the Beni Mzala unit (Upper Sebtides, Rif belt,
1132 Morocco): Refining the Alpine tectono-metamorphic evolution of the Alboran Domain of the Western
1133 Mediterranean. Journal of Metamorphic Geology, 39, 591–615. https://doi.org/10.1111/jmg.12587.
1134 Marrone, S., Monie, P., Rossetti, F., Aldega, L., Bouybaouene, M., Charpentier, D., et al. (2021b). Timing of
1135 Alpine orogeny and postorogenic extension in the Alboran Domain, inner Rif chain, Morocco. Tectonics,
1136 40, e2021TC006707. https://doi. org/10.1029/2021TC006707
1137 Marroni, M., Meneghini, F., & Pandolfi, L. (2017). A revised subduction inception model to explain the
1138 Late Cretaceous, double-vergent orogen in the precollisional western Tethys: Evidence from the
1139 Northern Apennines. Tectonics, 36, 2227–2249. https://doi.org/10.1002/2017TC004627
1140 Martin A.J., Rubatto D., Vitale Brovarone A. and Hermann J., 2011. Late Eocene lawsonite-eclogite
1141 facies metasomatism of a granulite sliver associated to ophiolites in Alpine Corsica. *Lithos, 125*,
1142 620-640.
1143 McAleer, R. J., Bish, D. L., Kunk, M. J., Sicard, K. R., Valley, P. M., Walsh, G. J., et al. (2017). Reaction
1144 softening by dissolution-precipitation creep in a retrograde greenschist facies ductile shear zone, New
1145 Hampshire, USA. *Journal of Metamorphic Geology*, 35(1), 95– 119.
1146 Min K., Mundil R., Renne P. R. & Ludwig K. R. (2000) A test for systematic errors in $^{40}Ar/^{39}Ar$
1147 geochronology through comparison with U/Pb analysis of a 1.1-Ga rhyolite. *Geochimica*
1148 *Cosmochimica Acta, 64*, 73–98.
1149 Molli, G., Malavieille, J. (2010). Orogenic processes and the Corsica/Apennines geodynamic
1150 evolution: insights from Taiwan. *International Journal of Earth Sciences,* 100, 1207–1224,
1151 doi:10.1007/s00531-010-0598-y.
1152 Molli, G., Tribuzio, R., Marquer, D. (2006). Deformation and metamorphism at the eastern border
1153 of the Tenda Massif (NE Corsica): a record of subduction and exhumation of continental crust.
1154 *Journal of Structural Geology, 28*, 1748–1766, doi:10.1016/j.jsg.2006.06.018.
1155 Mouthereau, F., Watts, A.B., & Burov, E. (2013). Structure of orogenic belts controlled by lithosphere
1156 age. *Nature Geosciences, 6*,785–789, doi: 10.1038/ngeo1902.
1157 Nemčok, M., Mora, A. and Cosgrove, J. W. (Eds), 2013. Thick-Skin-Dominated Orogens: From Initial
1158 Inversion to Full Accretion. Geological Society of London Special Publication, 377, doi
1159 10.1144/SP377. Published, 12/2013.
1160 O'Hara, K. (1990). State of strain in mylonites from the western Blue Ridge province, southern
1161 Appalachians: the role of volume loss. Journal of Structural Geology 12, 419-430.
1162 O'Hara, K. (2007). Reaction weakening and emplacement of crystalline thrusts: Diffusion control on
1163 reaction rate and strain rate. Journal of Structural Geology, 29, 1301e1314

Papeschi, S., & Musumeci, G. (2019). Fluid-assisted strain localization in quartz at the brittle/ductile transition. *Geochemistry, Geophysics, Geosystems*, 20, doi: 10.1029/2019GC008270

Passchier, C. W., & Trouw, R. A. J. (2010). Microtectonics (2nd ed.). Springer.

Penniston-Dorland, S. C., Kohn, M. J., & Manning, C. E. (2015). The global range of subduction zone thermal structures from exhumed blueschists and eclogites: Rocks are hotter than models. Earth and Planetary Science Letters, 428, 243–254. https://doi.org/10.1016/j.epsl.2015.07.031

Pfiffner, O.A. (2006). Thick-Skinned and thin-skinned styles of continental contraction. *Geological Society of America Special Paper 414*, 157–177.

Platt, J. P. & Compagnoni, R. (1990). Alpine ductile deformation and metamorphism in a Calabrian basement nappe (Aspromonte, south Italy). *Eclogae geologicae Helvetiae 83(1)*, 41-58.

Principi, G., & Treves, B. (1984). Il sistema Corso-Appennino come prisma di accrezione. Riflessi sul problema generale del limite Alpi-Appennino. Memorie-Società Geologica Italiana, 28, 529–576.

Rosenbaum, G., Lister, G.S., & Duboz, C. (2002). Relative motions of Africa, Iberia and Europe during Alpine orogeny. *Tectonophysics, 359*, 117–129.

Rossetti, F., Faccenna, C., Goffé, B., Monié, P., Argentieri, A., Funiciello, R., & Mattei, M. (2001). Alpine structural and metamorphic signature of the Sila Piccola Massif nappe stack (Calabria, Italy): Insights for the tectonic evolution of the Calabrian Arc. Tectonics, 20(1), 112–133, doi: 10.1029/2000TC900027

Rossetti, F., Faccenna, C., Jolivet, L., Funiciello, R., Goffé, B., Tecce, F., & Vidal, O. (2001). Structural signature and exhumation P-T-t path of the Gorgona blueschist sequence (Tuscan Archipelago,Italy). Ofioliti, 26, 175–186.

Rossetti, F., Glodny, J., Theye, T., & Maggi, M. (2015). Pressure–temperature–deformation–time of the ductile Alpine shearing in Corsica: From orogenic construction to collapse. Lithos, 218, 99–116, doi: 10.1016/j.lithos.2015.01.011

Rossetti, F., Goffé, B., Monié, P., Faccenna, C., & Vignaroli, G. (2004). Alpine orogenic P-T-t-deformation history of the Catena Costiera area and surrounding regions (Calabrian Arc, southern Italy): The nappe edifice of north Calabria revised with insights on the Tyrrhenian-Apennine system formation. Tectonics, 23(6), doi: 10.1029/2003TC001560.

Rossi, P., Durand-Delga, M., Caron, J.M., Guieu, G., Conchon, O., Libourel, G., & Loÿe-Pilot, M.D., avec la collaboration de Ohnenstetter D., Ohnenstetter M., Ferrandini J., Rouire J., Dominici R., (1994). Notice esplicative, Carte géol. France (1/50000), feuille Corte (1110). Orléans: BRGM, 150 pp.

Schenk, V. (1980). U-Pb and Rb-Sr radiometric dates and their correlation with metamorphic events in the granulite basement of the Serre, southern Calabria (Italy), *Contribution to Mineralogy and Petrology, 73*, 23-38.

Stip, M, Stunitz, H, Heilbronner, R, & Schmid, SM. (2002). The eastern Tonale fault zone: a “natural laboratory” for crystal plastic deformation for quartz over a temperature range from 250 to 700°C. Journal of Structural Geology, 24, 1861-1884

Thomson, S. N. (1994). Fission track analysis of the crystalline basement rocks of the Calabrian Arc, southern Italy: evidence of Oligo-Miocene late orogenic extension and erosion, Tectonophysics, 238, 331-352

Tribuzio, R., & Giacomini, F. (2002). Blueschist facies metamorphism of peralkaline rhyolites from the Tenda crystalline massif (northern Corsica): evidence for involvement in Alpine subduction event?. *Journal of Metamorphic Geology, 20*, 513–526.

Turco, E., Macchiavelli, C., Mazzoli, S., Schettino, A., & Pierantoni, P.P. (2012). Kinematic evolution of Alpine Corsica in the framework of Mediterranean mountain belts. *Tectonophysics, 579*, 193–206.

van Hinsbergen, D., Vissers, R., & Spakman, W. (2014). Origin and consequences of western Mediterranean subduction, rollback, and slab segmentation. *Tectonics*, 33, 393–419.

Vignaroli, G., Minelli, L., Rossetti, F., Balestrieri, M. L., & Faccenna, C. (2012). Miocene thrusting in the eastern Sila Massif: Implication for the evolution of the Calabria-Peloritani orogenic wedge (southern Italy). Tectonophysics, 538, 105–119. https://doi.org/10.1016/j.tecto.2012.03.011

Vignaroli, G., Rossetti, F., Theye, T., & Faccenna, C. (2008). Styles and regimes of orogenic thickening in the Peloritani Mountains (Sicily, Italy): New constraints on the tectono-metamorphic evolution of the Apennine belt. Geological Magazine, 145(4), 552–569. https://doi.org/10.1017/S0016756807004293

Villa, I.M., Bucher, S., Bousquet, R., Kleinhanns, I.C. & Schmid, S.M. (2014). Dating polygenetic metamorphic assemblages along a transect across the Western Alps. *Journal of Petrology, 55*, doi: 10.1093/ petrology/egu007

Vitale Brovarone, A., Beyssac, O., Malavieille, J., Molli, G., Beltrando, M., & Compagnoni R. (2013). Stacking and metamorphism of continuous segments of subducted lithosphere in a high-pressure wedge: The example of Alpine Corsica (France). *Earth Science Review, 116*, 35–56, doi:10.1016/j.earscirev.2012.10.003.

Vitale Brovarone, A., Herwartz, D. (2013). Timing of HP metamorphism in the Schistes Lustrés of Alpine Corsica: New Lu–Hf garnet and lawsonite ages. *Lithos, 172*, 175–191.

Whitney, D., & Evans B., (2010). Abbreviations for names of rock-forming minerals. *American Mineralogist, 95*, 185–187, doi:10.2138/am.2010.3371.

Wintsch, R.P., Christoffersen, R., & Kronenberg, A.K., (1995). Fluid-rock reaction weakening of fault zones. *Journal of Geophysical Research, 100*, 13,021e13,032.

Wintsch, R.P., Aleinikoff, J.N., & Yi, K. (2005). Foliation development and reaction softening by dissolution and precipitation in the transformation of granodiorite to orthogneiss, Glastonbury complex, Connecticut, U.S.A. Canadian Mineralogist, 43, 327-347.

White R.W., Powell R. & Clarke G.L., 2002. The interpretation of reaction textures in Fe-rich metapelitic granulites of the Musgrave Block central Australia: constraints from mineral equilibria calculations in the system K_2O-FeO-MgO-Al_2O_3-SiO_2-H_2O-TiO_2-Fe_2O_3. Journal of Metamorphic Geology, 20, 41–55

White, R. W., Powell, R., Holland, T. J. B., Johnson, T. E., & Green, E. C. R. (2014). New mineral activity–composition relations for thermodynamic calculations in metapelitic systems. Journal of Metamorphic Geology, 32(3), 261–286.

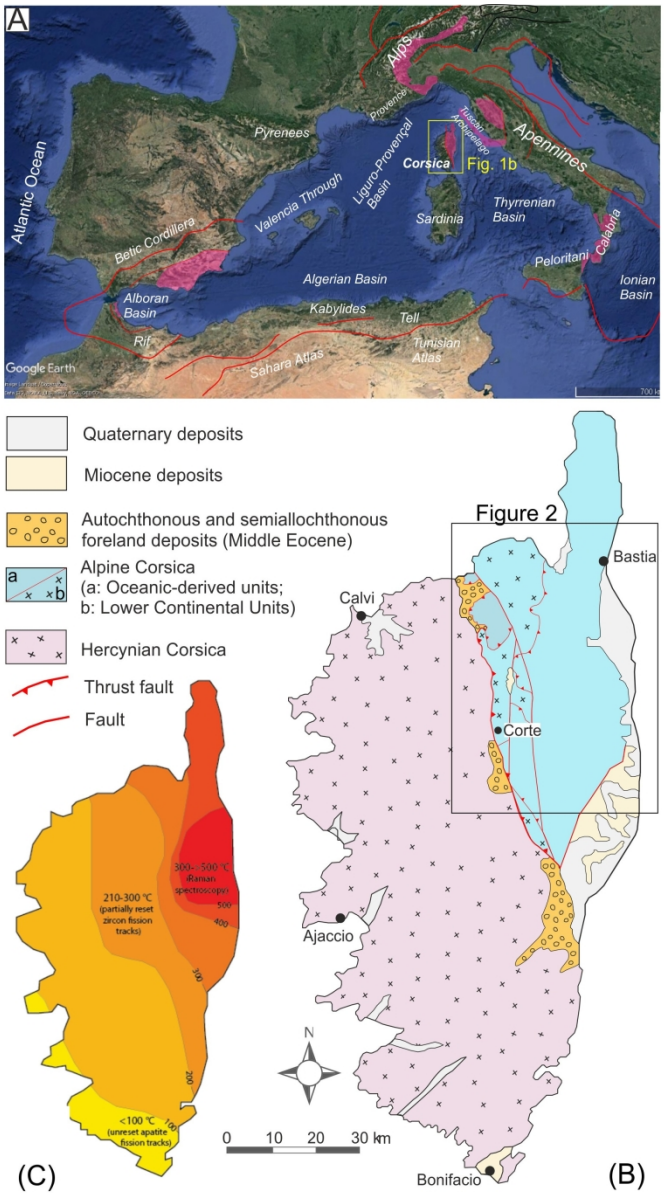

157x281mm (300 x 300 DPI)

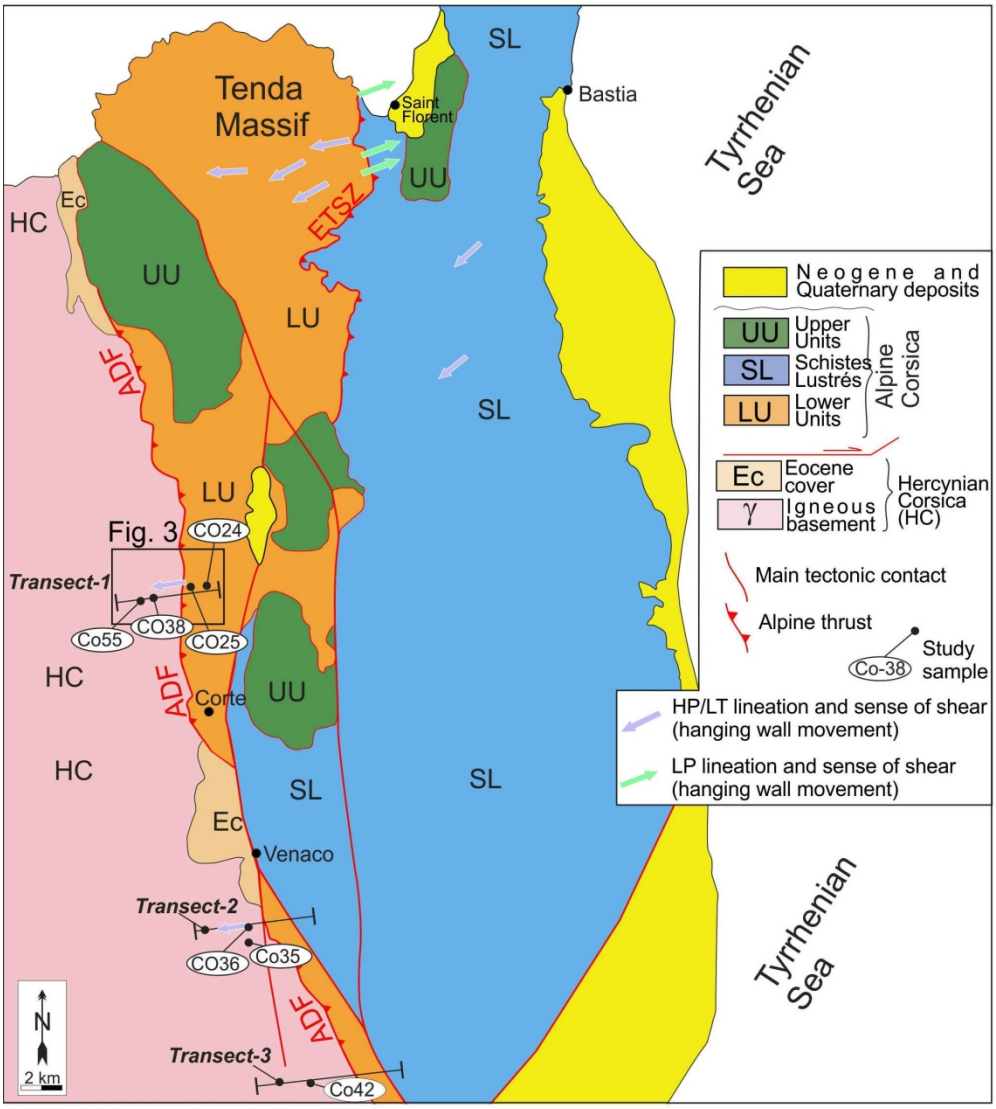

173x193mm (300 x 300 DPI)

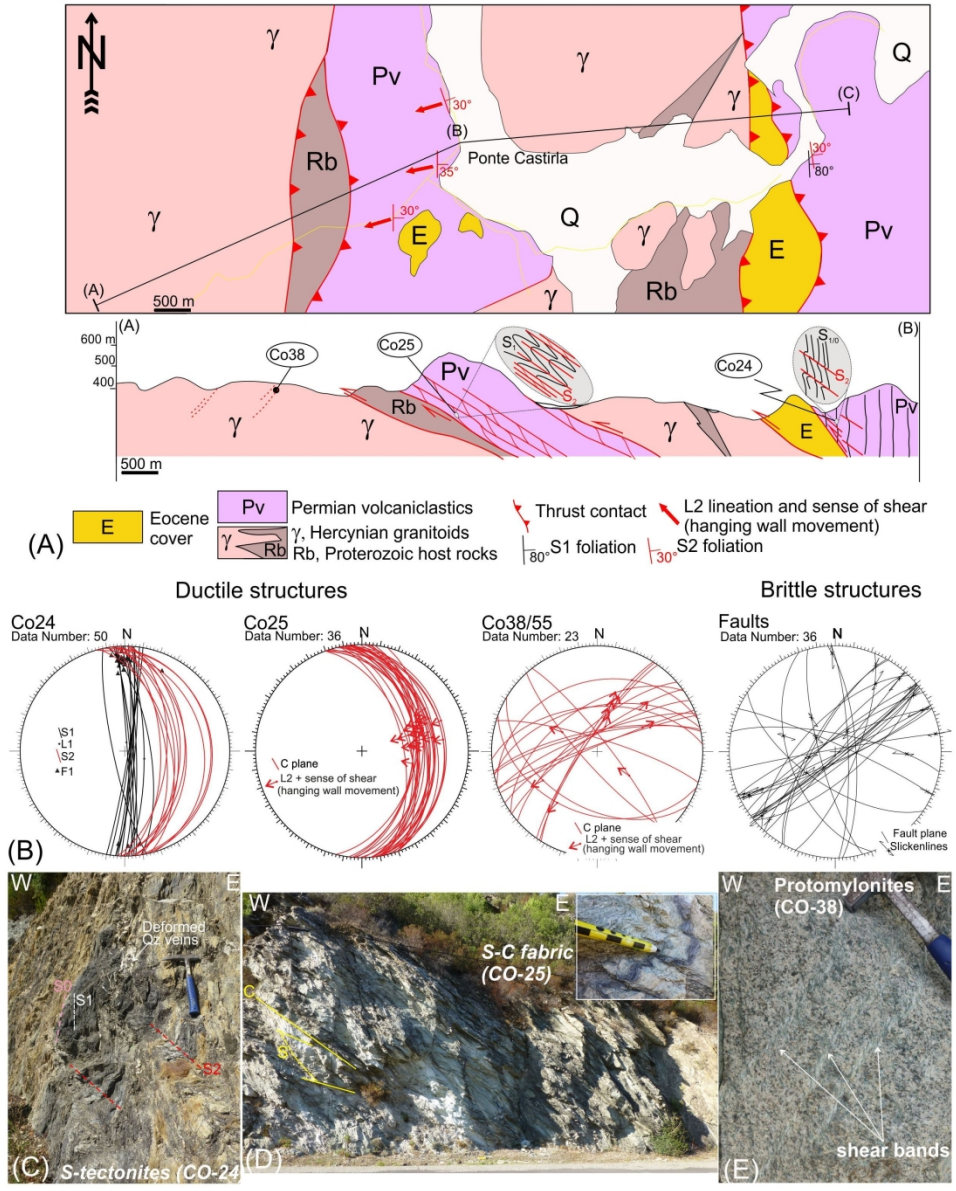

213x265mm (300 x 300 DPI)

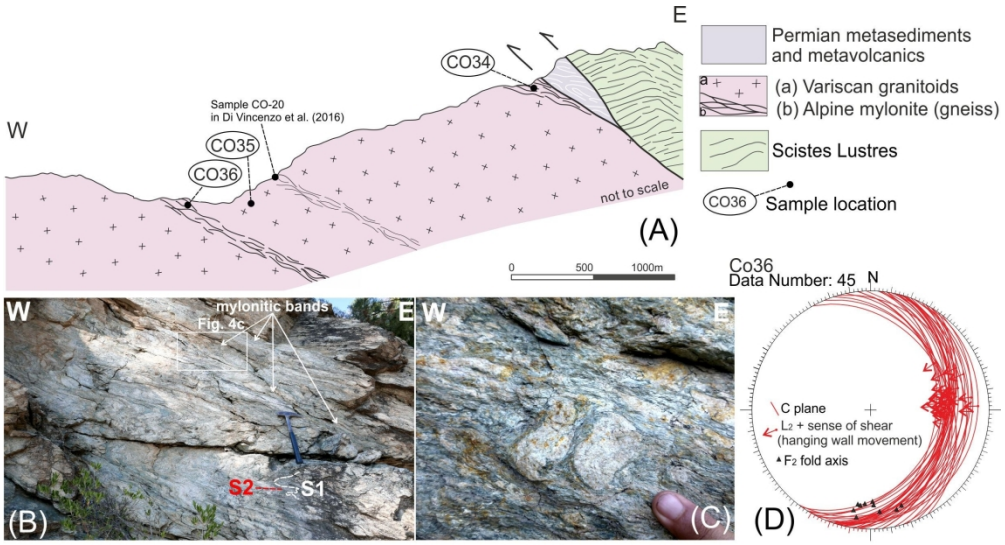

207x111mm (300 x 300 DPI)

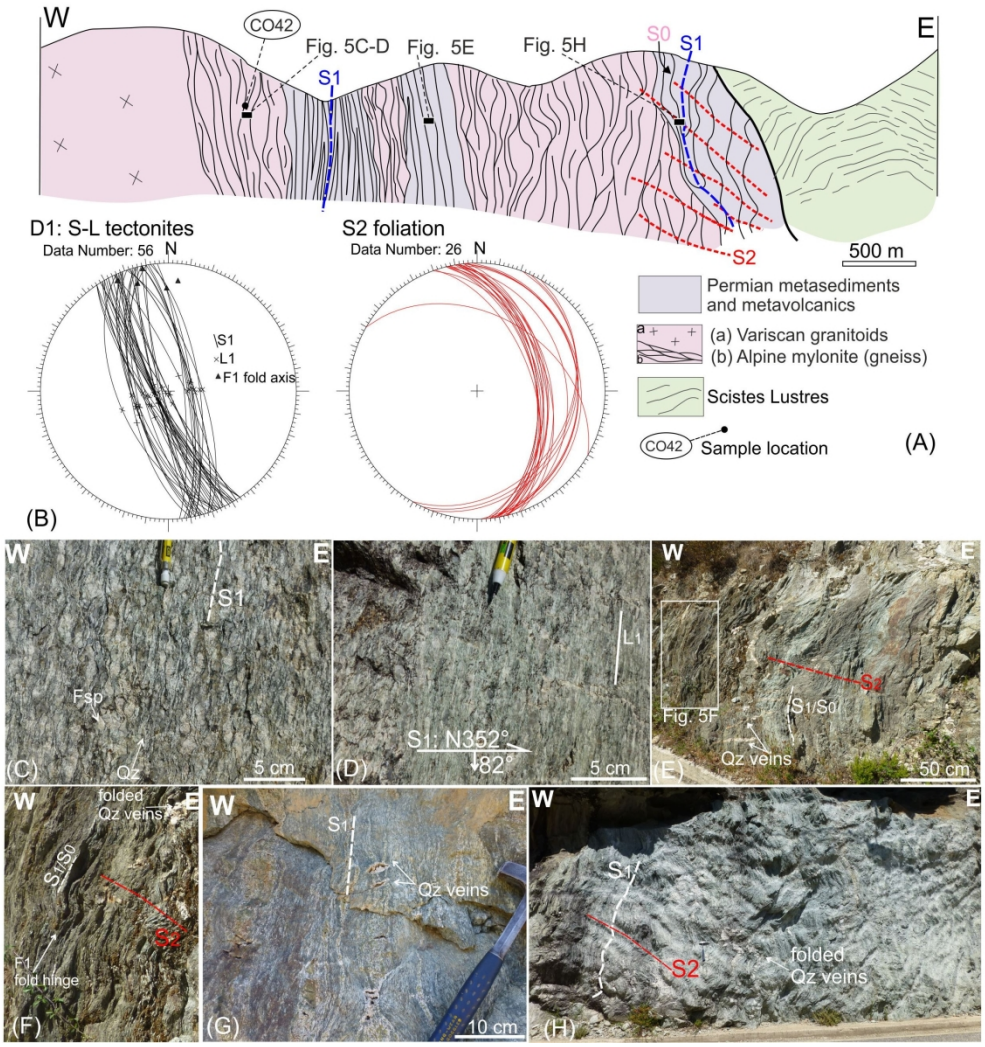

214x223mm (300 x 300 DPI)

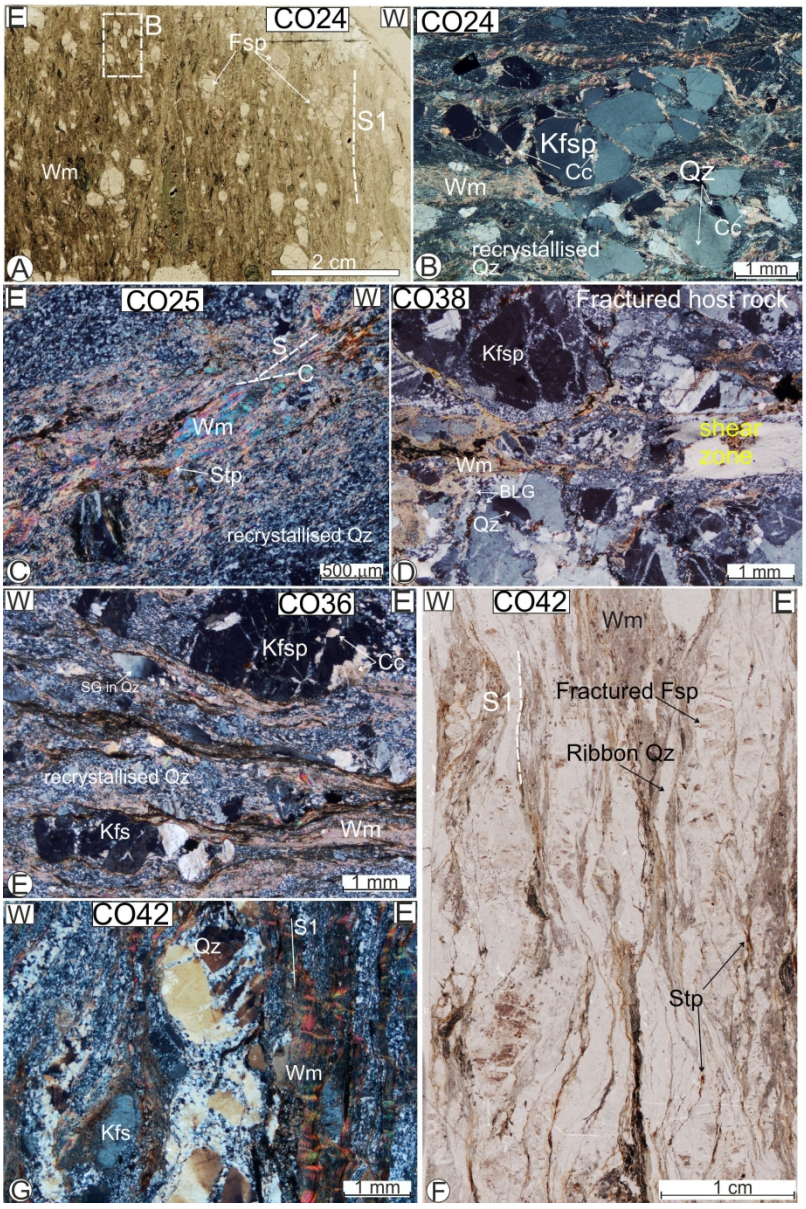

195x290mm (300 x 300 DPI)

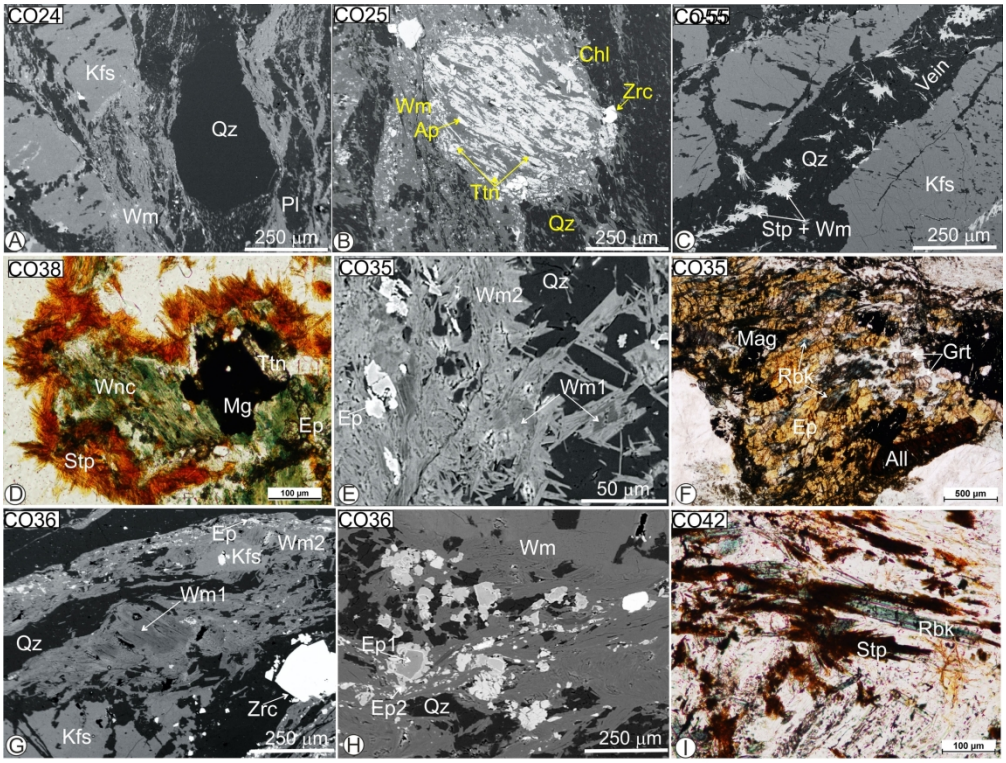

207x157mm (300 x 300 DPI)

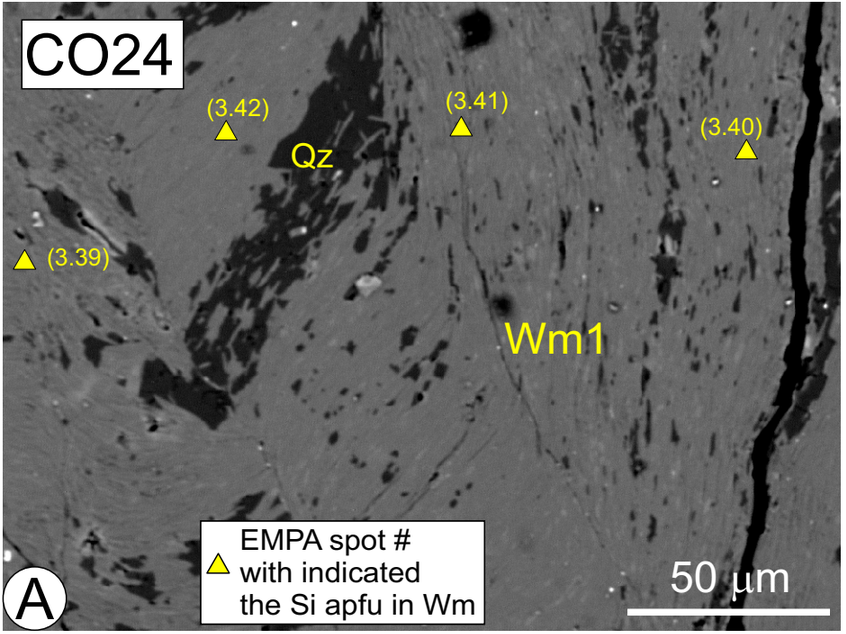
CO24
(3.42)
(3.41)
(3.40)
Qz
(3.39)
Wm1
EMPA spot #
with indicated
the Si apfu in Wm
50 μm
A

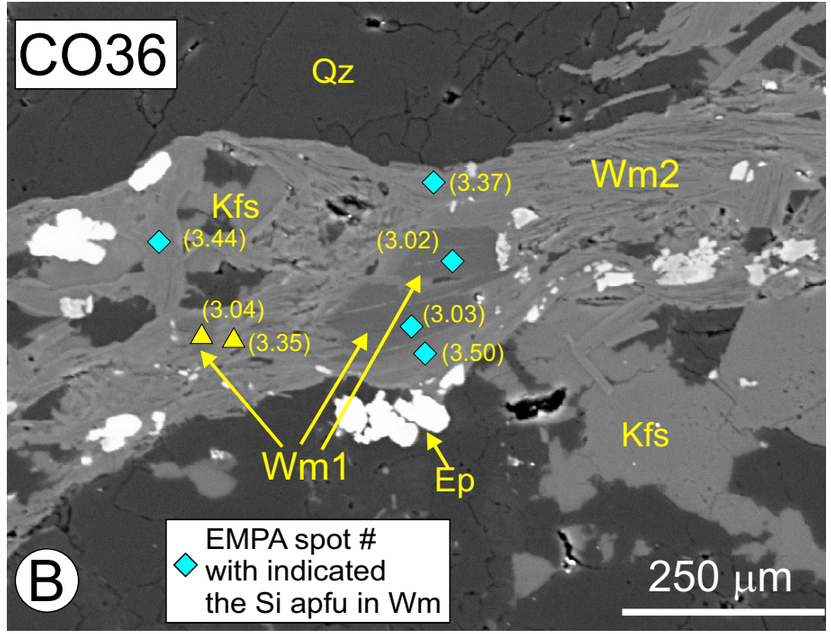
CO36
Qz
Wm2
(3.37)
Kfs
(3.44)
(3.02)
(3.04)
(3.03)
(3.35)
(3.50)
Wm1
Ep
Kfs
EMPA spot #
with indicated
the Si apfu in Wm
250 μm
B

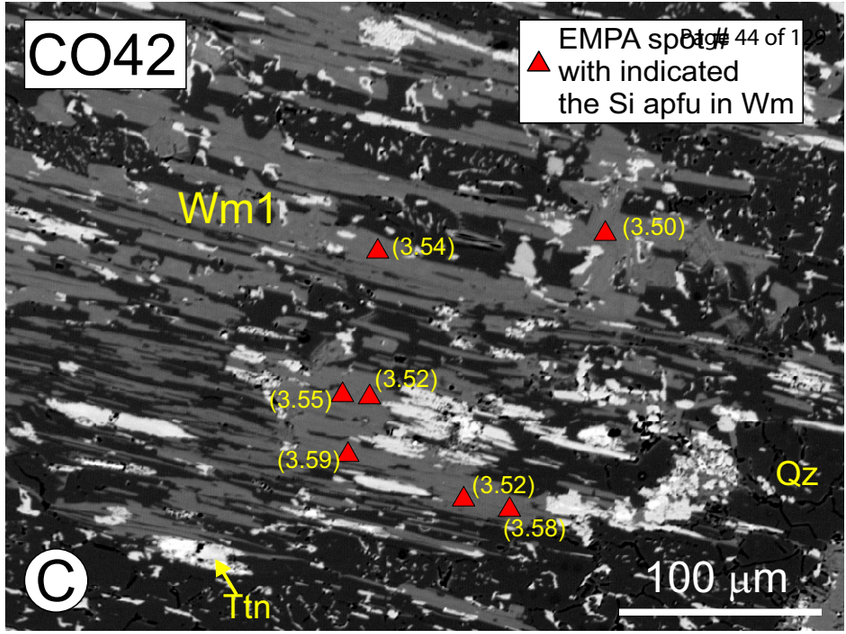
CO42
EMPA spot #
with indicated
the Si apfu in Wm
Wm1
(3.54)
(3.50)
(3.52)
(3.55)
(3.59)
(3.52)
(3.58)
Qz
Ttn
100 μm
C

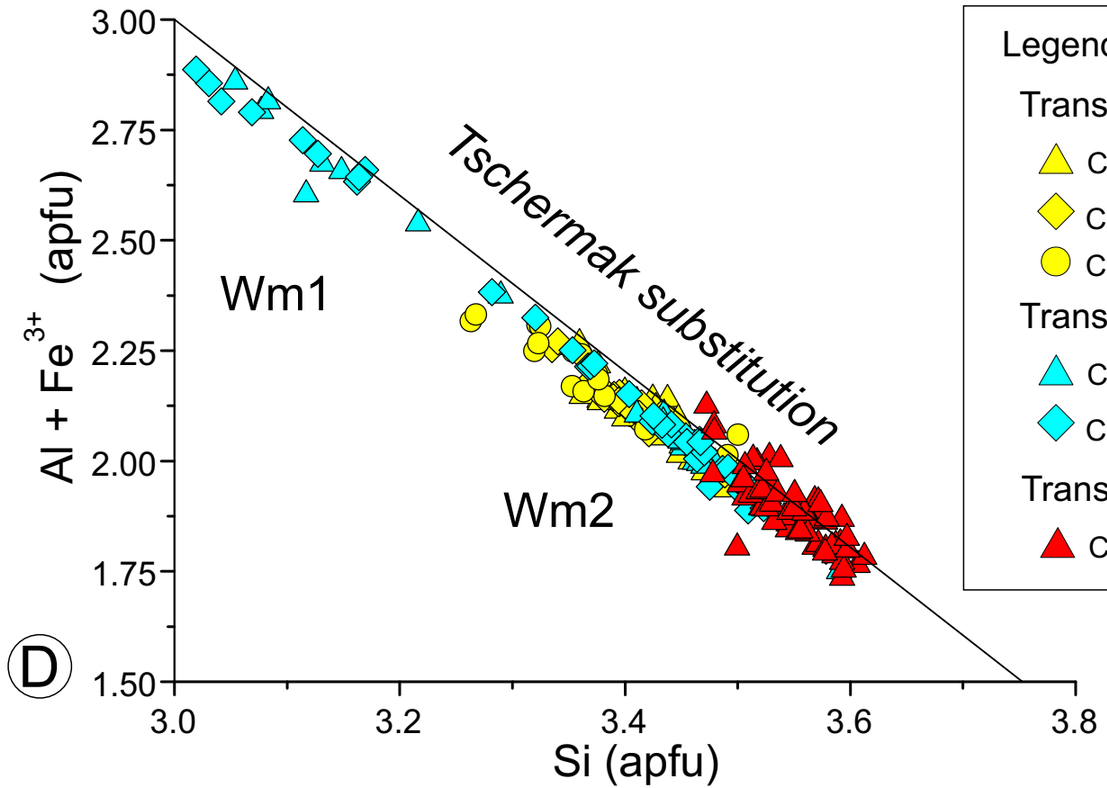
3.00
2.75
2.50
2.25
2.00
1.75
1.50
Al + Fe3+ (apfu)
3.0
3.2
3.4
3.6
3.8
Si (apfu)
Tschermak substitution
Wm1
Wm2
D

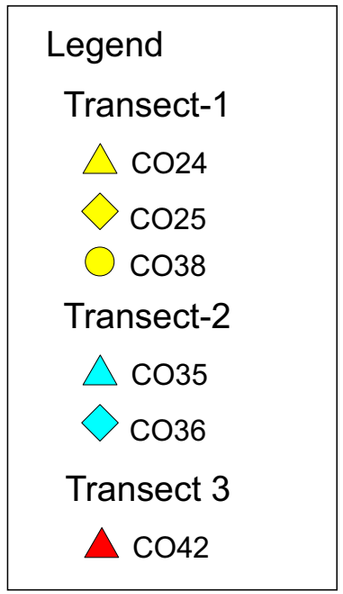
Legend
Transect-1
CO24
CO25
CO38
Transect-2
CO35
CO36
Transect 3
CO42

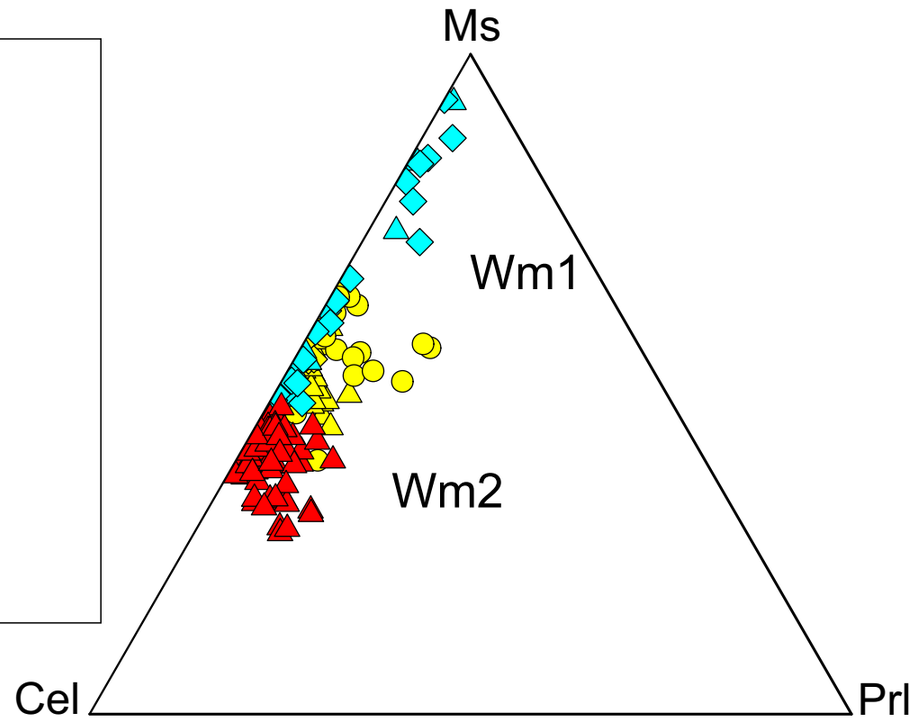
Ms
Wm1
Wm2
Cel
Prl

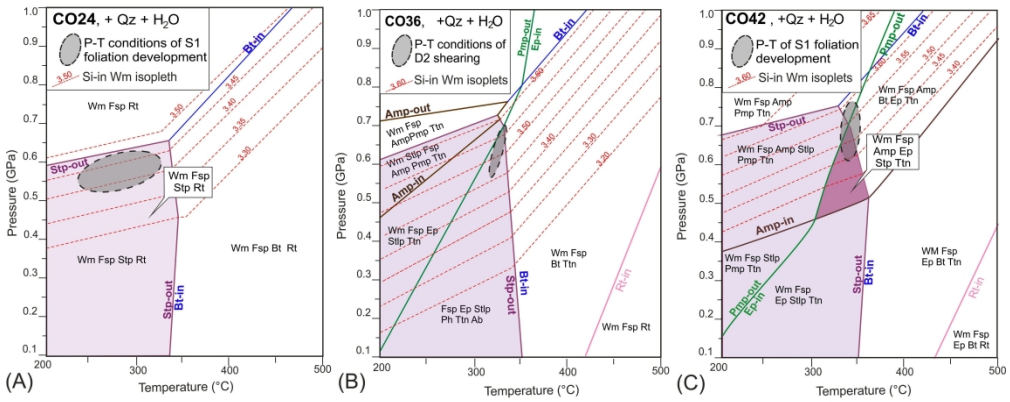

406x163mm (300 x 300 DPI)

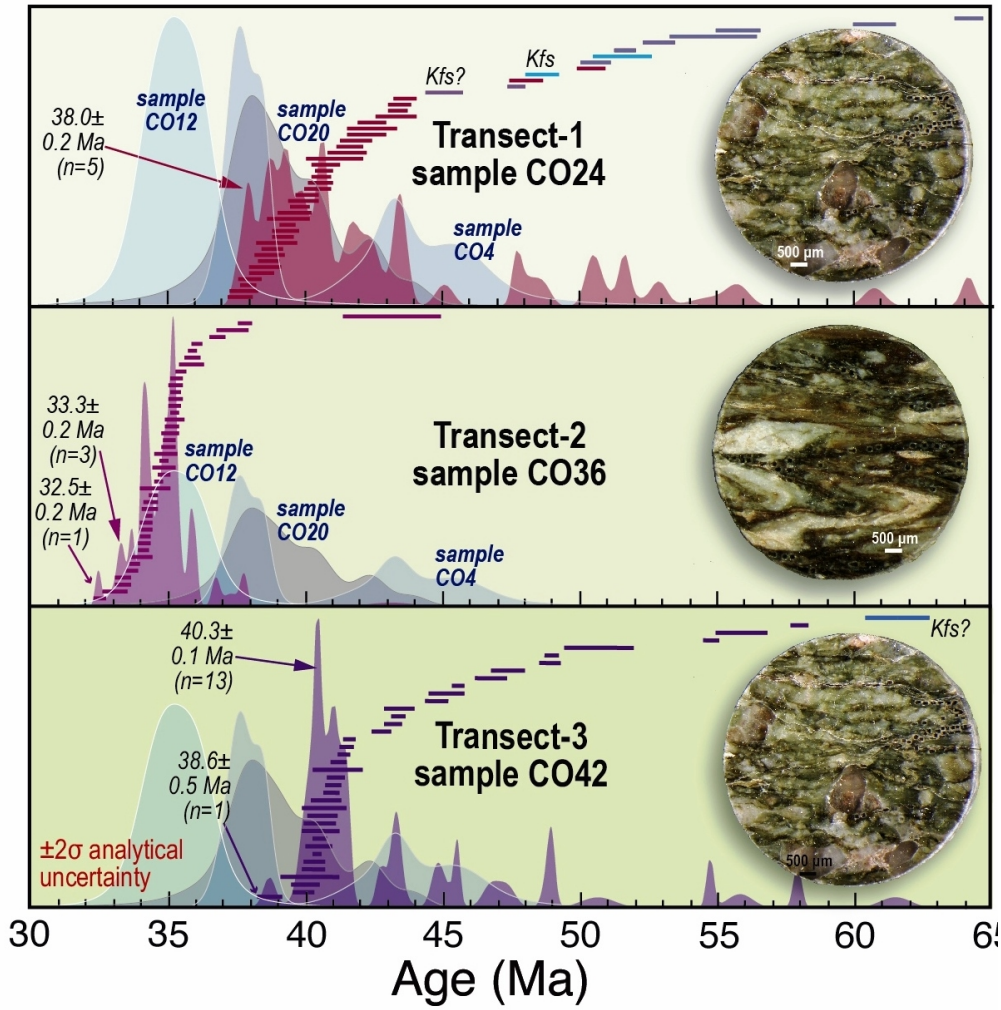

318x322mm (96 x 96 DPI)

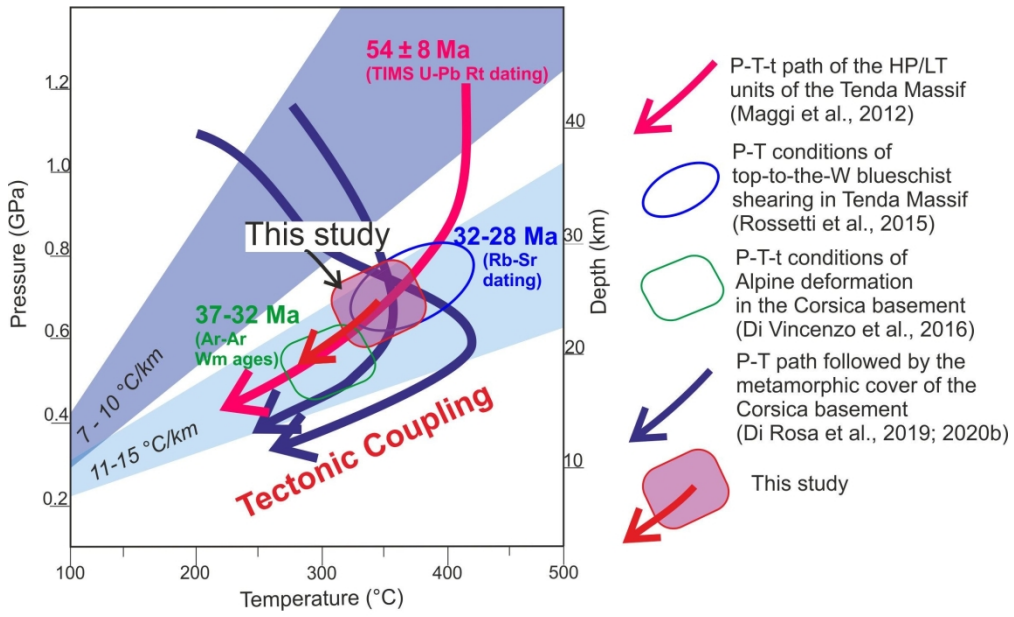

198x122mm (300 x 300 DPI)

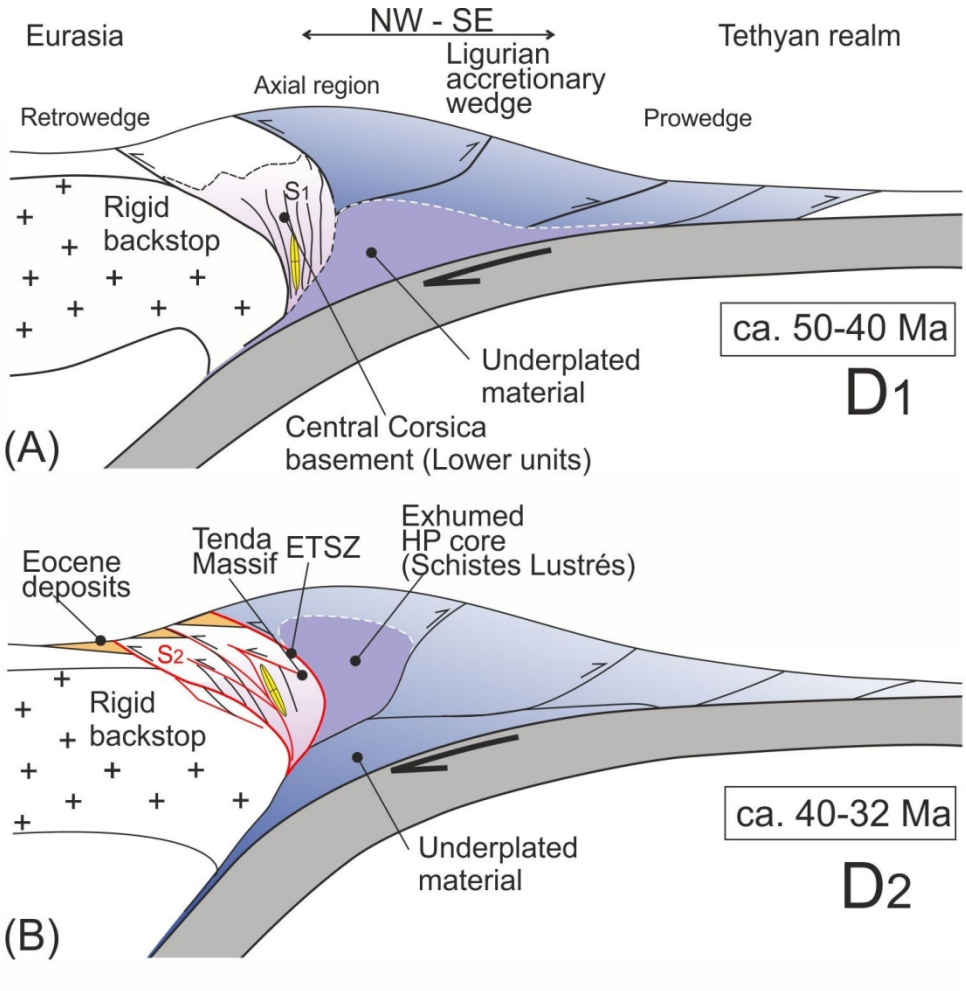

132x130mm (300 x 300 DPI)

Table 1 - List of the Studied Samples, with Geographical Location and Analytical Methods

Sample	Rock Type	Location		Metamorphic Assemblage	Analytical method		
		Latitude (°N)	Longitude (°W)		EMPA	ICP whole rock	$^{40}Ar/^{39}Ar$ in situ dating
CO24	Permian volcaniclastics	42°23' 09.8"	09° 10' 01.5"	Qz-Wm-Ab, Stp, Rt + Cb (late)	X	X	X
CO25	Permian volcaniclastics	42° 22' 52.1"	09°07'59.1"	Qz-Wm-Ab, Chl, Stp, Ep, Ttn, Ap + Cb (late)	X		
CO38	Granitoid	42° 22' 20.0"	09° 06' 44.8"	Qz-Wm-Ab, Stp, Ep, Ch, Ttn, Bt, Amp (Wnc), Ap + Ilv + Cb (late)	X		
Co55	Granitoid	42° 22' 19.4"	09° 06' 43.4"	Qz-Wm-Ab, Stp, Ep, Chl, Ttn, Bt, Ap + Cb (late)			
CO35	Granitoid	42° 10' 24.8"	09° 09' 45.5"	Qz-Wm-Ab, Stp,Ep, Amp (Rbk), Ttn, Ab + Grt (And-Grs), Ap + Cb (late)	X		
CO36	Granitoid	42° 11' 53.9"	09° 10' 17.0"	Qz-Wm-Ab, Stp, Ep, Ttn, Amp (Act), Cb (late)	X	X	X
CO42	Granitoid	42° 06' 12.8"	09° 15' 37.0"	Wm-Qz- Ab-Stp-Amp (Rbk), Ep, Ttn, Ap, Cb (late)	X	X	X

(*) Mineral abbreviations after Whitney and Evans (2010); Wm: white mica

Table 2 - Bulk and recalculated rock compositions used for pseudosection modelling

	XRF data			Recalculated(*)		
Sample	Co-24	Co-36	Co-42	Co-24	Co-36	Co-42
Rock Type	Metavolcanic	Granitoid	Granitoid			
SiO_2	72.08	74.70	71.18	71.73	73.20	69.48
TiO_2	0.26	0.18	0.37	0.26	0.18	0.36
Al_2O_3	13.19	12.26	13.65	13.13	12.01	13.32
Fe_2O_3	2.57	1.09	3.35			
FeO				2.30	0.98	2.94
MnO	0.09	0.04	0.06			
MgO	0.47	0.46	0.45	0.47	0.45	0.44
CaO	1.61	0.25	1.54	0.40	0.17	0.49
Na_2O	2.68	3.25	3.50	2.67	3.18	3.42
K_2O	4.08	4.92	4.60	4.06	4.82	4.49
P_2O_5	0.07	0.06	0.08			
O_2					0.01	0.06
H_2O				5.00	5.00	5.00
Sum	97.10	97.21	98.77	100	100.00	100.00

(*) In the NCKFMASHTO chemical system

Supplementary Material#1 – Fsp and Qz microfabrics in the studied samples.

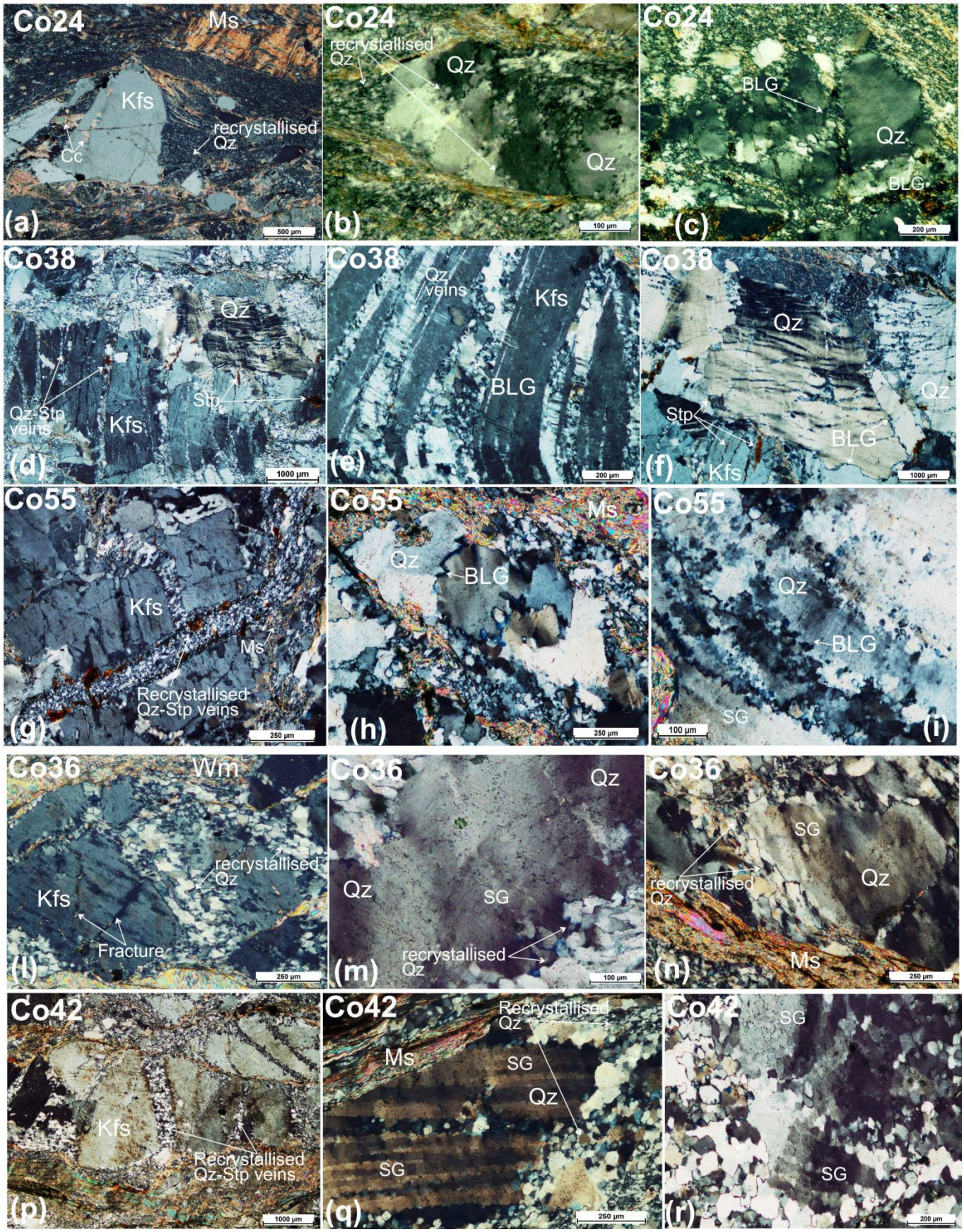

Sample CO24 (Crossed Polars)
(a) Fractured K-feldspar (K-Fsp) porphyroclast (igneous) in fine-grained recrystallized quartz (Qz) and white mica (Wm) shear matrix. Large Wm crystals are crenulated, and post-tectonic growth of calcite (Cc) is observed. (b) – (c) Patchy undulose extinction and dynamic recrystallisation in Qz, dominantly assisted by bulging recrystallisation (BLG).

Sample CO38 (Crossed Polars)
(d) Fractured and strained relic (igneous) K-feldspar-quartz assemblage in a fine-grained recrystallizes Qz-Wm matrix. Quartz-stilpnomelane (Stp) veins cut across the K-feldspar-Qz assemblage. (e) Enlargement showing the internal fabric of the Qz veins in K-Fsp. Qz grains show evidence of dynamic recrystallisation assisted by BLG. (f) Healed fractures in relict igneous Qz. Undulose extinction and BLG recrystallisation is observed.

Sample CO55 (Crossed Polars)
(g) Fractured (relic igneous) K-Fsp grains hosting recrystallized Qz veins. (h) – (i). Relic igneous Qz grains showing undulose extinction, deformation lamellae and evidence of dynamic recrystallisation assisted by BLG.

Sample CO36 (Crossed Polars)
(l) Fractured K-Fsp grains surrounded by fine-grained recrystallized Qz grains (early veins). Fracture in K-Fsp do not pass through the recrystallized Qz domains, indicating the differential rheological behavior during rock deformation. (m) Relic (igneous) Qz showing subgrain (SG) formation. (n) Bimodal grain size produced by subgrain rotation recrystallisation in Qz.

Sample CO42 (Crossed Polars)
(o) Fractured K-Fsp grains surrounded by fine-grained recrystallized Qz grains (early veins). (p) – (q) Bimodal grain size produced by subgrain rotation recrystallization in Qz.

Representative EMPA and chemical formulas of White Mica

Locality							
Sample							
Type							
Analysis	#1	#2	#3	#4	#5	#6	#7
SiO_2 (wt%)	50.77	51.06	50.49	50.71	50.37	49.71	50.59
TiO_2	0.44	0.48	0.39	0.36	0.47	0.37	0.34
Al_2O_3	25.18	25.52	25.08	25.28	25.08	24.45	25.21
FeOt	6.79	6.83	7.00	6.67	7.25	7.00	6.90
MnO	0.09	0.09	0.07	0.07	*bdl*	0.07	0.08
MgO	1.60	1.60	1.67	1.60	1.62	1.61	1.65
CaO	*bdl*	*bdl*	*bdl*	*bdl*	*bdl*	0.06	*bdl*
Na_2O	0.05	*bdl*	*bdl*	0.05	*bdl*	0.04	0.05
K_2O	10.55	10.79	10.66	10.32	11.04	10.84	10.82
BaO	0.11	0.14	0.09	0.09	0.12	0.08	0.13
Total	95.58	96.52	95.45	95.15	95.95	94.22	95.77
Formula (11 Oxygens)							
Si (apfu)	3.437	3.428	3.425	3.438	3.416	3.435	3.427
Ti	0.022	0.024	0.020	0.018	0.024	0.019	0.017
Al^{Tot}	2.009	2.019	2.005	2.020	2.005	1.991	2.013
$Al^{[IV]}$	0.563	0.572	0.575	0.562	0.584	0.565	0.573
$Al^{[VI]}$	1.446	1.447	1.430	1.458	1.421	1.426	1.440
Fe^{2+}	0.278	0.283	0.261	0.258	0.308	0.319	0.282
Fe^{3+}	0.107	0.101	0.136	0.120	0.104	0.086	0.109
Mn	0.005	0.005	0.004	0.004	-	0.004	0.005
Mg	0.162	0.161	0.169	0.162	0.164	0.166	0.167
Ca	-	-	-	-	-	-	-
Ba	0.003	0.004	0.003	0.002	0.003	0.002	0.003
Na	0.006	-	-	0.006	-	0.006	0.007
K	0.912	0.924	0.922	0.893	0.956	0.956	0.936
$^{(a)}$XPrl	0.08	0.07	0.07	0.10	0.03	0.03	0.05
$^{(a)}$XTri	0.02	0.02	0.02	0.02	0.02	0.02	0.02
$^{(a)}$XPg	0.01	-	-	0.01	-	0.01	0.01
$^{(a)}$XCel	0.46	0.45	0.44	0.46	0.44	0.45	0.44
$^{(a)}$XMs	0.44	0.46	0.47	0.43	0.51	0.49	0.48

* FeOt total iron reported as FeO; apfu: atoms per formula unit; bdl: below detection limit.

(a) White mica molar fractions: XPrl: Pyrophyllite, XTri: Trioctahedral substitution, XPg: Paragoı

#9	#10	#11	#12	#38	#39	#1	#2	#3
50.71	51.06	49.59	50.82	49.57	51.28	50.25	50.09	49.61
0.29	0.25	0.42	0.30	0.09	0.05	0.33	0.29	0.44
24.68	25.30	25.04	24.36	25.80	24.14	23.53	24.17	24.02
7.23	6.85	6.75	8.01	7.00	8.72	7.93	8.01	8.01
0.06	0.10	0.06	0.15	0.08	*bdl*	0.08	0.05	*bdl*
1.64	1.53	1.50	1.61	1.63	1.66	1.71	1.70	1.62
bdl	*bdl*	*bdl*	*bdl*	0.06	0.10	*bdl*	*bdl*	*bdl*
0.07	*bdl*	0.06	*bdl*	0.09	0.07	0.06	0.07	0.06
10.71	10.87	10.77	11.31	11.05	10.97	11.35	11.03	11.07
0.10	0.11	0.11	0.10	*bdl*	*bdl*	0.07	0.09	0.09
95.50	96.07	94.30	96.68	95.36	96.99	95.30	95.49	94.91
3.447	3.447	3.418	3.438	3.376	3.447	3.458	3.424	3.418
0.015	0.013	0.022	0.015	0.005	0.002	0.017	0.015	0.023
1.977	2.013	2.034	1.942	2.071	1.913	1.909	1.947	1.951
0.553	0.553	0.582	0.562	0.624	0.553	0.542	0.576	0.582
1.425	1.460	1.452	1.380	1.447	1.360	1.367	1.371	1.369
0.302	0.308	0.305	0.324	0.253	0.308	0.366	0.298	0.319
0.109	0.079	0.084	0.129	0.146	0.182	0.090	0.160	0.142
0.004	0.006	0.003	0.009	0.004	-	0.004	0.003	-
0.166	0.154	0.154	0.163	0.165	0.166	0.176	0.173	0.167
-	-	-	-	0.004	0.007	-	-	-
0.003	0.003	0.003	0.003	-	-	0.002	0.002	0.002
0.010	-	0.009	-	0.012	0.009	0.009	0.009	0.007
0.928	0.936	0.947	0.976	0.961	0.941	0.997	0.962	0.973
0.06	0.06	0.04	0.02	0.02	0.04	-	0.03	0.02
0.02	0.02	0.02	0.02	0.02	0.02	0.02	0.02	0.02
0.01	-	0.01	-	0.01	0.01	0.01	0.01	0.01
0.46	0.46	0.44	0.45	0.38	0.45	0.48	0.44	0.44
0.46	0.47	0.50	0.51	0.57	0.48	0.50	0.51	0.52

nite, XCel: Celadonite; XMs: Muscovite. Trioctahedral substitution is fixed by stochiometry at XTri=0.02.

		CO-24						
		Wm1						
#4	#5	#6	#8	#9	#10	#11	#13	#15
50.24	49.26	49.40	49.02	50.03	50.32	50.59	48.27	48.88
0.41	0.53	0.57	0.96	0.35	0.47	0.34	0.50	0.47
22.69	25.39	25.14	25.67	23.43	21.57	21.69	27.67	27.63
8.54	7.12	6.93	6.66	8.25	9.70	9.23	4.58	4.79
0.08	*bdl*	0.06	0.09	0.09	0.08	0.16	*bdl*	*bdl*
1.69	1.51	1.57	1.44	1.61	2.03	2.01	1.24	1.20
bdl	*bdl*	*bdl*	0.11	*bdl*	*bdl*	*bdl*	0.18	0.22
0.11	0.06	0.12	0.04	0.05	0.09	0.11	0.45	0.35
11.18	11.35	11.13	11.00	11.12	11.15	11.27	10.24	9.64
bdl	0.13	0.14	0.10	0.07	*bdl*	*bdl*	0.07	*bdl*
94.94	95.35	95.07	95.08	95.00	95.40	95.40	93.21	93.17
3.476	3.377	3.393	3.362	3.450	3.470	3.490	3.343	3.360
0.021	0.027	0.029	0.050	0.018	0.024	0.018	0.026	0.024
1.850	2.051	2.035	2.075	1.905	1.753	1.763	2.258	2.239
0.524	0.623	0.607	0.638	0.550	0.530	0.510	0.657	0.640
1.326	1.429	1.428	1.436	1.355	1.223	1.254	1.600	1.598
0.385	0.321	0.319	0.309	0.345	0.338	0.360	0.265	0.247
0.108	0.087	0.079	0.073	0.130	0.221	0.173	-	0.028
0.005	-	0.004	0.005	0.005	0.005	0.009	-	-
0.174	0.155	0.161	0.147	0.166	0.209	0.207	0.128	0.123
-	-	-	0.008	-	-	-	0.013	0.016
-	0.003	0.004	0.003	0.002	-	-	0.002	-
0.015	0.009	0.015	0.006	0.007	0.012	0.015	0.060	0.046
0.987	0.993	0.976	0.963	0.978	0.980	0.992	0.905	0.845
-	-	0.00	0.02	0.01	0.01	-	0.02	0.09
0.02	0.02	0.02	0.02	0.02	0.02	0.02	0.02	0.02
0.02	0.01	0.02	0.01	0.01	0.01	0.02	0.06	0.05
0.50	0.40	0.42	0.41	0.47	0.49	0.51	0.37	0.38
0.48	0.57	0.54	0.54	0.50	0.48	0.47	0.52	0.45

#17	#18	#19	#20	#21	#22	#23	#24	#25
50.32	48.89	48.87	50.10	50.05	49.51	49.62	49.29	49.70
0.29	0.67	0.21	0.28	0.19	0.17	0.14	0.15	0.19
22.07	25.91	25.00	24.83	25.33	24.51	25.03	25.11	24.31
8.94	5.76	6.85	6.59	6.93	7.60	7.46	7.01	7.90
0.07	0.09	*bdl*	0.08	*bdl*	0.07	0.08	*bdl*	0.13
1.97	1.56	1.69	1.56	1.61	1.65	1.57	1.57	1.59
bdl	0.07	*bdl*	0.04	*bdl*	*bdl*	0.07	*bdl*	*bdl*
0.09	0.27	0.08	0.84	0.39	0.10	*bdl*	0.09	0.17
11.21	10.78	11.19	10.40	11.01	11.00	11.09	11.48	10.95
bdl	0.11	0.13	0.07	0.10	0.11	0.10	0.08	0.11
94.94	94.10	94.02	94.79	95.60	94.71	95.16	94.76	95.03
3.482	3.378	3.392	3.448	3.415	3.410	3.400	3.403	3.416
0.015	0.035	0.011	0.014	0.010	0.009	0.007	0.008	0.010
1.800	2.109	2.045	2.014	2.037	1.990	2.021	2.043	1.969
0.518	0.622	0.608	0.552	0.585	0.590	0.600	0.597	0.584
1.281	1.487	1.437	1.462	1.451	1.400	1.421	1.445	1.386
0.352	0.309	0.302	0.380	0.337	0.292	0.291	0.339	0.306
0.165	0.024	0.095	-	0.059	0.146	0.136	0.065	0.148
0.004	0.005	-	0.005	-	0.004	0.005	-	0.007
0.203	0.160	0.175	0.160	0.163	0.169	0.160	0.162	0.163
-	0.005	-	0.003	-	-	0.005	-	-
-	0.003	0.004	0.002	0.003	0.003	0.003	0.002	0.003
0.012	0.036	0.011	0.112	0.052	0.013	-	0.011	0.022
0.990	0.950	0.991	0.913	0.958	0.967	0.970	1.011	0.960
-	0.01	-	-	-	0.02	0.02	-	0.01
0.02	0.02	0.02	0.02	0.02	0.02	0.02	0.02	0.02
0.01	0.04	0.01	0.11	0.05	0.01	-	0.01	0.02
0.50	0.41	0.40	0.46	0.42	0.42	0.41	0.41	0.43
0.48	0.53	0.57	0.41	0.51	0.54	0.55	0.56	0.52

								Transect-
#26	#27	#2	#4	#5	#9	#11	#15	#16
48.75	49.67	50.56	49.66	49.85	49.70	49.84	49.61	49.42
0.46	0.41	0.07	0.10	0.08	0.09	0.08	0.12	0.06
24.51	24.31	22.88	24.51	24.53	24.47	22.31	23.38	23.58
7.30	7.33	7.44	7.00	6.91	6.91	7.86	7.52	7.49
0.07	0.11	0.10	0.04	0.07	0.07	0.08	0.10	0.11
1.47	1.55	2.77	2.38	2.48	2.46	2.59	2.65	2.39
0.09	0.06	0.09	*bdl*	*bdl*	0.04	*bdl*	0.05	0.08
0.39	0.24	0.21	0.08	0.07	0.10	0.07	*bdl*	0.06
10.63	10.87	10.86	11.50	11.37	11.24	11.14	11.41	11.20
0.10	0.08	0.06	0.20	0.14	0.14	0.08	0.10	0.04
93.76	94.62	95.03	95.47	95.50	95.22	94.05	94.94	94.42
3.399	3.431	3.458	3.395	3.396	3.395	3.461	3.410	3.412
0.024	0.021	0.004	0.005	0.004	0.004	0.004	0.006	0.003
2.015	1.979	1.844	1.975	1.970	1.971	1.825	1.894	1.919
0.601	0.569	0.542	0.605	0.604	0.605	0.539	0.590	0.588
1.414	1.410	1.303	1.370	1.366	1.366	1.286	1.304	1.332
0.344	0.349	0.226	0.244	0.214	0.211	0.257	0.216	0.230
0.081	0.075	0.200	0.156	0.180	0.184	0.199	0.217	0.202
0.004	0.006	0.006	0.003	0.004	0.004	0.005	0.006	0.006
0.152	0.160	0.282	0.242	0.252	0.251	0.268	0.272	0.246
0.006	0.004	0.007	-	-	0.003	-	0.004	0.006
0.003	0.002	0.002	0.005	0.004	0.004	0.002	0.003	0.001
0.053	0.032	0.028	0.011	0.009	0.013	0.009	-	0.007
0.945	0.958	0.947	1.003	0.988	0.980	0.987	1.001	0.986
-	0.00	0.02	-	-	0.00	-	-	-
0.02	0.02	0.02	0.02	0.02	0.02	0.02	0.02	0.02
0.05	0.03	0.03	0.01	0.01	0.01	0.01	-	0.01
0.42	0.45	0.46	0.40	0.40	0.40	0.46	0.42	0.42
0.50	0.50	0.47	0.57	0.57	0.57	0.51	0.56	0.56

-1 (Castirla)								
							CO-25	
							Wm2	
#18	#19	#21	#25	#27	#30	#33	#35	#36
50.77	49.78	49.93	49.56	49.48	49.56	50.07	51.49	49.75
0.08	0.06	0.09	0.08	0.09	0.08	0.13	*bdl*	0.06
24.58	24.43	24.19	24.29	23.82	24.25	24.48	22.48	24.61
6.22	6.71	6.95	7.08	7.12	6.64	6.52	6.73	6.71
0.10	*bdl*	0.10	0.14	0.14	0.08	*bdl*	0.07	0.08
2.67	2.41	2.46	2.26	2.33	2.27	2.53	3.11	2.36
bdl	*bdl*	*bdl*	0.11	*bdl*	*bdl*	0.13	*bdl*	*bdl*
0.06	*bdl*	0.07	0.13	*bdl*	0.37	0.10	*bdl*	*bdl*
11.27	11.54	11.45	11.04	11.67	11.18	10.93	11.36	11.59
bdl	0.14	0.09	0.16	0.12	0.15	0.07	*bdl*	0.10
95.75	95.07	95.34	94.85	94.77	94.58	94.96	95.25	95.26
3.432	3.412	3.413	3.403	3.417	3.421	3.415	3.509	3.403
0.004	0.003	0.005	0.004	0.005	0.004	0.007	-	0.003
1.958	1.973	1.949	1.966	1.939	1.973	1.967	1.806	1.984
0.568	0.588	0.587	0.597	0.583	0.579	0.585	0.491	0.597
1.390	1.385	1.361	1.370	1.356	1.394	1.382	1.315	1.387
0.204	0.250	0.234	0.237	0.273	0.294	0.209	0.245	0.242
0.148	0.134	0.163	0.169	0.138	0.090	0.163	0.138	0.142
0.006	-	0.006	0.008	0.008	0.005	-	0.004	0.005
0.269	0.246	0.251	0.231	0.240	0.234	0.258	0.316	0.241
-	-	-	0.008	-	-	0.009	-	-
-	0.004	0.003	0.004	0.003	0.004	0.002	-	0.003
0.008	-	0.010	0.017	-	0.049	0.013	-	-
0.972	1.009	0.999	0.967	1.028	0.984	0.951	0.987	1.012
0.02	-	-	0.00	-	-	0.02	0.01	-
0.02	0.02	0.02	0.02	0.02	0.02	0.02	0.02	0.02
0.01	-	0.01	0.02	-	0.05	0.01	-	-
0.44	0.42	0.42	0.41	0.42	0.43	0.42	0.51	0.41
0.53	0.57	0.56	0.55	0.56	0.51	0.52	0.47	0.58

#37	#38	#39	#40	#41	#43	#44	#45	#46
48.58	49.20	48.34	49.33	48.74	49.17	48.55	49.09	49.38
0.07	0.11	0.07	0.07	*bdl*	0.07	0.05	0.06	0.07
24.97	25.23	24.68	24.48	24.82	24.60	24.47	24.30	24.26
7.07	7.06	6.47	6.76	6.44	6.75	6.47	6.67	6.71
0.08	0.05	0.11	0.15	0.10	0.11	0.11	0.09	0.05
2.45	2.49	2.32	2.34	2.23	2.25	2.34	2.36	2.31
bdl	*bdl*	*bdl*	*bdl*	*bdl*	*bdl*	*bdl*	*bdl*	*bdl*
bdl	0.05	0.05	0.11	0.07	0.07	0.08	0.07	0.08
11.55	11.36	11.56	11.49	11.46	11.41	11.54	11.32	11.33
0.20	0.16	0.16	0.18	0.16	0.18	0.19	0.15	0.20
94.97	95.69	93.76	94.91	94.02	94.62	93.81	94.12	94.39
3.335	3.340	3.367	3.394	3.379	3.390	3.382	3.399	3.413
0.003	0.005	0.004	0.003	-	0.003	0.003	0.003	0.003
2.020	2.019	2.026	1.985	2.028	1.999	2.009	1.982	1.976
0.665	0.660	0.633	0.606	0.621	0.610	0.618	0.601	0.587
1.355	1.359	1.392	1.379	1.408	1.389	1.390	1.381	1.389
0.172	0.149	0.227	0.243	0.236	0.238	0.245	0.232	0.257
0.234	0.252	0.149	0.146	0.137	0.151	0.132	0.154	0.130
0.005	0.003	0.007	0.009	0.006	0.007	0.007	0.005	0.003
0.251	0.252	0.240	0.240	0.231	0.232	0.243	0.244	0.237
-	-	-	-	-	-	-	-	-
0.005	0.004	0.004	0.005	0.004	0.005	0.005	0.004	0.005
-	0.006	0.007	0.015	0.009	0.009	0.011	0.009	0.011
1.011	0.984	1.028	1.009	1.014	1.004	1.025	1.000	0.999
-	0.01	-	-	-	-	-	-	-
0.02	0.02	0.02	0.02	0.02	0.02	0.02	0.02	0.02
-	0.01	0.01	0.01	0.01	0.01	0.01	0.01	0.01
0.34	0.35	0.37	0.40	0.38	0.39	0.38	0.40	0.42
0.64	0.63	0.61	0.57	0.60	0.58	0.59	0.57	0.56

							Wm1	
#47	#48	#49	#1	#2	#8	#9	#11	#12
49.02	49.23	49.39	50.69	49.67	49.01	49.40	48.61	48.73
0.06	0.05	*bdl*	0.07	0.11	0.23	0.09	0.10	0.11
24.25	24.49	24.46	22.68	24.58	24.23	25.85	25.43	25.87
6.43	6.45	6.40	6.76	6.89	5.56	4.62	5.41	5.11
0.17	0.14	0.09	0.09	0.13	*bdl*	*bdl*	*bdl*	*bdl*
2.39	2.54	2.47	2.87	2.34	4.34	3.83	4.35	4.16
bdl	*bdl*	*bdl*	*bdl*	*bdl*	0.04	0.06	0.05	0.13
0.07	*bdl*	0.08	0.07	*bdl*	0.05	0.10	0.08	0.06
11.42	11.58	11.48	11.27	11.54	10.97	9.66	9.59	9.70
0.18	0.15	0.16	0.06	0.16	*bdl*	*bdl*	*bdl*	*bdl*
93.98	94.63	94.52	94.55	95.42	94.42	93.61	93.62	93.87
3.403	3.390	3.404	3.488	3.394	3.320	3.322	3.263	3.268
0.003	0.003	-	0.003	0.005	0.012	0.005	0.005	0.005
1.984	1.988	1.987	1.840	1.980	1.934	2.049	2.012	2.045
0.597	0.610	0.596	0.512	0.606	0.680	0.678	0.737	0.732
1.387	1.377	1.391	1.328	1.374	1.254	1.372	1.276	1.313
0.239	0.214	0.239	0.259	0.237	-	-	-	-
0.134	0.157	0.130	0.130	0.157	0.315	0.260	0.304	0.287
0.010	0.008	0.005	0.005	0.008	-	-	-	-
0.247	0.261	0.253	0.294	0.239	0.438	0.384	0.435	0.415
-	-	-	-	-	0.003	0.005	0.003	0.010
0.005	0.004	0.004	0.002	0.004	-	-	-	-
0.009	-	0.011	0.009	-	0.007	0.013	0.010	0.008
1.012	1.017	1.009	0.989	1.006	0.948	0.829	0.821	0.830
-	-	-	-	-	0.04	0.15	0.17	0.15
0.02	0.02	0.02	0.02	0.02	0.02	0.02	0.02	0.02
0.01	-	0.01	0.01	-	0.01	0.01	0.01	0.01
0.41	0.39	0.41	0.49	0.40	0.33	0.33	0.27	0.27
0.57	0.59	0.57	0.48	0.58	0.61	0.49	0.54	0.54

		CO-38						
								Wr
#31	#34	#3	#4	#5	#7	#14	#35	#38
48.37	48.40	50.16	48.89	49.70	50.09	49.72	49.78	49.15
0.17	0.41	0.23	0.24	0.28	0.23	0.13	0.41	0.13
22.11	22.27	22.97	22.22	22.67	24.07	24.80	22.66	22.98
10.67	10.12	5.72	6.51	6.17	5.03	4.89	7.63	9.18
0.14	0.14	0.06	*bdl*	*bdl*	*bdl*	*bdl*	0.14	0.11
2.68	2.78	4.73	4.74	4.80	4.36	4.09	2.94	2.63
0.16	0.22	0.05	*bdl*	*bdl*	0.09	*bdl*	0.28	*bdl*
bdl	0.08	*bdl*	*bdl*	*bdl*	0.04	0.06	0.05	*bdl*
10.93	10.99	11.02	10.46	10.65	10.46	10.24	10.98	11.19
bdl	*bdl*	*bdl*	*bdl*	*bdl*	*bdl*	*bdl*	*bdl*	*bdl*
95.22	95.39	94.94	93.06	94.28	94.36	93.93	94.87	95.37
3.325	3.323	3.382	3.353	3.363	3.376	3.354	3.418	3.361
0.009	0.021	0.012	0.012	0.014	0.011	0.007	0.021	0.006
1.791	1.802	1.825	1.796	1.808	1.912	1.972	1.834	1.853
0.675	0.677	0.618	0.647	0.637	0.624	0.646	0.582	0.639
1.116	1.126	1.207	1.149	1.172	1.287	1.326	1.252	1.214
0.099	0.117	-	-	-	-	-	0.201	0.137
0.514	0.464	0.322	0.373	0.349	0.284	0.276	0.237	0.389
0.008	0.008	0.004	-	-	-	-	0.008	0.006
0.274	0.284	0.475	0.485	0.484	0.438	0.412	0.301	0.268
0.012	0.016	0.003	-	-	0.007	-	0.021	0.002
-	-	-	-	-	-	-	-	-
-	0.010	-	-	-	0.005	0.007	-	0.003
0.959	0.963	0.948	0.915	0.920	0.899	0.881	0.962	0.977
0.02	0.01	0.05	0.08	0.08	0.09	0.11	0.01	0.02
0.02	0.02	0.02	0.02	0.02	0.02	0.02	0.02	0.02
-	0.01	-	-	-	0.01	0.01	-	0.00
0.33	0.34	0.39	0.37	0.38	0.39	0.36	0.44	0.37
0.61	0.61	0.54	0.54	0.53	0.50	0.51	0.51	0.60

m2								
#40	#44	#45	#3	#4	#8	#11	#80	#81
48.92	49.92	50.17	51.43	50.51	51.39	51.44	46.43	47.08
0.29	*bdl*	*bdl*	*bdl*	*bdl*	*bdl*	0.06	0.27	0.12
22.49	22.16	22.29	22.43	22.78	22.90	21.48	33.26	27.61
9.02	8.57	8.37	7.97	6.62	6.91	8.90	2.20	5.51
0.15	0.19	0.15	0.30	0.19	0.34	0.22	0.06	0.11
2.61	2.37	2.37	2.69	2.64	2.78	2.71	1.03	2.49
0.18	*bdl*	*bdl*	*bdl*	*bdl*	0.04	*bdl*	*bdl*	*bdl*
0.05	0.05	*bdl*	*bdl*	*bdl*	*bdl*	*bdl*	0.18	0.16
10.87	11.22	11.46	11.37	11.15	10.98	10.29	11.11	10.77
bdl	*bdl*	*bdl*	*bdl*	*bdl*	*bdl*	*bdl*	0.23	0.13
94.59	94.48	94.82	96.19	93.89	95.34	95.10	94.76	93.98
3.376	3.458	3.467	3.486	3.495	3.491	3.500	3.132	3.216
0.015	-	-	-	-	-	0.003	0.014	0.006
1.830	1.809	1.816	1.792	1.858	1.834	1.722	2.644	2.223
0.624	0.542	0.533	0.514	0.505	0.509	0.500	0.868	0.784
1.206	1.267	1.283	1.279	1.353	1.325	1.223	1.775	1.439
0.165	0.263	0.286	0.242	0.259	0.213	0.169	0.095	-
0.355	0.234	0.198	0.210	0.124	0.179	0.337	0.029	0.315
0.009	0.011	0.009	0.017	0.011	0.020	0.013	0.003	0.006
0.269	0.244	0.244	0.271	0.272	0.281	0.275	0.103	0.253
0.013	-	-	-	-	0.003	-	-	-
-	-	-	-	-	-	-	0.006	0.004
0.007	0.007	-	-	-	-	-	0.023	0.021
0.957	0.991	1.010	0.983	0.985	0.951	0.893	0.956	0.939
0.02	0.00	0.00	0.02	0.01	0.04	0.11	0.01	0.04
0.02	0.02	0.02	0.02	0.02	0.02	0.02	0.02	0.02
0.01	0.01	-	-	-	-	-	0.02	0.02
0.39	0.46	0.47	0.49	0.50	0.49	0.50	0.15	0.22
0.56	0.52	0.52	0.49	0.48	0.45	0.38	0.80	0.70

		Wm1						
#82	#83	#87	#88	#95	#84	#50	#51	#52
45.73	45.27	46.64	45.07	45.60	48.73	49.79	49.77	49.66
0.44	0.04	*bdl*	0.06	*bdl*	*bdl*	*bdl*	*bdl*	0.06
28.34	35.82	32.74	34.69	35.32	28.82	21.29	21.29	20.49
5.74	1.43	2.91	1.93	1.27	3.57	7.84	7.52	7.63
0.15	*bdl*	0.17	0.12	0.36	*bdl*	0.19	0.17	0.09
2.63	0.35	0.92	0.31	0.29	2.32	3.85	3.97	4.04
bdl	*bdl*	*bdl*	*bdl*	*bdl*	*bdl*	*bdl*	*bdl*	*bdl*
0.18	0.23	0.12	0.20	0.12	0.12	*bdl*	0.06	*bdl*
11.10	11.09	11.32	11.16	11.31	11.44	11.34	11.01	11.49
0.27	0.07	0.20	0.08	0.28	0.07	*bdl*	*bdl*	*bdl*
94.60	94.31	95.02	93.62	94.54	95.06	94.30	93.79	93.47
3.117	3.054	3.148	3.077	3.083	3.290	3.431	3.435	3.462
0.023	0.002	-	0.003	-	-	-	-	0.003
2.277	2.848	2.604	2.791	2.815	2.293	1.729	1.732	1.684
0.883	0.946	0.852	0.923	0.917	0.710	0.569	0.565	0.538
1.393	1.902	1.752	1.868	1.898	1.583	1.160	1.166	1.146
-	0.069	0.112	0.109	0.072	0.120	0.089	0.060	0.130
0.327	0.012	0.052	0.001	-	0.082	0.363	0.375	0.315
0.009	-	0.010	0.007	0.021	0.002	0.011	0.010	0.005
0.267	0.036	0.092	0.031	0.029	0.234	0.395	0.408	0.420
-	-	-	-	-	-	-	-	-
0.007	0.002	0.005	0.002	0.007	0.002	-	-	-
0.024	0.030	0.016	0.026	0.015	0.016	-	0.008	-
0.965	0.955	0.975	0.972	0.975	0.985	0.997	0.969	1.022
-	0.01	-	-	-	-	-	0.02	-
0.02	0.02	0.02	0.02	0.02	0.02	0.02	0.02	0.02
0.02	0.03	0.02	0.03	0.02	0.02	-	0.01	-
0.14	0.06	0.15	0.08	0.08	0.29	0.43	0.44	0.47
0.82	0.89	0.81	0.88	0.88	0.68	0.55	0.52	0.52

		CO-35						
						Wm2		
#53	#54	#55	#66	#68	#69	#70	#85	#86
50.37	50.41	50.45	51.16	49.04	49.95	51.11	49.90	51.53
bdl	*bdl*	*bdl*	*bdl*	0.14	0.05	*bdl*	*bdl*	*bdl*
20.93	21.43	21.33	20.74	20.46	21.35	20.02	20.78	21.25
7.64	6.58	7.05	7.07	7.84	6.82	7.61	7.64	6.98
0.10	0.13	0.10	0.20	0.18	0.16	0.07	0.11	0.14
4.00	3.74	4.12	4.05	4.42	3.86	4.17	4.13	4.02
bdl	*bdl*	*bdl*	*bdl*	0.09	*bdl*	*bdl*	*bdl*	*bdl*
0.10	0.12	0.04	*bdl*	0.05	*bdl*	*bdl*	0.06	*bdl*
11.51	10.95	11.26	11.30	11.26	11.24	11.30	11.53	11.42
bdl	0.07	*bdl*	0.06	*bdl*	0.04	*bdl*	*bdl*	*bdl*
94.64	93.43	94.36	94.57	93.49	93.48	94.29	94.15	95.34
3.466	3.494	3.462	3.510	3.410	3.467	3.522	3.451	3.504
-	-	-	-	0.007	0.003	-	-	-
1.698	1.750	1.725	1.677	1.677	1.746	1.626	1.694	1.703
0.534	0.506	0.538	0.490	0.590	0.533	0.478	0.549	0.496
1.164	1.244	1.187	1.187	1.087	1.213	1.148	1.145	1.207
0.142	0.154	0.091	0.143	0.028	0.126	0.149	0.105	0.144
0.297	0.227	0.313	0.263	0.428	0.270	0.290	0.337	0.253
0.006	0.008	0.006	0.011	0.011	0.010	0.004	0.007	0.008
0.410	0.386	0.421	0.414	0.459	0.399	0.429	0.426	0.408
-	-	-	-	0.007	0.003	-	-	-
-	0.002	-	0.002	-	0.001	-	-	-
0.013	0.015	0.006	-	0.007	-	-	0.008	-
1.010	0.968	0.986	0.989	0.999	0.996	0.994	1.017	0.990
-	0.01	0.01	-	-	-	-	-	0.01
0.02	0.02	0.02	0.02	0.02	0.02	0.02	0.02	0.02
0.01	0.02	0.01	-	0.01	-	-	0.01	-
0.47	0.49	0.46	0.51	0.42	0.47	0.52	0.45	0.50
0.51	0.46	0.51	0.47	0.56	0.51	0.46	0.53	0.48

#91	#92	#93	#96	#100	#101	#102	#7	#10
50.24	49.79	50.62	49.80	50.41	50.32	50.62	45.57	45.18
bdl	*bdl*	*bdl*	*bdl*	0.11	0.04	*bdl*	0.18	0.20
21.30	21.97	21.53	20.34	19.94	20.69	16.99	36.13	36.38
7.33	7.21	6.98	8.12	7.92	7.40	10.88	2.21	1.86
0.08	0.13	0.12	0.14	0.20	0.19	0.20	0.08	0.08
4.07	3.66	3.78	4.17	4.50	4.17	3.34	0.21	0.17
bdl	0.09	*bdl*	*bdl*	0.04	*bdl*	*bdl*	*bdl*	*bdl*
0.07	*bdl*	*bdl*	0.06	*bdl*	*bdl*	*bdl*	0.59	0.51
11.43	11.19	11.39	11.39	11.28	11.61	11.35	11.18	11.12
bdl	*bdl*	*bdl*	*bdl*	*bdl*	*bdl*	*bdl*	*bdl*	*bdl*
94.53	94.04	94.42	94.02	94.39	94.42	93.37	96.14	95.50
3.452	3.434	3.480	3.449	3.469	3.470	3.590	3.031	3.019
-	-	-	-	0.006	0.002	-	0.009	0.010
1.725	1.786	1.744	1.660	1.617	1.681	1.420	2.832	2.865
0.548	0.566	0.520	0.551	0.531	0.530	0.410	0.969	0.981
1.177	1.220	1.224	1.110	1.086	1.151	1.010	1.863	1.885
0.103	0.113	0.150	0.084	0.063	0.119	0.314	0.099	0.083
0.318	0.303	0.252	0.386	0.393	0.308	0.331	0.024	0.021
0.005	0.007	0.007	0.008	0.011	0.011	0.012	0.005	0.004
0.417	0.376	0.387	0.431	0.461	0.429	0.353	0.021	0.017
-	0.007	-	-	0.003	-	-	-	-
-	-	-	-	-	-	-	-	-
0.010	-	-	0.008	-	-	-	0.075	0.066
1.002	0.985	0.999	1.006	0.990	1.022	1.027	0.949	0.948
-	0.01	-	-	-	-	-	-	-
0.02	0.02	0.02	0.02	0.02	0.02	0.02	0.02	0.02
0.01	-	-	0.01	-	-	-	0.07	0.07
0.45	0.43	0.48	0.45	0.47	0.47	0.59	0.04	0.03
0.53	0.54	0.51	0.53	0.51	0.52	0.40	0.88	0.90

Transect2 (Vivario-Venaco)								
			Wm1					
#12	#23	#6	#7	#8	#10	#11	#1	#2
45.51	48.10	44.24	44.89	46.29	45.25	46.17	49.08	48.31
0.44	0.22	0.26	0.24	0.13	0.22	0.19	*bdl*	0.05
34.42	33.55	31.07	30.25	30.85	30.43	30.28	24.38	25.01
3.72	1.99	4.30	4.47	3.71	4.32	4.35	6.73	6.77
0.13	*bdl*	0.21	0.16	0.20	0.17	0.12	0.18	0.14
0.30	1.27	1.31	1.47	1.41	1.40	1.41	3.61	3.36
0.10	*bdl*	*bdl*	*bdl*	*bdl*	*bdl*	*bdl*	*bdl*	*bdl*
0.46	0.90	0.31	0.36	0.43	0.44	0.43	0.05	0.05
11.08	9.69	10.38	10.51	10.68	10.48	10.37	11.34	11.53
bdl	0.13	0.07	0.05	*bdl*	*bdl*	0.05	*bdl*	0.04
96.15	95.85	92.14	92.39	93.70	92.70	93.37	95.36	95.26
3.042	3.169	3.069	3.114	3.162	3.127	3.164	3.320	3.282
0.022	0.011	0.013	0.013	0.007	0.011	0.010	-	0.003
2.712	2.605	2.540	2.473	2.484	2.478	2.446	1.944	2.003
0.958	0.831	0.931	0.886	0.838	0.873	0.836	0.680	0.718
1.753	1.775	1.609	1.587	1.646	1.606	1.610	1.264	1.285
0.105	0.056	-	0.006	0.063	0.032	0.052	-	0.005
0.103	0.054	0.250	0.254	0.149	0.218	0.198	0.381	0.380
0.007	-	0.012	0.009	0.012	0.010	0.007	0.010	0.008
0.029	0.124	0.135	0.152	0.144	0.144	0.144	0.364	0.340
0.007	-	-	-	-	-	-	-	-
-	0.003	0.002	0.001	-	-	0.001	-	0.001
0.060	0.115	0.041	0.048	0.057	0.058	0.057	0.007	0.007
0.944	0.815	0.919	0.930	0.931	0.924	0.907	0.979	0.999
0.00	0.07	0.04	0.02	0.01	0.02	0.03	0.01	-
0.02	0.02	0.02	0.02	0.02	0.02	0.02	0.02	0.02
0.06	0.12	0.04	0.05	0.06	0.06	0.06	0.01	0.01
0.06	0.18	0.08	0.13	0.17	0.14	0.17	0.32	0.28
0.86	0.62	0.82	0.79	0.75	0.77	0.72	0.65	0.70

							CO-36	
#4	#5	#6	#8	#9	#11	#13	#17	#18
49.91	49.64	51.21	51.71	49.23	50.52	49.04	51.76	50.99
bdl	0.05	*bdl*	*bdl*	0.08	*bdl*	0.06	0.10	0.09
23.92	24.85	23.62	24.16	23.66	24.44	23.45	23.62	23.77
5.64	5.70	6.32	4.69	7.20	5.11	7.52	5.35	5.55
0.11	0.09	0.12	0.15	0.13	0.12	0.14	0.17	0.11
3.24	3.31	3.23	3.10	3.13	3.19	3.29	3.02	3.04
bdl	*bdl*	*bdl*	*bdl*	0.06	*bdl*	0.08	*bdl*	0.36
bdl	*bdl*	*bdl*	0.04	0.05	*bdl*	*bdl*	0.05	*bdl*
11.57	11.55	11.51	12.00	11.23	11.71	11.24	11.94	11.51
bdl	0.05	*bdl*	0.08	0.06	0.07	*bdl*	0.05	0.08
94.38	95.24	96.01	95.92	94.83	95.16	94.81	96.06	95.49
3.424	3.367	3.454	3.503	3.369	3.438	3.353	3.509	3.475
-	0.003	-	-	0.004	-	0.003	0.005	0.005
1.934	1.987	1.877	1.929	1.908	1.960	1.890	1.887	1.909
0.576	0.633	0.546	0.497	0.631	0.562	0.647	0.491	0.525
1.358	1.354	1.331	1.432	1.277	1.398	1.244	1.396	1.384
0.168	0.096	0.177	0.266	0.105	0.189	0.069	0.303	0.283
0.155	0.227	0.179	-	0.307	0.102	0.361	0.001	0.033
0.006	0.005	0.007	0.008	0.008	0.007	0.008	0.010	0.006
0.331	0.335	0.324	0.313	0.319	0.324	0.335	0.305	0.309
-	-	-	-	0.004	-	0.006	-	0.026
-	0.001	-	0.002	0.002	0.002	-	0.001	0.002
-	-	-	0.005	0.007	-	-	0.007	-
1.013	1.000	0.990	1.037	0.980	1.017	0.981	1.033	1.001
-	-	0.01	-	0.01	-	0.01	-	-
0.02	0.02	0.02	0.02	0.02	0.02	0.02	0.02	0.02
-	-	-	0.01	0.01	-	-	0.01	-
0.43	0.37	0.45	0.50	0.37	0.44	0.36	0.51	0.48
0.56	0.62	0.53	0.48	0.60	0.55	0.61	0.47	0.48

				Wm2				
#19	#24	#25	#3	#4	#12	#13	#14	#15
51.49	51.19	51.24	50.71	51.03	50.49	51.70	49.71	51.33
0.08	0.18	0.06	0.04	*bdl*	0.05	*bdl*	0.06	*bdl*
23.55	23.60	24.22	24.10	23.58	24.38	23.90	25.35	23.58
5.45	6.05	5.44	5.48	5.20	5.35	4.66	5.56	5.03
0.11	0.10	0.08	0.18	0.18	0.12	0.10	*bdl*	0.12
3.32	3.10	3.10	3.24	3.13	3.16	3.19	2.96	3.25
bdl	*bdl*	*bdl*	*bdl*	*bdl*	*bdl*	*bdl*	0.05	*bdl*
bdl	0.05	0.07	*bdl*	0.09	0.05	*bdl*	0.11	0.06
11.48	10.97	11.67	11.34	11.17	11.50	11.44	11.11	11.33
0.08	0.07	0.10	0.06	0.06	0.06	0.06	0.09	0.09
95.56	95.30	95.96	95.15	94.42	95.16	95.04	94.99	94.79
3.486	3.466	3.464	3.441	3.491	3.433	3.512	3.373	3.500
0.004	0.009	0.003	0.002	-	0.002	-	0.003	-
1.879	1.883	1.929	1.927	1.901	1.954	1.913	2.027	1.895
0.514	0.534	0.536	0.559	0.509	0.567	0.488	0.627	0.500
1.366	1.350	1.393	1.369	1.392	1.387	1.426	1.400	1.394
0.206	0.177	0.232	0.155	0.214	0.176	0.244	0.122	0.224
0.103	0.165	0.076	0.156	0.084	0.128	0.021	0.194	0.063
0.006	0.006	0.005	0.011	0.010	0.007	0.006	-	0.007
0.336	0.313	0.312	0.328	0.319	0.320	0.323	0.299	0.330
-	-	-	-	-	-	-	0.003	-
0.002	0.002	0.003	0.002	0.002	0.002	0.002	0.002	0.002
-	0.006	0.009	-	0.012	0.007	-	0.014	0.008
0.991	0.948	1.006	0.982	0.975	0.997	0.992	0.961	0.985
0.01	0.04	-	0.01	0.01	-	0.00	0.02	0.00
0.02	0.02	0.02	0.02	0.02	0.02	0.02	0.02	0.02
-	0.01	0.01	-	0.01	0.01	-	0.01	0.01
0.49	0.48	0.47	0.44	0.49	0.44	0.51	0.38	0.50
0.49	0.46	0.51	0.53	0.47	0.55	0.47	0.58	0.47

#16	#17	#18	#19	#20	#21	#22	#30	#15
50.37	50.78	50.58	50.32	51.92	51.26	53.72	52.33	52.68
0.06	*bdl*	*bdl*	*bdl*	0.04	0.04	0.10	0.08	0.06
23.08	23.98	24.00	23.97	23.65	23.63	22.80	23.52	22.38
5.61	5.33	5.57	6.15	4.94	5.62	6.10	5.58	6.41
0.11	0.08	0.13	0.12	0.11	0.09	0.20	0.15	0.15
3.34	3.30	3.52	3.45	3.13	3.42	2.97	2.97	3.16
0.05	*bdl*	*bdl*	0.05	0.04	*bdl*	*bdl*	0.06	0.05
bdl	0.07	0.06	0.04	0.07	*bdl*	*bdl*	*bdl*	*bdl*
11.14	11.47	11.48	11.40	11.53	11.29	11.62	11.36	11.09
0.04	*bdl*	*bdl*	*bdl*	0.05	*bdl*	0.05	0.11	0.09
93.80	95.00	95.33	95.50	95.49	95.34	97.56	96.15	96.08
3.470	3.455	3.425	3.404	3.523	3.467	3.578	3.527	3.551
0.003	-	-	-	0.002	0.002	0.005	0.004	0.003
1.874	1.922	1.915	1.911	1.891	1.884	1.790	1.868	1.778
0.530	0.545	0.575	0.596	0.477	0.533	0.422	0.473	0.449
1.345	1.377	1.341	1.315	1.414	1.351	1.369	1.395	1.329
0.177	0.183	0.129	0.108	0.278	0.159	0.333	0.278	0.258
0.146	0.120	0.187	0.240	0.002	0.159	0.007	0.036	0.103
0.006	0.004	0.007	0.007	0.006	0.005	0.011	0.008	0.009
0.343	0.334	0.356	0.348	0.317	0.345	0.295	0.299	0.318
0.004	-	-	0.003	0.003	-	-	0.004	0.003
0.001	-	-	-	0.001	-	0.001	0.003	0.002
-	0.009	0.007	0.005	0.009	-	-	-	-
0.979	0.996	0.992	0.984	0.998	0.974	0.988	0.977	0.954
0.01	-	-	0.01	-	0.02	0.01	0.01	0.04
0.02	0.02	0.02	0.02	0.02	0.02	0.02	0.02	0.02
-	0.01	0.01	0.01	0.01	-	-	-	-
0.47	0.46	0.43	0.41	0.53	0.47	0.58	0.53	0.55
0.50	0.52	0.55	0.57	0.45	0.49	0.39	0.44	0.39

#16	#19	#21	#27	#28	#29	#30	#32	#33
51.11	53.29	50.96	52.83	52.41	53.04	52.84	52.20	52.00
0.05	*bdl*	*bdl*	*bdl*	*bdl*	0.05	0.07	0.05	*bdl*
21.33	22.08	22.43	20.71	18.80	20.74	21.36	19.63	18.78
7.73	7.13	8.03	7.36	8.71	6.54	6.53	7.67	8.33
0.20	0.17	0.18	0.08	0.17	0.12	0.17	0.14	0.22
2.88	3.00	2.73	3.15	4.62	3.90	3.91	3.97	3.90
0.21	0.05	0.12	*bdl*	0.07	*bdl*	*bdl*	0.09	0.08
0.09	0.04	0.05	*bdl*	*bdl*	*bdl*	*bdl*	0.10	*bdl*
9.54	10.47	9.87	11.16	10.97	11.00	11.02	10.37	10.01
0.11	0.09	0.10	0.08	*bdl*	0.06	*bdl*	0.05	0.07
93.24	96.32	94.47	95.37	95.76	95.46	95.89	94.27	93.41
3.528	3.568	3.473	3.607	3.549	3.591	3.554	3.578	3.593
0.003	-	-	-	-	0.002	0.004	0.003	-
1.735	1.743	1.801	1.667	1.500	1.655	1.693	1.586	1.529
0.472	0.432	0.527	0.393	0.451	0.409	0.446	0.422	0.407
1.263	1.311	1.274	1.273	1.049	1.246	1.248	1.164	1.122
0.172	0.231	0.133	0.322	0.094	0.212	0.169	0.163	0.142
0.274	0.168	0.324	0.098	0.399	0.158	0.199	0.277	0.340
0.011	0.010	0.011	0.004	0.010	0.007	0.009	0.008	0.013
0.296	0.300	0.278	0.321	0.467	0.394	0.392	0.405	0.402
0.016	0.003	0.009	-	0.005	-	-	0.007	0.006
0.003	0.002	0.003	0.002	-	0.002	-	0.001	0.002
0.012	0.006	0.007	-	-	-	-	0.014	-
0.840	0.895	0.858	0.972	0.948	0.950	0.946	0.907	0.883
0.13	0.09	0.12	0.02	0.04	0.04	0.05	0.07	0.11
0.02	0.02	0.02	0.02	0.02	0.02	0.02	0.02	0.02
0.01	0.01	0.01	-	-	-	-	0.01	-
0.53	0.57	0.47	0.61	0.55	0.59	0.56	0.58	0.59
0.29	0.31	0.37	0.35	0.39	0.35	0.38	0.31	0.28

#41	#42	#43	#44	#49	#51	#53	#1	#2
54.17	52.84	51.83	52.84	52.16	53.08	52.30	52.41	52.24
bdl	*bdl*	0.05	*bdl*	0.08	0.04	*bdl*	0.04	0.06
21.45	22.11	21.81	21.73	19.41	21.74	22.06	20.90	20.58
6.82	6.16	6.98	6.07	8.80	6.24	7.18	6.76	6.69
0.18	0.10	0.10	0.18	0.15	0.18	0.15	0.12	0.16
3.32	3.30	3.51	3.27	3.54	3.33	3.46	3.81	3.65
0.05	*bdl*	0.08	*bdl*	0.37	*bdl*	*bdl*	0.05	0.12
bdl	*bdl*	*bdl*	*bdl*	0.10	*bdl*	*bdl*	*bdl*	*bdl*
11.03	10.40	10.42	11.20	9.75	11.15	10.69	10.93	11.08
0.08	0.11	0.11	0.08	0.05	0.09	0.05	0.04	*bdl*
97.10	95.02	94.88	95.37	94.41	95.87	95.89	95.07	94.57
3.613	3.571	3.517	3.591	3.574	3.587	3.514	3.565	3.586
-	-	0.003	-	0.004	0.002	-	0.002	0.003
1.686	1.761	1.744	1.741	1.567	1.732	1.747	1.675	1.665
0.387	0.429	0.483	0.409	0.426	0.413	0.486	0.435	0.414
1.299	1.332	1.261	1.332	1.141	1.319	1.261	1.240	1.251
0.283	0.201	0.143	0.288	0.190	0.274	0.146	0.195	0.263
0.097	0.147	0.253	0.057	0.315	0.079	0.258	0.190	0.121
0.010	0.006	0.006	0.010	0.008	0.011	0.008	0.007	0.009
0.330	0.333	0.355	0.331	0.362	0.336	0.346	0.386	0.373
0.004	-	0.006	-	0.027	-	-	0.004	0.009
0.002	0.003	0.003	0.002	0.001	0.002	0.001	0.001	-
-	-	-	-	0.013	-	-	-	-
0.938	0.896	0.902	0.972	0.852	0.962	0.917	0.948	0.971
0.06	0.10	0.09	0.03	0.11	0.03	0.08	0.04	0.01
0.02	0.02	0.02	0.02	0.02	0.02	0.02	0.02	0.02
-	-	-	-	0.01	-	-	-	-
0.61	0.57	0.52	0.59	0.58	0.59	0.51	0.57	0.59
0.31	0.31	0.37	0.37	0.26	0.36	0.39	0.37	0.37

#3	#4	#5	#6	#7	#8	#9	#11	#12
50.86	52.20	51.58	51.02	51.59	51.24	51.07	51.19	51.79
0.04	0.05	0.05	*bdl*	0.06	0.04	*bdl*	0.05	*bdl*
19.96	19.96	20.73	22.37	20.77	21.12	22.10	21.79	20.40
7.16	7.20	7.04	6.64	6.56	7.19	7.10	6.92	7.48
0.16	0.13	0.15	0.10	0.20	0.14	0.09	0.10	0.09
3.91	3.74	3.47	3.53	3.53	3.46	3.50	3.43	3.64
0.15	*bdl*	0.05	0.12	0.09	0.12	0.07	0.11	0.07
bdl	0.07	*bdl*	0.07	*bdl*	*bdl*	*bdl*	0.05	*bdl*
10.99	11.22	11.09	10.24	11.18	10.56	10.55	10.62	10.73
bdl	0.06	*bdl*	0.06	0.14	0.08	0.11	0.07	0.05
93.23	94.63	94.17	94.16	94.11	93.94	94.59	94.32	94.23
3.545	3.593	3.559	3.479	3.568	3.527	3.479	3.507	3.559
0.002	0.003	0.003	-	0.003	0.002	-	0.002	-
1.640	1.619	1.686	1.797	1.693	1.713	1.775	1.759	1.652
0.455	0.407	0.441	0.521	0.432	0.473	0.521	0.493	0.441
1.185	1.212	1.245	1.276	1.262	1.241	1.254	1.266	1.212
0.199	0.262	0.243	0.096	0.267	0.177	0.113	0.167	0.198
0.218	0.153	0.163	0.283	0.112	0.237	0.292	0.229	0.232
0.009	0.008	0.009	0.006	0.012	0.008	0.005	0.006	0.005
0.406	0.384	0.357	0.359	0.364	0.355	0.355	0.350	0.372
0.011	-	0.003	0.009	0.007	0.009	0.005	0.008	0.005
-	0.002	-	0.002	0.004	0.002	0.003	0.002	0.001
-	0.009	-	0.009	-	-	-	0.007	-
0.977	0.985	0.976	0.891	0.986	0.927	0.917	0.928	0.941
0.01	0.00	0.02	0.09	-	0.06	0.07	0.06	0.05
0.02	0.02	0.02	0.02	0.02	0.02	0.02	0.02	0.02
-	0.01	-	0.01	-	-	-	0.01	-
0.55	0.60	0.56	0.48	0.57	0.53	0.48	0.51	0.56
0.42	0.38	0.40	0.40	0.40	0.39	0.43	0.41	0.37

Transect-3 (Inzecca)								
CO-42								
#14	#15	#16	#17	#18	#19	#21	#22	#23
51.34	50.61	50.99	50.91	50.07	51.51	51.24	51.47	50.94
0.22	0.39	0.25	0.34	0.46	0.11	0.33	0.17	0.12
20.01	20.14	20.15	19.85	19.92	20.74	21.02	20.70	20.30
7.87	7.79	7.24	7.93	8.25	6.20	6.83	7.04	7.08
0.16	0.16	0.15	0.22	0.10	0.11	0.10	0.11	0.18
3.96	3.76	3.72	4.12	3.89	3.70	3.73	4.05	3.68
bdl	*bdl*	0.06	*bdl*	0.05	0.13	0.27	0.07	*bdl*
0.07	0.08	0.07	0.07	0.09	0.06	0.06	0.06	*bdl*
11.20	11.02	10.91	10.95	10.88	10.89	10.70	10.99	11.27
bdl	*bdl*	*bdl*	0.05	0.05	0.08	0.08	*bdl*	0.07
94.84	93.94	93.54	94.44	93.74	93.51	94.35	94.65	93.63
3.524	3.506	3.543	3.502	3.478	3.571	3.521	3.521	3.545
0.012	0.020	0.013	0.018	0.024	0.005	0.017	0.008	0.006
1.618	1.645	1.650	1.609	1.631	1.695	1.702	1.669	1.665
0.476	0.494	0.457	0.498	0.522	0.429	0.479	0.479	0.455
1.142	1.151	1.192	1.111	1.108	1.267	1.223	1.189	1.210
0.178	0.179	0.208	0.118	0.140	0.242	0.199	0.147	0.231
0.274	0.273	0.213	0.338	0.339	0.117	0.193	0.256	0.180
0.009	0.010	0.009	0.013	0.006	0.006	0.006	0.006	0.011
0.405	0.388	0.385	0.423	0.403	0.382	0.382	0.413	0.382
-	-	0.005	-	0.003	0.009	0.020	0.005	-
-	-	-	0.001	0.001	0.002	0.002	-	0.002
0.010	0.011	0.009	0.009	0.012	0.008	0.008	0.008	-
0.980	0.974	0.967	0.961	0.965	0.963	0.938	0.959	1.000
0.01	0.01	0.02	0.03	0.02	0.02	0.03	0.03	-
0.02	0.02	0.02	0.02	0.02	0.02	0.02	0.02	0.02
0.01	0.01	0.01	0.01	0.01	0.01	0.01	0.01	-
0.54	0.53	0.56	0.52	0.50	0.58	0.54	0.53	0.55
0.44	0.44	0.40	0.43	0.45	0.38	0.39	0.42	0.43

#24	#25	#26	#27	#28	#29	#31	#32	#33
52.10	51.06	51.96	51.65	50.67	51.47	50.60	50.60	50.69
0.34	0.30	0.20	0.19	1.34	0.14	0.33	0.36	0.30
20.07	20.51	19.97	20.71	20.28	19.17	18.74	18.54	18.70
6.89	7.35	7.04	6.84	7.69	7.96	8.83	8.41	8.74
0.21	0.11	0.14	0.23	0.16	0.09	0.19	0.11	0.12
3.59	3.74	3.87	3.82	3.37	4.08	4.20	4.29	4.15
0.17	0.08	*bdl*	0.05	0.32	*bdl*	*bdl*	*bdl*	*bdl*
bdl	*bdl*	0.10	*bdl*	*bdl*	*bdl*	*bdl*	*bdl*	*bdl*
11.06	11.08	11.01	11.10	10.88	11.04	10.95	11.07	10.97
0.08	0.07	*bdl*	0.06	0.13	0.09	0.06	0.04	0.06
94.50	94.30	94.29	94.65	94.83	94.04	93.90	93.41	93.73
3.593	3.522	3.578	3.541	3.500	3.562	3.512	3.532	3.526
0.017	0.016	0.010	0.010	0.069	0.007	0.017	0.019	0.015
1.631	1.668	1.621	1.673	1.651	1.563	1.533	1.525	1.533
0.407	0.478	0.422	0.459	0.500	0.438	0.488	0.468	0.474
1.224	1.189	1.199	1.215	1.150	1.126	1.045	1.058	1.059
0.293	0.198	0.224	0.193	0.290	0.189	0.122	0.154	0.148
0.105	0.226	0.181	0.199	0.154	0.272	0.390	0.336	0.360
0.012	0.006	0.008	0.013	0.009	0.005	0.011	0.007	0.007
0.369	0.385	0.398	0.390	0.347	0.421	0.435	0.446	0.430
0.012	0.006	-	0.003	0.024	-	-	-	-
0.002	0.002	-	0.002	0.004	0.002	0.002	0.001	0.002
-	-	0.013	-	-	-	-	-	-
0.973	0.975	0.967	0.971	0.958	0.975	0.969	0.986	0.973
0.01	0.02	0.02	0.02	0.01	0.02	0.02	0.01	0.02
0.02	0.02	0.02	0.02	0.02	0.02	0.02	0.02	0.02
-	-	0.01	-	-	-	-	-	-
0.61	0.54	0.59	0.55	0.57	0.57	0.53	0.55	0.54
0.35	0.43	0.37	0.41	0.38	0.40	0.43	0.42	0.42

#34	#35	#36	#37	#38	#39	#40	#41	#42
51.01	52.01	51.27	51.67	51.63	51.87	51.64	51.10	51.25
0.26	0.08	0.13	0.10	0.12	0.11	0.08	0.16	0.16
20.97	20.34	19.97	20.72	20.60	21.02	20.52	20.87	21.05
6.86	6.39	8.03	6.47	6.41	6.35	6.65	6.70	6.40
0.06	0.12	0.08	0.15	0.12	0.14	0.14	0.16	0.07
3.96	3.77	3.86	4.04	4.02	3.80	3.89	3.94	4.04
bdl	0.05	0.05	*bdl*	*bdl*	*bdl*	*bdl*	*bdl*	*bdl*
bdl	*bdl*	*bdl*	0.05	0.07	*bdl*	0.07	0.07	0.05
10.86	11.29	11.01	11.00	11.25	11.27	10.63	10.95	10.85
0.05	0.08	0.06	*bdl*	0.05	*bdl*	0.07	*bdl*	*bdl*
94.03	94.13	94.46	94.19	94.29	94.56	93.68	93.95	93.86
3.505	3.594	3.530	3.546	3.554	3.556	3.559	3.518	3.522
0.013	0.004	0.007	0.005	0.006	0.006	0.004	0.008	0.008
1.698	1.657	1.620	1.676	1.671	1.698	1.666	1.694	1.705
0.495	0.406	0.470	0.454	0.446	0.444	0.441	0.482	0.478
1.204	1.251	1.150	1.222	1.225	1.254	1.225	1.213	1.227
0.134	0.273	0.180	0.162	0.201	0.219	0.167	0.149	0.138
0.260	0.097	0.282	0.209	0.168	0.145	0.216	0.237	0.230
0.004	0.007	0.005	0.009	0.007	0.008	0.008	0.009	0.004
0.405	0.388	0.396	0.413	0.413	0.388	0.399	0.404	0.413
-	0.004	0.004	-	-	-	-	-	-
0.001	0.002	0.002	-	0.001	-	0.002	-	-
-	-	-	0.007	0.009	-	0.010	0.010	0.007
0.952	0.995	0.967	0.963	0.988	0.985	0.935	0.961	0.951
0.04	-	0.02	0.03	0.00	0.01	0.05	0.03	0.04
0.02	0.02	0.02	0.02	0.02	0.02	0.02	0.02	0.02
-	-	-	0.01	0.01	-	0.01	0.01	0.01
0.52	0.60	0.54	0.55	0.56	0.56	0.56	0.53	0.53
0.42	0.38	0.42	0.40	0.42	0.41	0.36	0.42	0.41

#43	#44	#45	#46	#49	#50	#51	#53	#54
51.88	51.90	51.52	52.28	51.37	50.96	51.58	51.82	51.90
0.06	0.08	0.05	*bdl*	*bdl*	*bdl*	*bdl*	0.07	0.05
20.65	20.73	21.68	20.41	21.65	21.44	21.18	21.48	20.58
6.67	6.39	6.34	6.58	6.60	6.41	6.46	6.75	6.64
0.20	0.14	0.15	0.18	0.13	0.13	0.18	0.14	0.16
3.45	3.67	3.44	3.67	3.47	3.39	3.60	3.29	3.63
0.12	0.06	0.10	0.16	0.11	0.14	0.14	0.09	0.07
0.05	0.06	0.07	0.07	0.05	0.05	0.09	*bdl*	*bdl*
10.81	11.18	9.67	10.55	10.35	10.51	10.59	10.34	10.38
0.07	0.06	0.06	*bdl*	0.05	0.04	0.05	0.07	*bdl*
93.94	94.28	93.08	93.90	93.78	93.07	93.86	94.06	93.40
3.584	3.578	3.538	3.598	3.526	3.535	3.550	3.551	3.579
0.003	0.004	0.003	-	-	-	-	0.004	0.002
1.681	1.684	1.755	1.656	1.751	1.753	1.718	1.735	1.673
0.416	0.422	0.462	0.402	0.474	0.465	0.450	0.449	0.421
1.265	1.262	1.293	1.254	1.277	1.289	1.268	1.285	1.252
0.260	0.260	0.115	0.234	0.157	0.199	0.197	0.196	0.186
0.125	0.108	0.249	0.144	0.222	0.173	0.175	0.190	0.197
0.011	0.008	0.008	0.010	0.007	0.007	0.010	0.008	0.009
0.356	0.377	0.352	0.376	0.355	0.351	0.369	0.336	0.373
0.009	0.004	0.008	0.012	0.008	0.010	0.010	0.007	0.005
0.002	0.002	0.002	-	0.001	0.001	0.001	0.002	-
0.007	0.008	0.009	0.010	0.007	0.007	0.012	-	-
0.952	0.983	0.847	0.926	0.906	0.930	0.929	0.904	0.913
0.03	-	0.13	0.05	0.08	0.05	0.05	0.08	0.08
0.02	0.02	0.02	0.02	0.02	0.02	0.02	0.02	0.02
0.01	0.01	0.01	0.01	0.01	0.01	0.01	-	-
0.59	0.58	0.54	0.60	0.53	0.54	0.55	0.55	0.58
0.36	0.39	0.29	0.32	0.37	0.38	0.37	0.34	0.32

#55	#56
52.42	51.85
bdl	0.07
20.13	20.68
6.89	7.02
0.19	*bdl*
3.79	3.47
0.10	0.23
0.05	0.05
10.44	9.79
0.05	0.05
94.07	93.19
3.597	3.574
-	0.003
1.628	1.680
0.403	0.426
1.225	1.253
0.197	0.182
0.198	0.222
0.011	-
0.388	0.356
0.008	0.017
0.001	0.001
0.006	0.007
0.914	0.860
0.07	0.11
0.02	0.02
0.01	0.01
0.60	0.58
0.30	0.27

Representative EMPA and chemical formulas of Feldspar

Locality					Transect 1 (Casti	
Sample	CO-24		CO-25			
Type	Igneous	Metamorphic	Igneous	Metamorphic		Igne
Analysis	#13	#14	#14	#26	#1	#37
SiO_2 (wt%)	64.34	69.70	62.07	67.34	64.45	64.16
Al_2O_3	18.56	19.94	18.85	19.53	18.36	18.63
FeOt	*bdl*	0.06	0.83	*bdl*	0.08	0.47
CaO	*bdl*	0.28	*bdl*	0.05	*bdl*	0.09
Na_2O	0.12	10.84	0.51	11.73	0.20	0.19
K_2O	16.83	0.31	15.94	0.09	17.11	17.06
BaO	0.47	*bdl*	0.36	*bdl*	0.04	0.10
Total	100.31	101.13	98.56	98.74	100.25	100.70
Fe_2O_3	0.00	0.07	0.93	-	0.09	0.53
Formula (8 Oxygens)						
Si (apfu)	2.983	3.002	2.923	2.981	2.986	2.963
Al	1.014	1.012	1.046	1.019	1.003	1.014
Fe^{3+}	-	0.002	0.033	-	0.003	0.018
Ba	0.008	-	0.007	-	0.001	0.002
Ca	-	0.013	-	0.002	-	0.004
Na	0.012	0.905	0.046	1.007	0.018	0.017
K	0.996	0.017	0.957	0.005	1.011	1.005
XAn	-	0.01	0.01	0.00	-	0.01
XAb	0.02	0.97	0.05	0.99	0.02	0.02
XOr	0.98	0.02	0.95	0.00	0.98	0.98

* FeOt total iron reported as FeO; apfu: atoms per formula unit; bdl: below detection limit.

** TiO_2, MnO and MgO always below detection limit.

irla)							Transe
CO-38						CO-35	
eous		Metamorphic				Metamorphic	
#42	#14	#2	#43	#1	#2	#94	#97
64.27	64.56	68.35	67.04	70.68	67.84	68.31	67.86
18.69	18.24	19.79	20.09	20.24	19.86	19.66	19.89
0.05	0.14	0.15	0.10	0.27	0.22	0.16	0.10
bdl	*bdl*	0.07	0.62	0.66	0.41	*bdl*	0.44
0.34	0.27	11.78	10.88	8.68	11.84	11.88	11.61
17.12	16.86	0.08	0.30	1.24	0.15	0.14	0.12
bdl	*bdl*	*bdl*	*bdl*	*bdl*	*bdl*	*bdl*	*bdl*
100.47	100.08	100.22	99.02	101.76	100.31	100.15	100.02
0.05	0.16	0.17	0.11	0.30	0.24	0.17	0.11
2.974	2.993	2.981	2.961	3.016	2.964	2.983	2.969
1.019	0.997	1.017	1.046	1.018	1.023	1.012	1.026
0.002	0.006	0.005	0.004	0.010	0.008	0.006	0.004
-	-	-	-	-	-	0.000	0.000
-	-	0.003	0.029	0.030	0.019	-	0.021
0.031	0.024	0.996	0.932	0.718	1.003	1.006	0.985
1.010	0.997	0.005	0.017	0.067	0.008	0.008	0.007
-	-	0.00	0.03	0.04	0.02	-	0.02
0.03	0.02	0.99	0.95	0.88	0.97	0.99	0.97
0.97	0.98	0.00	0.02	0.08	0.01	0.01	0.01

ct-2 (Vivario-Venaco)			transect-3 (Inzecca)				
CO-36			CO-42				
Igneous		Metamorphic	Igneous				M
#1	#27	#23	#25	#37	#47	#9	#26
64.71	65.18	69.23	64.01	63.87	63.70	64.25	69.35
18.34	18.21	19.28	18.11	18.46	18.30	18.30	19.56
bdl	0.08	0.05	0.51	0.54	0.08	*bdl*	0.11
bdl	*bdl*	*bdl*	*bdl*	*bdl*	*bdl*	*bdl*	*bdl*
bdl	0.25	11.31	0.20	0.32	0.14	0.21	11.98
16.23	17.08	0.09	17.15	16.91	17.05	16.79	0.08
0.21	0.11	*bdl*	*bdl*	0.24	0.15	0.12	*bdl*
99.48	100.91	99.97	99.99	100.34	99.41	99.67	101.07
-	0.09	0.05	0.57	0.60	0.09	-	0.12
3.003	2.999	3.016	2.980	2.966	2.981	2.991	2.997
1.003	0.987	0.990	0.994	1.011	1.009	1.004	0.996
-	0.003	0.002	0.020	0.021	0.003	-	0.004
0.004	0.002	0.000	-	0.004	0.003	0.002	-
-	-	-	-	-	-	-	-
-	0.022	0.956	0.018	0.029	0.012	0.019	1.004
0.964	1.003	0.005	1.019	1.002	1.018	0.997	0.004
-	-	-	-	-	-	-	-
-	0.02	0.99	0.02	0.03	0.01	0.02	1.00
1.00	0.98	0.01	0.98	0.97	0.99	0.98	-

Metamorphic	
#3	#10
70.09	69.87
19.50	19.06
0.18	*bdl*
bdl	*bdl*
11.47	10.98
bdl	0.05
bdl	*bdl*
101.24	99.96
0.20	-
3.014	3.034
0.988	0.975
0.006	-
-	-
-	-
0.957	0.925
-	0.003
-	-
1.00	1.00
-	-

Representative EMPA and chemical formulas of Stilpnomela

Locality						Tra
Sample	CO-24	CO-25				
Analysis	#36	#37	#14	#15	#16	#17
SiO_2 (wt%)	43.93	43.99	44.54	46.28	43.98	42.84
TiO_2	*bdl*	*bdl*	0.24	0.19	0.12	0.15
Al_2O_3	5.85	6.08	5.87	5.75	6.42	7.09
FeOt	34.19	33.90	29.96	29.52	29.52	29.61
MnO	0.45	0.41	2.19	2.24	2.17	2.12
MgO	2.07	1.91	3.25	3.16	3.46	3.51
CaO	0.10	0.13	0.23	0.22	0.12	0.20
Na_2O	0.21	0.37	0.53	0.52	0.48	0.49
K_2O	2.04	2.19	1.98	1.84	2.44	2.96
Total	88.83	88.98	88.79	89.72	88.71	88.98
FeO	22.45	22.07	17.81	17.22	17.54	17.63
Fe_2O_3	13.05	13.16	13.50	13.66	13.32	13.31
Formula (120 Cations)						
Si (apfu)	63.60	63.83	64.09	65.73	63.34	61.86
$Al^{[IV]}$	8.40	8.17	7.91	6.27	8.66	10.14
Ti	-	-	0.26	0.20	0.13	0.17
$Al^{[VI]}$	1.58	2.23	2.05	3.36	2.24	1.92
Fe^{2+}	27.18	26.78	21.43	20.46	21.12	21.29
Fe^{3+}	14.22	14.36	14.62	14.60	14.43	14.47
Mn	0.55	0.50	2.67	2.70	2.64	2.59
Mg	4.46	4.13	6.97	6.68	7.43	7.56
Ca	0.15	0.20	0.35	0.33	0.19	0.32
Na	0.58	1.03	1.47	1.44	1.34	1.37
K	3.77	4.06	3.64	3.34	4.47	5.46
(OH)	32.19	31.41	31.08	29.84	31.20	31.44

* FeOt total iron reported as FeO; apfu: atoms per formula unit; bdl: below detection lim

**(OH) by stochiometry

ıne

ansect-1 (Castirla)								
		CO-38						
#18	#19	#23	#24	#25	#5	#6	#7	#19
44.44	43.80	47.20	43.59	42.78	45.47	45.47	44.29	47.62
0.13	*bdl*	0.17	0.12	*bdl*	*bdl*	*bdl*	*bdl*	*bdl*
6.46	6.23	5.69	6.52	6.46	5.86	5.51	5.46	6.44
30.77	29.92	29.16	30.85	31.09	29.68	29.86	27.89	27.58
2.02	2.00	2.05	2.00	2.21	1.86	2.20	3.41	3.21
3.57	3.90	2.91	3.85	3.40	3.60	3.54	4.41	4.40
0.23	0.23	1.00	0.44	0.11	0.23	0.26	0.20	0.19
0.48	0.57	0.61	0.59	0.50	0.62	0.36	0.34	0.12
2.34	1.95	2.02	1.92	1.86	1.62	1.33	1.53	0.64
90.45	88.61	90.82	89.88	88.40	88.94	88.52	87.51	90.19
18.50	17.87	16.01	18.63	19.41	17.52	17.86	15.93	16.06
13.63	13.39	14.62	13.59	12.98	13.51	13.33	13.28	12.80
62.80	62.80	67.03	61.83	61.60	64.83	64.90	63.64	65.27
9.20	9.20	4.97	10.17	10.40	7.17	7.10	8.36	6.73
0.14	-	0.18	0.12	-	-	-	-	-
1.55	1.33	4.55	0.73	0.57	2.68	2.17	0.88	3.67
21.87	21.43	19.01	22.09	23.37	20.89	21.32	19.15	18.41
14.50	14.45	15.63	14.51	14.06	14.50	14.32	14.36	13.21
2.42	2.43	2.46	2.41	2.69	2.25	2.65	4.15	3.72
7.53	8.33	6.16	8.14	7.30	7.66	7.53	9.44	8.99
0.35	0.35	1.52	0.67	0.17	0.35	0.39	0.30	0.28
1.33	1.59	1.69	1.61	1.40	1.70	1.01	0.93	0.31
4.22	3.56	3.66	3.48	3.41	2.95	2.42	2.80	1.12
31.81	32.19	27.64	32.64	33.36	30.80	31.51	32.74	31.12

ıit.

Transect-2 (Vivario-Venaco)								
CO-36								
#20	#21	#22	#24	#25	#26	#34	#35	#13
47.03	48.56	46.55	47.14	46.90	46.75	49.04	47.33	48.76
bdl	*bdl*	*bdl*	*bdl*	*bdl*	*bdl*	*bdl*	*bdl*	0.07
5.98	6.92	5.74	5.94	5.93	5.95	5.97	5.87	7.83
28.00	25.84	28.89	28.50	28.38	28.15	28.37	28.61	24.25
3.58	3.32	3.55	3.82	3.86	3.64	3.55	3.20	1.02
4.54	4.29	4.49	4.46	4.40	4.17	4.07	4.43	4.88
0.29	0.16	0.20	0.23	0.21	0.32	0.17	0.29	0.31
0.08	0.87	0.09	0.09	0.10	0.10	0.08	0.20	0.19
0.91	1.17	0.94	0.87	0.96	0.70	0.88	1.04	2.35
90.41	91.12	90.45	91.05	90.73	89.77	92.12	90.97	89.65
16.12	13.73	16.96	16.57	16.47	16.44	16.35	16.49	12.52
13.21	13.45	13.26	13.26	13.23	13.02	13.36	13.47	13.03
64.66	66.58	64.08	64.38	64.36	64.77	66.21	64.90	67.68
7.34	5.42	7.92	7.62	7.64	7.23	5.79	7.10	4.32
-	-	-	-	-	-	-	-	0.07
2.34	5.76	1.38	1.94	1.95	2.49	3.71	2.38	8.49
18.53	15.75	19.52	18.93	18.90	19.05	18.46	18.91	14.54
13.66	13.88	13.73	13.63	13.66	13.58	13.57	13.90	13.61
4.17	3.85	4.14	4.42	4.48	4.27	4.05	3.72	1.20
9.30	8.76	9.22	9.08	9.00	8.62	8.20	9.05	10.09
0.43	0.23	0.29	0.34	0.30	0.47	0.25	0.42	0.46
0.21	2.32	0.25	0.24	0.26	0.26	0.21	0.52	0.50
1.60	2.04	1.66	1.51	1.68	1.24	1.51	1.82	4.16
32.00	28.36	32.88	32.42	32.39	31.93	30.71	31.68	25.83

Transect-3 (Inzecca)								
CO-42								
#58	#59	#14	#20	#23	#24	#34	#35	#36
45.59	47.37	46.29	44.86	45.93	44.78	47.28	46.22	45.97
0.06	*bdl*	*bdl*	0.07	0.04	0.14	*bdl*	*bdl*	*bdl*
6.63	7.80	5.90	10.87	7.88	8.16	6.51	6.51	6.24
26.25	26.58	30.83	25.67	28.18	31.67	30.15	30.61	31.50
1.48	1.38	1.19	0.98	1.45	0.89	1.02	0.88	1.07
4.84	5.75	4.13	4.11	5.10	3.89	4.97	5.08	4.93
0.34	0.15	0.15	0.42	0.30	0.66	0.35	0.41	0.32
0.22	*bdl*	0.08	0.22	0.19	0.33	0.16	0.19	0.26
0.71	1.15	0.98	3.06	1.36	0.43	0.47	0.55	0.66
86.10	90.17	89.55	90.27	90.45	90.96	90.93	90.46	90.95
15.16	15.38	19.16	14.91	16.78	20.46	18.41	18.83	19.54
12.32	12.44	12.97	11.96	12.67	12.46	13.05	13.09	13.28
65.23	64.19	64.42	62.49	62.88	61.38	64.14	63.16	62.74
6.77	7.81	7.58	9.51	9.12	10.62	7.86	8.84	9.26
0.06	-	-	0.08	0.04	0.15	-	-	-
4.41	4.65	2.10	8.32	3.60	2.56	2.56	1.64	0.77
18.14	17.43	22.31	17.37	19.21	23.45	20.88	21.52	22.31
13.27	12.69	13.58	12.53	13.05	12.85	13.32	13.47	13.64
1.79	1.59	1.41	1.16	1.68	1.04	1.17	1.02	1.24
10.33	11.62	8.58	8.54	10.42	7.95	10.06	10.35	10.04
0.52	0.21	0.22	0.62	0.44	0.97	0.51	0.61	0.47
0.62	-	0.20	0.61	0.51	0.88	0.43	0.50	0.68
1.29	1.99	1.73	5.45	2.38	0.76	0.82	0.96	1.16
30.26	30.64	32.29	27.07	31.31	32.44	32.12	32.89	33.59

#45	#46	#54
45.80	45.37	46.41
0.08	0.04	*bdl*
6.20	6.13	6.72
29.66	29.89	29.53
1.01	1.69	1.01
5.02	5.41	4.83
0.30	0.19	0.28
0.10	0.05	0.38
0.54	0.47	1.19
88.71	89.25	90.33
18.15	18.40	17.62
12.79	12.77	13.23
63.68	62.50	63.96
8.32	9.50	8.04
0.09	0.05	-
1.84	0.45	2.87
21.10	21.20	20.31
13.38	13.23	13.72
1.19	1.97	1.17
10.40	11.11	9.92
0.44	0.29	0.42
0.27	0.13	1.01
0.96	0.83	2.08
32.69	34.27	31.40

Representative EMPA and chemical formulas of Biotite

Locality	Transect1 (Castirla)			
Sample	CO-38			
Analysis	#26	#27	#39	#41
SiO_2 (wt%)	39.03	39.56	35.99	37.17
TiO_2	0.55	0.58	0.68	0.92
Al_2O_3	17.86	18.93	16.88	17.18
FeOt	22.50	21.56	26.69	24.42
MnO	0.30	0.30	0.47	0.40
MgO	4.01	3.90	5.08	4.37
CaO	*bdl*	*bdl*	*bdl*	*bdl*
Na_2O	*bdl*	0.04	0.06	*bdl*
K_2O	10.44	10.49	8.29	10.05
Total	94.71	95.37	94.15	94.51
Formula (11 Oxygens; $Fe_{total} = Fe^{2+}$)				
Si (apfu)	3.019	3.015	2.858	2.925
$Al^{[IV]}$	0.981	0.985	1.142	1.075
Ti	0.032	0.033	0.041	0.055
$Al^{[VI]}$	0.647	0.715	0.438	0.518
Fe^{2+}	1.455	1.374	1.772	1.607
Mn	0.020	0.019	0.031	0.027
Mg	0.463	0.443	0.602	0.512
Ca	-	-	-	-
Na	-	0.007	0.009	-
K	1.030	1.020	0.840	1.009
$^{(a)}$XMg	0.24	0.24	0.25	0.24

* FeOt total iron reported as FeO; apfu: atoms per formula unit; bdl: below detection limit.

(a) XMg as [$Mg/(Mg+Fe^{2+})$]

Representative EMPA and chemical formulas of Chlorite

Locality	Transect1 (Castirla)					
Sample	CO-25					
Analysis	#7	#8	#10	#12	#14	#20
SiO_2 (wt%)	25.04	24.57	24.61	24.86	25.52	24.61
TiO_2	*bdl*	*bdl*	0.04	0.05	0.05	*bdl*
Al_2O_3	18.33	18.60	18.57	17.63	17.63	17.96
FeOt	35.45	35.49	36.57	36.52	35.31	36.68
MnO	1.22	1.15	1.08	1.00	1.01	1.16
MgO	7.74	7.26	7.44	7.34	7.39	6.74
CaO	*bdl*	0.06	0.04	0.34	0.45	*bdl*
Na_2O	*bdl*	*bdl*	*bdl*	*bdl*	*bdl*	*bdl*
K_2O	*bdl*	*bdl*	*bdl*	*bdl*	0.07	*bdl*
Total	87.77	87.13	88.34	87.74	87.42	87.15
Formula (14 Oxygens)						
Si (apfu)	2.818	2.793	2.762	2.825	2.909	2.812
$Al^{[IV]}$	1.182	1.207	1.238	1.175	1.091	1.188
Ti	-	-	0.003	0.005	0.004	-
$Al^{[VI]}$	1.249	1.285	1.218	1.185	1.277	1.232
Fe^{2+}	3.336	3.373	3.418	3.471	3.366	3.506
Fe^{3+}	-	-	0.014	-	-	-
Mn	0.116	0.111	0.103	0.096	0.097	0.112
Mg	1.298	1.230	1.245	1.243	1.255	1.148
$^{(a)}$XMg	0.27	0.26	0.26	0.26	0.27	0.24

* FeOt total iron reported as FeO; apfu: atoms per formula unit; bdl: below detection lin
(a) XMg as [Mg / (Mg + Fe2+)].

		CO-38
#23	#32	#22
24.55	24.85	24.12
0.10	0.17	0.10
18.59	17.39	16.41
36.82	36.89	39.94
0.90	0.78	1.29
6.81	6.43	5.82
0.15	0.35	0.85
bdl	*bdl*	*bdl*
bdl	0.18	*bdl*
87.91	87.04	88.53
2.782	2.871	2.782
1.218	1.129	1.218
0.008	0.015	0.009
1.265	1.238	1.012
3.490	3.564	3.664
-	-	0.189
0.086	0.076	0.126
1.151	1.107	1.000
0.24	0.23	0.20

mit.

Representative EMPA and chemical formulas of Epidote

Locality	Transect-1					
Sample	CO-25	CO-38				
Analysis	#2	#36	#71	#72	#73	#74
SiO_2 (wt%)	36.34	37.33	36.65	36.19	36.47	36.50
TiO_2	*bdl*	0.10	0.04	*bdl*	*bdl*	0.04
Al_2O_3	20.34	20.93	21.76	18.63	19.59	19.03
FeOt	15.13	15.32	13.12	17.19	16.05	16.84
MnO	0.35	0.29	0.64	0.18	0.16	0.23
MgO	*bdl*	*bdl*	*bdl*	*bdl*	*bdl*	0.07
CaO	22.55	21.54	22.65	22.78	23.02	23.00
Total	94.72	95.52	94.86	94.97	95.29	95.71
Fe_2O_3	16.82	17.04	14.59	19.11	17.83	18.72
Mn_2O_3	0.39	0.33	0.71	0.20	0.18	0.25
Formula (12.5 Oxygens)						
Si (apfu)	2.983	3.021	2.987	2.984	2.988	2.985
Ti	-	0.006	0.003	-	-	0.003
Al^{Tot}	1.968	1.996	2.090	1.810	1.891	1.834
Fe^{3+}	1.039	1.037	0.894	1.185	1.099	1.152
Mn^{3+}	0.025	0.020	0.044	0.013	0.011	0.016
Mg	-	-	-	-	-	0.008
Ca	1.984	1.867	1.978	2.012	2.020	2.015
$^{(a)}$XPs	0.35	0.34	0.30	0.40	0.37	0.39

* FeOt total iron reported as FeO; apfu: atoms per formula unit; bdl: below detection limit.

** Na_2O and K_2O always below detection limit.

(a) XPs: Pistacite as [Fe^{3+} / (Fe^{3+} + Al^{3+})] atomic ratio.

Transect-2 (Vivario-Venaco)								
CO-35						CO-36		
#98	#6	#7	#11	#12	#17	#2	#15	#21
36.78	36.59	36.34	37.93	36.47	36.93	37.39	37.19	37.22
bdl	0.07	0.08	0.04	0.05	*bdl*	0.18	0.11	0.12
20.71	20.65	19.51	21.32	20.99	21.86	21.65	21.85	21.72
14.36	14.53	16.22	14.67	14.82	13.50	13.95	13.49	14.15
0.28	0.31	0.50	0.21	0.16	0.22	0.20	0.06	0.09
bdl	*bdl*	*bdl*	*bdl*	*bdl*	*bdl*	*bdl*	*bdl*	*bdl*
22.61	22.69	22.62	22.75	22.96	23.19	23.18	23.16	23.47
94.75	94.83	95.27	96.92	95.45	95.69	96.55	95.87	96.77
15.99	16.15	18.03	16.30	16.47	15.01	15.53	15.01	15.73
0.31	0.34	0.55	0.23	0.18	0.24	0.22	0.07	0.10
3.009	2.993	2.978	3.025	2.968	2.987	2.996	2.999	2.981
-	0.004	0.005	0.003	0.003	-	0.011	0.007	0.007
1.997	1.991	1.885	2.005	2.013	2.083	2.045	2.077	2.050
0.983	0.994	1.112	0.978	1.009	0.913	0.935	0.910	0.947
0.019	0.021	0.035	0.014	0.011	0.015	0.013	0.004	0.006
-	-	-	-	-	-	-	-	-
1.982	1.989	1.986	1.944	2.003	2.009	1.991	2.001	2.016
0.33	0.33	0.37	0.33	0.33	0.30	0.31	0.30	0.32

		Transect-3 (Inzecca)	
		CO-42	
#31	#32	#105	#106
37.18	37.29	37.42	38.53
0.16	0.26	*bdl*	0.18
23.49	23.66	26.00	28.22
11.01	11.45	8.45	6.41
0.37	0.25	0.26	0.06
bdl	*bdl*	*bdl*	*bdl*
21.18	22.20	23.67	24.14
93.39	95.11	95.81	97.55
12.26	12.74	9.40	7.13
0.42	0.28	0.29	0.07
3.035	3.002	2.976	2.987
0.010	0.016	-	0.010
2.260	2.245	2.437	2.578
0.752	0.771	0.562	0.415
0.026	0.017	0.018	0.004
-	-	-	-
1.852	1.915	2.017	2.005
0.25	0.26	0.19	0.14

Representative EMPA and chemical formulas of Garnet

Locality						
Sample						
Analysis	#56	#57	#60	#62	#63	#77
SiO_2 (wt%)	33.96	33.70	34.32	34.76	34.13	33.65
TiO_2	0.24	0.08	1.12	0.19	0.18	0.17
Al_2O_3	5.61	5.13	6.89	8.85	6.49	6.23
FeOt	20.22	20.94	17.64	17.02	18.71	19.52
MnO	0.43	0.40	1.39	2.54	0.68	0.66
MgO	0.05	0.05	*bdl*	0.05	*bdl*	0.10
CaO	34.49	34.35	33.02	32.59	33.86	32.93
Total	94.99	94.65	94.36	95.99	94.06	93.25
Fe_2O_3	*22.47*	*23.27*	*19.01*	*18.69*	*20.79*	*21.68*
FeO	-	-	*0.54*	*0.20*	-	*0.01*
H_2O	*1.62*	*1.68*	*1.11*	*1.45*	*1.22*	*1.33*
Formula (8 Cations)						
Si (apfu)	2.779	2.770	2.847	2.805	2.831	2.814
H /4	0.221	0.230	0.153	0.195	0.169	0.186
Ti	0.015	0.005	0.070	0.012	0.011	0.011
Al^{Tot}	0.541	0.497	0.674	0.842	0.634	0.614
Fe^{3+}	1.384	1.439	1.187	1.135	1.298	1.365
Fe^{2+}	-	-	0.037	0.014	-	0.001
Mn^{3+}	0.030	0.028	0.098	0.174	0.048	0.047
Mg	0.006	0.006	-	0.006	-	0.013
Ca	3.024	3.025	2.935	2.818	3.009	2.951
$^{(a)}$Grs	0.275	0.247	0.341	0.365	0.317	0.294
$^{(a)}$Hgr	0.074	0.077	0.051	0.065	0.056	0.062
$^{(a)}$Adr	0.713	0.742	0.615	0.571	0.668	0.686
$^{(a)}$Alm	-	-	0.012	0.005	-	-
$^{(a)}$Prp	0.002	0.002	-	0.002	-	0.004
$^{(a)}$Sps	0.010	0.009	0.032	0.058	0.016	0.016

* FeOt total iron reported as FeO; apfu: atoms per formula unit; bdl: below detection lin

** Na_2O and K_2O always below detection limit.

(a) Grs: Grossular; Hgr: Hydrogrossular; Adr: Andradite; Alm: Almandine; Prp: Pyrope; Sp

Transect-2 (Vivario-Venaco)								
	CO-35							
#78	#3	#4	#5	#6	#9	#10	#13	#14
34.53	33.45	34.70	34.30	35.63	34.71	34.78	34.78	33.73
0.19	0.43	0.31	0.18	0.41	0.06	0.13	*bdl*	*bdl*
6.83	7.05	8.32	6.35	8.98	4.50	7.92	5.53	8.16
19.32	19.11	17.59	20.18	16.83	22.05	17.81	20.70	17.77
0.34	0.44	1.05	0.34	3.79	0.37	1.05	1.29	0.41
0.15	*bdl*	*bdl*	0.07	*bdl*	*bdl*	*bdl*	*bdl*	*bdl*
33.50	34.83	34.02	34.48	30.97	33.92	34.16	33.81	35.18
94.86	95.32	95.99	95.89	96.62	95.62	95.85	96.11	95.24
21.22	*21.22*	*19.35*	*22.43*	*17.73*	*24.51*	*19.79*	*23.00*	*19.75*
0.23	*0.02*	*0.18*	-	*0.87*	-	-	-	-
1.15	*2.36*	*1.53*	*1.68*	*0.71*	*0.93*	*1.39*	*1.14*	*2.27*
2.842	2.684	2.794	2.774	2.903	2.871	2.813	2.844	2.698
0.158	0.316	0.206	0.226	0.097	0.129	0.187	0.156	0.302
0.012	0.026	0.019	0.011	0.025	0.004	0.008	-	-
0.663	0.667	0.790	0.605	0.862	0.439	0.755	0.533	0.769
1.314	1.281	1.173	1.365	1.087	1.525	1.205	1.416	1.189
0.016	0.001	0.012	-	0.060	-	-	-	-
0.024	0.030	0.072	0.023	0.262	0.026	0.072	0.089	0.028
0.018	-	-	0.008	-	-	-	-	-
2.954	2.995	2.935	2.987	2.704	3.006	2.960	2.962	3.015
0.320	0.341	0.380	0.301	0.343	0.216	0.364	0.244	0.384
0.053	0.105	0.069	0.075	0.032	0.043	0.062	0.052	0.101
0.661	0.649	0.592	0.689	0.551	0.775	0.612	0.727	0.607
0.005	-	0.004	-	0.020	-	-	-	-
0.006	-	-	0.003	-	-	-	-	-
0.008	0.010	0.024	0.008	0.087	0.009	0.024	0.029	0.009

mit.

ps: Spessartine.

#15	#16	#19
33.29	33.12	33.95
bdl	*bdl*	0.11
7.61	5.73	5.73
18.68	20.94	20.75
0.52	0.63	0.60
bdl	0.09	0.23
34.92	34.42	33.91
95.02	94.93	95.27
20.76	*23.27*	*23.06*
-	-	-
2.51	*2.38*	*1.72*
2.666	2.679	2.766
0.335	0.321	0.234
-	-	0.007
0.718	0.546	0.550
1.251	1.417	1.414
-	-	-
0.035	0.043	0.041
-	0.011	0.028
2.996	2.983	2.960
0.353	0.261	0.260
0.112	0.107	0.078
0.635	0.722	0.717
-	-	-
-	0.004	0.009
0.012	0.014	0.014

Representative EMPA and chemical formulas of Amphibole

Locality	Transect-1		Transect-2		
Sample	CO-38		CO-35	CO-36	
Analysis	#28	#29	#13	#29	#33
SiO_2 (wt%)	53.36	53.36	52.98	55.13	57.28
TiO_2	0.10	0.09	0.37	0.05	0.05
Al_2O_3	1.29	1.07	1.48	0.56	0.55
FeOt	21.04	20.99	29.32	20.13	18.18
MnO	0.92	0.90	0.39	0.75	0.82
MgO	9.24	9.50	4.52	9.46	10.39
CaO	6.38	7.09	0.22	10.80	11.38
Na_2O	3.31	3.19	6.61	0.16	0.15
K_2O	0.85	0.79	0.25	0.13	0.06
Total	96.49	96.98	96.15	97.17	98.85
Normalization Scheme: 13-CNK					
Si (apfu)	7.625	7.608	7.953	8.000	8.000
Al	0.375	0.392	0.047	0.000	0.000
ΣT	*8.000*	*8.000*	*8.000*	*8.000*	*8.000*
Ti	0.018	0.018	0.042	0.006	0.005
Al	0.074	0.090	0.215	0.095	0.090
Fe^{3+}	1.196	1.173	1.705	1.101	1.488
Mn^{2+}	0.115	0.108	0.050	0.092	0.097
Fe^{2+}	2.598	2.689	1.976	1.343	0.636
Mg	0.999	0.922	1.012	2.046	2.163
ΣC	*5.000*	*5.000*	*5.000*	*4.683*	*4.479*
Ca	1.021	0.962	0.036	1.680	1.702
Na	0.873	1.013	1.924	0.046	0.040
ΣB	*1.894*	*1.975*	*1.960*	*1.726*	*1.742*
Na	-	-	-	0.000	0.000
K	0.153	0.157	0.048	0.023	0.110
ΣA	*0.153*	*0.157*	*0.048*	*0.023*	*0.110*
O (non-W)	22.000	22.000	22.000	22.000	22.000
W (OH)	2.000	2.000	2.000	2.000	2.000
Σ(T, C, B, A)	*15.047*	*15.132*	*15.008*	*14.432*	*14.331*
[(a)]Species	Wnc	Wnc	Rbk	Act	Act

* FeOt total iron reported as FeO; apfu: atoms per formula unit; bdl: below detection limit.

(a) IMA-2012 classification (Hawthorne et al., 2012), amphibole abbreviation follow Whitn

Transect-3								
				CO-42				
#11	#12	#1	#2	#5	6	#7	8	#17
52.03	52.11	53.36	53.36	52.87	54.02	52.47	53.71	52.80
0.31	0.18	0.10	0.09	0.07	0.09	0.09	0.00	0.07
1.74	2.13	1.29	1.07	1.29	0.84	1.29	0.96	1.30
30.33	30.35	21.04	20.99	21.94	20.45	21.93	21.71	21.72
0.30	0.38	0.92	0.90	0.97	1.00	0.87	0.95	0.78
4.33	4.08	9.24	9.50	8.87	9.82	8.89	8.89	8.50
0.71	0.52	6.38	7.09	6.33	8.08	6.51	7.12	7.08
6.00	6.03	3.31	3.19	3.59	2.70	3.24	3.14	3.55
0.32	0.29	0.85	0.79	0.93	0.76	1.09	1.17	0.88
96.06	96.06	96.49	96.98	96.86	97.75	96.38	97.66	96.68
7.830	7.827	7.964	7.957	7.915	8.000	7.896	8.000	7.993
0.170	0.173	0.036	0.043	0.085	0.000	0.104	0.000	0.007
8.000	*8.000*	*8.000*	*8.000*	*8.000*	*8.000*	*8.000*	*8.000*	*8.000*
0.035	0.021	0.012	0.010	0.008	0.010	0.010	0.001	0.008
0.139	0.205	0.190	0.145	0.142	0.146	0.125	0.169	0.224
1.922	1.950	0.663	0.539	0.677	0.385	0.709	0.492	0.258
0.038	0.048	0.117	0.113	0.123	0.126	0.111	0.119	0.100
1.895	1.863	1.963	2.079	2.070	2.148	2.052	2.212	2.491
0.972	0.914	2.055	2.113	1.980	2.168	1.995	1.975	1.919
5.001	*5.001*	*5.000*	*4.999*	*5.000*	*4.983*	*5.002*	*4.968*	*5.000*
0.114	0.083	1.019	1.133	1.016	*1.283*	1.049	*1.136*	1.149
1.751	1.755	0.959	0.867	0.984	*0.717*	0.945	*0.864*	0.851
1.865	*1.838*	*1.978*	*2.000*	*2.000*	*2.000*	*1.994*	*2.000*	*2.000*
-	-	-	0.055	0.057	*0.059*	-	*0.043*	0.191
0.061	0.055	0.162	0.151	0.177	*0.143*	0.208	*0.223*	0.170
0.061	*0.055*	*0.162*	*0.206*	*0.234*	*0.202*	*0.208*	*0.266*	*0.361*
22.000	22.000	22.000	22.000	22.000	22.000	22.000	22.000	22.000
2.000	2.000	2.000	2.000	2.000	2.000	2.000	2.000	2.000
14.927	*14.894*	*15.140*	*15.205*	*15.234*	*15.185*	*15.204*	*15.234*	*15.361*
Rbk	Rbk	Wnc	Wnc	Wnc	Wnc	Wnc	Wnc	Wnc

.

ey and Evans (2010): riebeckite (Rbk), winchite (Wnc), actinolite (Act).

#18

51.61
1.58
1.94
21.97
0.84
7.50
8.19
2.77
0.80
97.19

7.848
0.152
8.000

0.181
0.196
-
0.108
2.794
1.699
4.978

1.334
0.666
2.000

0.149
0.156
0.305

22.000
2.000
15.283

Wnc

Representaive EMPA and chemical formula of Titanite

Locality	Transect-1						
Sample	CO-24	CO-25		CO-38			
Analysis	#6	#22	#34	#6	#12	#13	#30
SiO_2 (wt%)	30.27	29.09	29.71	29.74	30.30	29.72	30.28
TiO_2	39.30	40.19	25.68	31.45	35.27	30.91	34.28
Al_2O_3	1.29	1.96	8.25	5.08	2.94	5.02	2.89
Fe_2O_3	0.69	0.95	6.70	2.54	1.39	2.11	2.37
Mn_2O_3	*bdl*	*bdl*	0.21	*bdl*	*bdl*	0.12	0.09
CaO	28.04	26.61	23.33	27.46	27.92	26.56	26.92
Total	100.76	100.04	94.70	97.28	98.98	95.40	97.87
Formula (5 Oxygens; Si = 1 apfu)							
Si (apfu)	1.000	1.000	1.000	1.000	1.000	1.000	1.000
Al	0.050	0.079	0.327	0.201	0.114	0.199	0.112
Ti	0.977	1.039	0.650	0.795	0.876	0.782	0.852
Fe^{3+}	0.017	0.025	0.170	0.064	0.035	0.054	0.059
Ca	0.993	0.980	0.841	0.989	0.987	0.958	0.952

* FeOt total iron reported as FeO; apfu: atoms per formula unit; bdl: below detection limit.

Transect-2							
CO-35							CO-36
#58	#59	#61	#64	#75	#79	#8	#3
31.83	30.58	30.72	30.30	29.21	31.10	31.12	30.29
26.37	29.71	27.34	28.44	32.83	29.43	27.82	36.51
5.68	4.20	6.53	5.68	6.00	4.70	6.76	2.62
4.84	4.15	3.08	2.99	4.83	3.98	3.14	0.39
0.17	0.07	*bdl*	*bdl*	*bdl*	*bdl*	*bdl*	*bdl*
26.79	28.62	27.90	28.16	22.72	27.69	28.35	27.50
96.55	98.21	96.41	96.43	96.57	97.85	98.04	98.38
1.000	1.000	1.000	1.000	1.000	1.000	1.000	1.000
0.210	0.162	0.251	0.221	0.242	0.178	0.256	0.102
0.623	0.731	0.669	0.706	0.846	0.712	0.672	0.906
0.114	0.102	0.075	0.074	0.124	0.096	0.076	0.010
0.902	1.003	0.973	0.996	0.834	0.954	0.976	0.973

Transect-3
CO-42
#60
27.78
30.15
4.40
7.07
0.06
23.88
94.22
1.000
0.187
0.816
0.191
0.921

Representative EMPA and chemical formulaa of Ilvaite

Locality	Transect-1 (Castirla)						
Sample	CO-38						
Analysis	#1	#2	#5	#7	#10	#20	#21
SiO_2 (wt%)	28.68	29.24	29.13	28.85	28.72	29.06	28.91
TiO_2	0.20	0.42	0.11	0.49	0.40	0.21	0.18
Al_2O_3	0.23	*bdl*	0.09	0.38	0.07	0.14	0.18
FeOt	49.06	48.73	49.59	48.40	49.82	48.74	48.08
MnO	2.86	3.02	3.11	2.90	2.97	2.67	2.77
MgO	0.18	0.11	0.14	0.25	0.11	0.16	0.16
CaO	13.54	13.68	13.50	13.20	13.51	13.87	13.52
Total	94.75	95.21	95.67	94.47	95.59	94.85	93.79
FeO	33.03	32.26	33.21	32.53	33.46	32.50	32.06
Fe_2O_3	17.82	18.30	18.21	17.64	18.18	18.05	17.81
Formula (8.5 Oxygens; Al + Fe^{3+} = 1 apfu)							
Si (apfu)	2.096	2.119	2.110	2.104	2.087	2.114	2.123
Al	0.020	-	0.008	0.032	0.006	0.012	0.016
Ti	0.011	0.023	0.006	0.027	0.022	0.012	0.010
Fe^{2+}	2.018	1.955	2.011	1.983	2.033	1.977	1.969
Fe^{3+}	0.980	0.998	0.992	0.968	0.994	0.988	0.984
Mn	0.177	0.185	0.191	0.179	0.183	0.165	0.172
Mg	0.019	0.012	0.015	0.027	0.012	0.017	0.017
Ca	1.060	1.062	1.047	1.031	1.052	1.081	1.064

* FeOt total iron reported as FeO; apfu: atoms per formula unit; bdl: below detection limit.

** Na_2O and K_2O always below detection limit.

Representative EMPA and chemical formula of Magnetite and Il

Locality	Transect-1 (Castirla)		
Sample	CO-38		
Analysis	#8	#9	#11
SiO_2 (wt%)	*bdl*	*bdl*	*bdl*
TiO_2	51.24	51.88	51.96
Al_2O_3	*bdl*	*bdl*	0.16
FeOt	39.50	38.45	37.09
MnO	7.90	7.90	8.06
MgO	0.03	0.03	0.03
Total	98.67	98.26	97.29
FeO	38.03	38.45	37.09
Fe_2O_3	1.64	-	-
Formula (3 cations)			
Si (apfu)	-	-	-
Ti	0.984	1.002	1.013
Al	-	-	0.005
Fe^{3+}	0.031	-	-
Fe^{2+}	0.812	0.825	0.804
Mn	0.171	0.172	0.177
Mg	0.001	0.001	0.001
Ca	-	-	-

* FeOt total iron reported as FeO; apfu: atoms per formula unit; bdl: below detection limit.

** CaO, BaO, Na_2O and K_2O always below detection limit.

Ilmenite

Supplementary Material#3 – T- Fe_2O_3 pseudosections calculated at 0.6 GPa for samples CO36 and CO42.

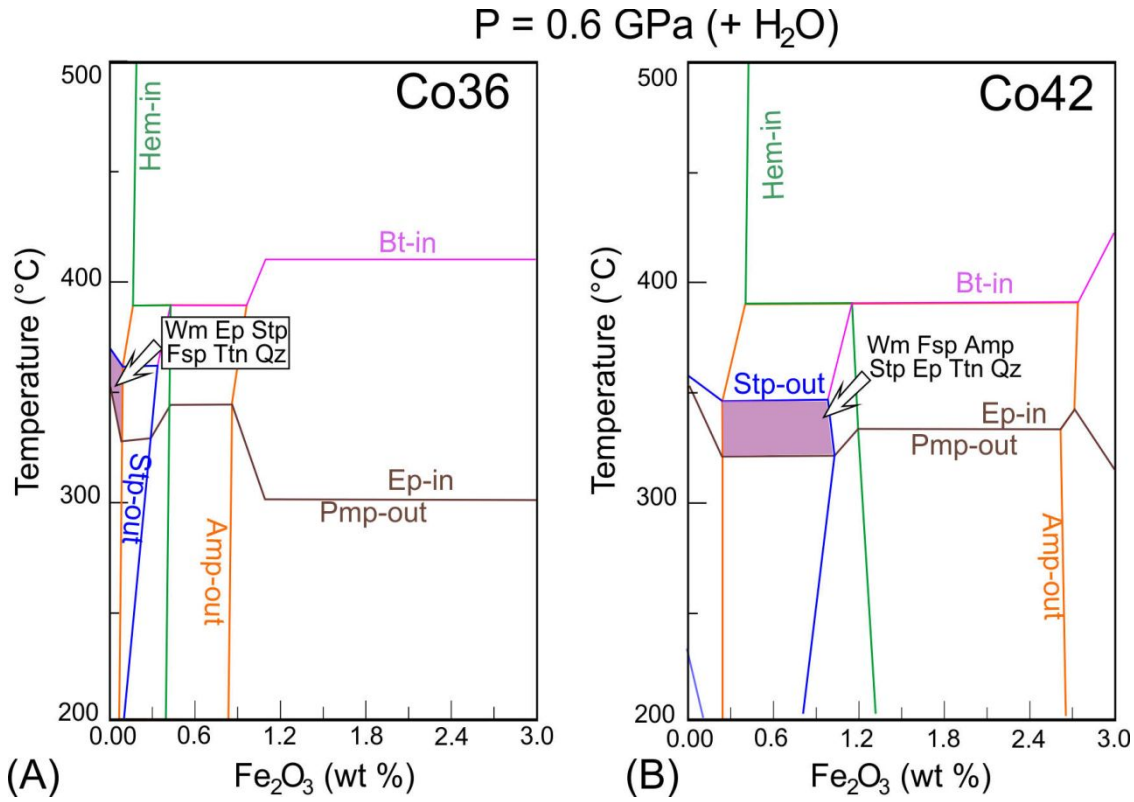

The FeO content (wt.%) is calculated as FeO = FeO(total) - (Fe_2O_3/1.11135) (wt.%). Accordingly, the surplus O_2 used in P-T pseudosection calculation (Table 2) is obtained as in Fe_2O_3 as O_2 = Fe_2O_3/(1.11125* 0.11135) = 0.100193 (rounded: 0.1).

Supplementary Material#4 - Ar-Ar in-situ data, Relative abundances.

	area	description	^{36}Ar	%1σ	^{37}Ar	%1σ	^{38}Ar	%1σ	^{39}Ar	%1σ	^{40}Ar	%1σ
	µm^2		[fA]		[fA]		[fA]		[fA]		[fA]	
CO24 (J = 0.00577542±0.00000347, ±1σ)												
101G	60x160	Wm	0.0104	10.5	0.0075	861	0.2189	15	14.633	0.10	55.885	0.059
101H	60x160	Wm	0.0097	8.9	0.0130	390	0.1031	36	7.697	0.16	34.085	0.082
101J	100x100	Wm	0.0039	15.5	0.0375	139	0.1043	25	13.451	0.11	50.104	0.053
101K	60x160	Wm	0.0011	56.6	0.0320	134	0.0528	59	9.463	0.15	35.398	0.076
101L	60x160	Wm	0.0015	43.7	0.0759	48	0.0887	32	10.623	0.12	39.979	0.084
101N	60x160	Wm	0.0016	41.7	0.0257	261	0.1591	16	13.896	0.10	52.904	0.063
101O	60x160	Wm	0.0053	12.0	0.0025	2540	0.1105	29	11.100	0.12	47.786	0.080
101P	100x100	Wm	0.0020	30.1	0.0073	956	0.1671	15	12.186	0.12	48.187	0.083
101R	60x160	Wm	0.0436	1.6	0.0485	118	0.1383	18	12.604	0.09	61.110	0.044
101S	100x100	Wm	0.1545	0.5	0.0159	362	0.2289	10	14.964	0.07	104.382	0.027
101T	60x160	Wm	0.0021	30.0	0.0716	81	0.1336	26	10.482	0.10	40.004	0.069
101V	100x100	K-Fsp?	0.0350	2.0	0.1165	43	0.0866	33	6.972	0.21	61.019	0.064
101W	100x100	Wm	0.0028	29.6	0.0065	925	0.1575	15	12.903	0.11	54.603	0.079
216B	~60x200	Wm	-0.0003	220.5	0.5996	40	0.1050	29	5.798	0.22	23.947	0.171
216H	100x100	Wm	0.0023	24.9	0.1543	177	0.0976	39	9.162	0.12	39.040	0.064
216I	60x160	Wm	0.0097	7.1	0.2530	104	0.1286	28	8.648	0.17	34.163	0.097
216K	60x160	Wm	0.0080	8.1	0.0690	486	0.1463	18	8.577	0.15	35.664	0.100
216L	60x160	Wm	0.0162	4.5	0.1332	185	0.1219	25	8.935	0.18	39.048	0.092
216O	60x160	K-Fsp?	-0.0023	34.2	-0.0274	1256	0.1141	28	6.724	0.21	38.658	0.073
216P	100x100	K-Fsp	-0.0050	13.8	0.0894	573	0.1247	28	7.355	0.20	32.865	0.083
216R	100x100	Wm	0.0063	9.4	0.1428	284	0.0775	38	6.523	0.20	28.071	0.105
216S	100x100	Wm	0.0044	15.1	0.1416	250	0.1354	21	8.366	0.11	34.699	0.086
216U	100x100	K-Fsp	0.0346	2.0	0.6038	37	0.1980	14	12.462	0.11	180.459	0.019
216V	100x100	Wm	0.0034	18.8	0.2614	133	0.0614	58	6.780	0.16	32.277	0.105
216X	60x160	Wm	-0.0011	47.2	0.1469	207	0.0977	39	6.894	0.24	33.065	0.112
216Y	100x100	Wm(±K-Fsp?)	-0.0008	71.9	0.1523	163	0.1430	27	11.750	0.15	53.590	0.072
216Z	100x100	K-Fsp?	0.0038	17.3	0.0604	556	0.1385	26	9.824	0.20	61.924	0.062
217E	~60x160	Wm	0.0073	9.4	0.1630	197	0.0597	49	6.385	0.32	26.029	0.164
217F	30x200	K-Fsp?	0.0119	4.7	0.5410	60	0.1071	31	6.470	0.25	36.422	0.090
217H	~100x100	K-Fsp?	0.0167	3.3	0.1919	238	0.1298	25	10.295	0.15	56.088	0.053
217I	~100x100	K-Fsp?	0.0177	3.2	0.4439	98	0.0256	137	6.442	0.17	36.572	0.076
217K	~160x50	K-Fsp?	0.0060	12.2	-0.0259	1217	0.0836	50	3.046	0.46	17.851	0.247
217L	100x100	K-Fsp	0.0079	8.6	-0.0883	389	0.0620	73	4.201	0.32	23.179	0.158
217N	100x100	Wm	0.0013	42.3	0.0985	388	0.1015	38	8.692	0.14	32.033	0.090
217O	50x200	Wm	0.0004	139.8	0.1916	142	0.0499	76	4.936	0.28	18.744	0.230
217T	~60x160	Wm	0.0124	4.8	0.0715	539	0.0962	32	7.087	0.25	29.908	0.121
217U	100x100	Wm	0.0134	3.3	0.3041	91	0.0923	37	7.628	0.21	33.299	0.114
217W	100x100	Wm	-0.0021	23.5	0.1228	291	0.0893	49	7.058	0.24	25.950	0.133
217X	100x100	Wm	0.0025	25.6	0.3170	77	0.1139	32	7.646	0.20	29.098	0.123
218A	100x100	Wm	0.0035	17.7	0.1586	164	0.0972	35	9.267	0.22	35.138	0.124
218B	100x100	Wm	0.0056	9.1	0.1440	288	0.0497	66	7.908	0.22	32.399	0.123
218D	100x100	Wm(±K-Fsp?)	0.0005	107.2	0.0919	391	0.0588	68	5.387	0.24	23.449	0.154
218E	100x100	Wm	0.0022	21.4	0.1230	147	0.0393	122	4.557	0.32	18.821	0.176
218G	~160*65	K-Fsp?	0.0066	12.0	0.2895	83	0.1157	32	6.498	0.26	36.830	0.108
218H	100x100	Wm	0.0058	12.5	0.1409	150	0.1206	31	9.227	0.23	37.782	0.091
218J	100x100	Wm	0.0013	46.9	0.3835	75	0.1239	34	6.618	0.20	25.482	0.115
218K	100x100	Wm	0.0044	14.2	0.3705	87	0.1203	27	7.774	0.16	32.940	0.111
218Q	60x160	Wm	0.0026	30.3	0.0399	898	0.0808	44	4.787	0.29	19.622	0.182
218R	100x100	Wm	0.0037	19.5	0.1152	202	0.0719	49	4.911	0.24	21.078	0.124

	area	description	^{36}Ar	%1σ	^{37}Ar	%1σ	^{38}Ar	%1σ	^{39}Ar	%1σ	^{40}Ar	%1σ
	µm^2		[fA]		[fA]		[fA]		[fA]		[fA]	
CO36 (J=0.00577996±0.00000231, ±1σ)												
84A	100x100	Wm	0.0134	5.0	0.3587	7.94	0.1940	15	17.584	0.1	63.060	0.04
84B	100x100	Wm	0.0048	13.1	0.0023	1203.51	0.0929	36	10.588	0.1	35.906	0.06
84C	100x100	Wm	0.0187	2.6	1.4755	2.33	0.2302	12	20.425	0.1	75.577	0.04
84E	~200x60	Wm	0.0166	4.1	0.5207	4.89	0.2463	11	20.071	0.1	67.299	0.04
84F	100x100	Wm	0.0169	4.7	0.2520	11.18	0.2752	11	23.560	0.1	81.973	0.04
84G	100x100	Wm	0.0214	3.3	0.7907	3.92	0.3375	8	25.376	0.0	93.870	0.03
84I	~100x100	Wm	0.0107	7.6	1.4448	2.09	0.1372	31	12.221	0.1	44.987	0.07
84J	60x60	Wm	0.0078	9.0	0.2672	11.14	0.0726	41	7.757	0.2	27.913	0.11
84N	100x100	Wm	0.0149	4.5	0.6922	3.15	0.2343	11	16.699	0.1	60.798	0.05
84O	200x60	Wm	0.0167	3.3	1.0071	2.49	0.3304	8	24.660	0.0	85.830	0.03
84Q	~200x60	Wm	0.0099	6.6	1.4072	2.21	0.2499	14	18.754	0.1	65.353	0.06
84R	~200x60	Wm	0.0117	5.6	0.4379	6.79	0.2106	15	18.463	0.1	62.959	0.05
84S	~100x100	Wm	0.0252	3.5	0.8151	3.18	0.2127	17	17.174	0.1	63.865	0.05
84U	~100x100	Wm	0.0192	2.5	0.8859	2.92	0.1727	16	19.197	0.1	69.682	0.04

84V	~100x100	Wm	0.0209	3.6	0.7972	3.85	0.2449	14	23.686	0.1	86.167	0.04
84W	~100x100	Wm	0.0393	1.9	1.3369	2.24	0.2774	10	26.452	0.0	98.845	0.04
84Z	~100x60	Wm	0.0440	1.6	0.8061	3.69	0.2281	10	17.634	0.1	70.748	0.05
85A	100x100	Wm	0.0072	9.8	0.2735	11.30	0.2199	13	16.303	0.1	54.146	0.06
85B	~300x30	Wm	0.0243	2.3	2.3917	1.32	0.2165	14	14.452	0.1	59.391	0.05
85G	~100x60	Wm	0.0161	4.0	1.6908	1.96	0.2177	12	19.086	0.1	69.024	0.04
85H	100x100	Wm	0.0145	4.9	1.1291	2.76	0.2809	8	23.229	0.1	82.663	0.04
85I	100x100	Wm	0.0181	2.9	0.2022	13.35	0.2641	11	24.008	0.1	84.997	0.03
85K	200x60	Wm	0.0234	4.1	2.8140	0.95	0.1650	19	13.863	0.1	53.078	0.05
85L	100x100	Wm	0.0139	5.5	2.6793	1.08	0.2473	11	24.051	0.1	82.528	0.04
85M	100x100	Wm	0.0209	3.4	1.2726	2.71	0.3257	9	29.053	0.1	104.047	0.03
85O	100x100	Wm	0.0355	2.0	3.2612	0.83	0.3183	15	25.368	0.0	93.080	0.04
85P	100x100	Wm	0.0159	4.5	3.0275	0.87	0.2636	16	17.783	0.1	64.088	0.05
85Q	100x100	Wm	0.0140	4.5	3.8033	0.67	0.2093	22	14.507	0.1	54.935	0.07
235A	160x60	Wm	0.0036	20.9	0.6046	105.33	0.0373	75	2.770	0.6	12.478	0.21
235C	100x100	Wm	0.0104	5.1	1.6528	26.06	0.1515	27	9.764	0.1	35.847	0.09
235D	100x100	Wm	0.0050	11.3	0.5859	73.28	0.1017	35	9.451	0.1	32.961	0.09
235F	100x100	Wm	0.0108	5.8	1.6621	36.61	0.2250	14	14.618	0.1	49.690	0.06
235G	100x100	Wm	0.0129	5.3	0.7949	75.97	0.2720	11	18.580	0.1	66.484	0.04
235I	100x100	Wm	0.0186	2.9	0.9965	33.30	0.2481	12	18.096	0.1	66.907	0.06
235J	~200x60	Wm	0.0178	2.5	0.8791	37.38	0.1290	21	9.783	0.1	38.829	0.08
235O	100x100	Wm	0.0049	12.8	0.2563	262.88	0.1599	19	9.126	0.1	30.332	0.11
235P	100x100	Wm	0.0099	6.4	0.1753	335.10	0.2310	15	17.391	0.1	59.851	0.05
235R	100x100	Wm	0.0214	3.4	0.1201	422.30	0.0372	101	0.157	7.9	6.897	0.32
235S	100x100	Wm	0.0275	2.2	1.9890	24.27	0.1611	22	15.192	0.1	58.001	0.06
235U	100x100	Wm	0.0282	2.4	1.2144	49.58	0.2712	13	23.625	0.1	84.561	0.04
235V	200x50	Wm	0.0198	2.8	0.8121	76.57	0.1356	30	11.237	0.1	43.548	0.08
235X	200x50	Wm	0.0520	1.3	1.3289	25.64	0.2993	9	20.704	0.1	84.820	0.04
235Y	100x100	Wm	0.0054	9.4	0.1872	325.50	0.0968	29	6.058	0.2	23.266	0.14

	area	description	^{36}Ar	%1σ	^{37}Ar	%1σ	^{38}Ar	%1σ	^{39}Ar	%1σ	^{40}Ar	%1σ
	µm²		[fA]		[fA]		[fA]		[fA]		[fA]	
CO42 (J=0.00577784±0.00000347, ±1σ)												
91A	100x100	Wm	0.0050	12.4	0.0253	111.68	0.1883	20	12.285	0.1	52.292	0.07
91B	100x100	Wm	0.0087	6.9	0.0177	218.10	0.1802	18	11.981	0.1	51.621	0.09
91P	100x100	Wm	0.0006	141.5	0.0202	146.70	0.1956	21	17.353	0.1	68.167	0.06
91Q	100x100	Wm	0.0038	17.7	0.0720	40.06	0.1327	32	13.068	0.1	52.542	0.07
91S	100x100	Wm	0.0063	11.6	0.0386	92.68	0.0911	31	7.044	0.2	29.189	0.13
91T	100x100	Wm	0.0069	10.5	0.1198	29.82	0.2628	7	21.568	0.1	87.459	0.04
91U	100x100	Wm	0.0167	3.7	0.6444	6.73	0.0648	39	7.098	0.2	34.419	0.11
91W	100x100	Wm	0.0020	33.8	0.1960	22.08	0.2105	13	18.824	0.1	75.504	0.04
91X	100x100	Wm	0.0028	20.2	0.0293	99.99	0.2388	16	21.127	0.1	82.518	0.04
91Y	100x100	Wm	0.0028	21.0	0.0090	400.12	0.2143	12	17.441	0.1	76.909	0.04
92A	100x100	Wm	0.0058	11.0	0.1488	24.06	0.2340	16	15.338	0.1	62.175	0.06
92B	50x50	Wm	0.0018	39.3	-0.0020	2102.11	0.0960	27	7.453	0.2	34.365	0.10
92C	50x50	Wm	0.0028	25.3	0.0346	109.15	0.0844	38	4.988	0.3	27.586	0.14
92I	50x50	Wm	0.0005	147.8	0.0858	41.07	0.1262	32	6.193	0.2	24.261	0.14
92J	100x100	Wm	0.0046	13.6	0.8148	5.25	0.0816	56	6.274	0.2	28.407	0.11
92K	100x100	Wm	0.0065	11.0	0.0919	33.62	0.1593	29	8.537	0.2	35.208	0.11
92M	100x100	Wm	0.0017	36.6	0.0800	36.18	0.1154	22	13.248	0.1	74.278	0.03
92N	100x100	Wm	0.0061	11.7	0.1307	27.37	0.0170	160	8.739	0.2	35.247	0.10
92O	100x100	Wm	0.0048	14.2	0.0321	110.57	0.1256	22	14.483	0.1	58.274	0.05
92Q	100x100	Wm	0.0047	13.5	0.0426	68.20	0.1748	31	9.652	0.1	38.599	0.08
92R	~100x60	Wm	0.0159	2.9	0.0242	118.97	0.0532	101	5.331	0.3	28.624	0.10
233C	100x100	Wm	0.0006	110.1	0.3107	152.53	0.0480	105	3.539	0.4	17.350	0.38
233D	100x100	Wm	0.0055	12.7	0.1102	479.74	0.0682	67	4.297	0.3	18.146	0.26
233F	100x100	Wm	0.0070	9.0	0.4934	84.09	0.1544	16	10.329	0.2	46.358	0.11
233G	100x100	Wm	0.0136	4.6	0.8773	48.81	0.0916	33	7.477	0.2	33.030	0.13
233I	100x100	K-Fsp?	0.0088	7.7	0.2768	133.51	0.0498	117	3.924	0.3	25.830	0.16
233J	100x100	Wm	0.0020	36.5	0.1174	293.60	0.1624	37	11.871	0.1	56.194	0.07
233M	100x100	Pl	0.0095	6.4	0.4393	104.78	0.0293	120	0.061	22.5	4.676	0.71
233N	100x100	Wm	0.0048	12.2	0.0122	4607.78	0.1102	30	8.777	0.1	33.918	0.10
233Q	~200x65	Wm	0.0121	6.8	0.4346	134.25	0.1012	30	5.969	0.2	27.104	0.15
233R	100x100	Wm	0.0033	19.1	0.7987	66.68	0.2088	14	16.404	0.1	87.185	0.04
233T	100x100	Wm	0.0037	19.5	-0.4818	147.98	0.1890	16	16.672	0.1	70.385	0.04
233V	100x100	Wm	0.0017	44.8	-0.2066	306.22	0.1713	21	12.596	0.1	48.634	0.06
233X	100x100	Wm	0.0039	16.5	0.3795	198.79	0.0960	30	7.591	0.1	30.554	0.14
233Y	100x100	Wm	0.0024	19.3	0.1122	691.54	0.1275	22	8.286	0.2	32.666	0.12
234A	100x100	Wm	0.0037	15.6	0.3115	196.46	0.1691	28	15.054	0.1	59.392	0.06
234B	~100x100	Wm	0.0085	9.1	0.3768	169.12	0.2299	22	20.868	0.1	85.339	0.04
234H	100x100	Wm	0.0005	161.6	0.3347	217.40	0.1527	27	9.937	0.2	38.595	0.09
234I	100x100	Wm	0.0094	7.1	0.3371	153.37	0.2474	17	17.916	0.1	86.906	0.05
234K	160x60	K-Fsp?	-0.0011	64.4	0.5661	113.63	0.0066	775	1.747	0.9	11.537	0.33

Decay Constant 40K = 5.463 ± 0.214 E-10 1/a
Decay Constant 39Ar = 2.940 ± 0.016 E-07 1/h
Decay Constant 37Ar = 8.230 ± 0.012 E-04 1/h

Atmospheric Ratio 40/36(a) = 298.56 ± 0.30
Atmospheric Ratio 38/36(a) = 0.1869 ± 0.0003

Production Ratio 39/37(ca) = 0.000696 ± 0.000015
Production Ratio 38/37(ca) = 0.000058 ± 0.000005
Production Ratio 36/37(ca) = 0.000269 ± 0.000005
Production Ratio 40/39(k) = 0.00973 ± 0.00012
Production Ratio 38/39(k) = 0.01265 ± 0.00014

$^{40}Ar^*/^{39}Ar_{(K)}$	±2σ	Age (Ma)	±2σ	$^{40}Ar^*$ (%)	$^{39}Ar_{(K)}$ (%)	K/Ca	±2σ
3.5978	0.0453	**37.64**	**0.47**	94.2	3.5	1037	17864
4.0420	0.0685	**42.24**	**0.71**	91.3	1.9	313	2440
3.6285	0.0282	**37.96**	**0.29**	97.4	3.2	190	530
3.6980	0.0399	**38.68**	**0.41**	98.9	2.3	157	421
3.7133	0.0373	**38.84**	**0.39**	98.7	2.6	74	72
3.7631	0.0302	**39.36**	**0.31**	98.8	3.3	287	1499
4.1527	0.0363	**43.38**	**0.37**	96.5	2.7	2330	118378
3.8946	0.0322	**40.71**	**0.33**	98.5	2.9	881	16831
3.8071	0.0339	**39.81**	**0.35**	78.5	3.0	138	325
3.8828	0.0343	**40.59**	**0.36**	55.7	3.6	498	3598
3.7483	0.0366	**39.20**	**0.38**	98.2	2.5	78	125
7.2462	0.0686	**75.03**	**0.70**	82.8	1.7	32	27
4.1568	0.0402	**43.42**	**0.42**	98.2	3.1	1045	19342
4.1453	0.0738	**43.31**	**0.76**	100.4	1.4	5	4
4.1774	0.0396	**43.64**	**0.41**	98.0	2.2	31	112
3.6080	0.0499	**37.75**	**0.52**	91.3	2.1	18	38
3.8715	0.0478	**40.48**	**0.49**	93.1	2.1	66	641
3.8192	0.0518	**39.94**	**0.54**	87.4	2.2	36	132
5.8428	0.0758	**60.74**	**0.78**	101.6	1.6	-130	3264
4.6632	0.0607	**48.64**	**0.62**	104.4	1.8	44	500
4.0060	0.0580	**41.87**	**0.60**	93.1	1.6	24	138
3.9829	0.0491	**41.63**	**0.51**	96.0	2.0	31	156
13.6460	0.0459	**138.81**	**0.45**	94.2	3.0	11	8
4.6045	0.0596	**48.04**	**0.61**	96.7	1.6	14	37
4.8368	0.0529	**50.43**	**0.54**	100.8	1.7	25	103
4.5725	0.0332	**47.71**	**0.34**	100.3	2.8	41	133
6.1780	0.0483	**64.17**	**0.49**	98.0	2.4	86	958
3.7271	0.0702	**38.98**	**0.73**	91.4	1.5	21	82
5.0767	0.0585	**52.89**	**0.60**	90.2	1.6	6	8
4.9551	0.0363	**51.64**	**0.37**	90.9	2.5	28	135
4.8521	0.0563	**50.59**	**0.58**	85.5	1.5	8	15
5.2667	0.1541	**54.84**	**1.58**	89.9	0.7	-62	1518
4.9483	0.1040	**51.57**	**1.07**	89.7	1.0	-25	196
3.6311	0.0411	**37.99**	**0.43**	98.5	2.1	47	363
3.7664	0.0754	**39.39**	**0.78**	99.2	1.2	14	39
3.6870	0.0548	**38.57**	**0.57**	87.4	1.7	53	567
3.8325	0.0404	**40.07**	**0.42**	87.8	1.8	13	24
3.7559	0.0467	**39.28**	**0.48**	102.2	1.7	30	177
3.7002	0.0541	**38.70**	**0.56**	97.2	1.8	13	20
3.6708	0.0442	**38.40**	**0.46**	96.8	2.2	31	102
3.8783	0.0440	**40.55**	**0.45**	94.7	1.9	29	167
4.3172	0.0638	**45.08**	**0.66**	99.2	1.3	31	243
3.9760	0.0695	**41.56**	**0.72**	96.3	1.1	20	58
5.3576	0.0793	**55.78**	**0.81**	94.5	1.6	12	20
3.8977	0.0513	**40.75**	**0.53**	95.2	2.2	35	104
3.7868	0.0588	**39.60**	**0.61**	98.3	1.6	9	14
4.0630	0.0507	**42.46**	**0.52**	95.9	1.9	11	19
3.9310	0.1014	**41.09**	**1.05**	95.9	1.2	64	1142
4.0626	0.0899	**42.45**	**0.93**	94.6	1.2	23	91

$^{40}Ar^*/^{39}Ar_{(K)}$	±2σ	Age (Ma)	±2σ	$^{40}Ar^*$ (%)	$^{39}Ar_{(K)}$ (%)	K/Ca	±2σ
3.35	0.02	**35.12**	**0.25**	93.5	2.4	26.0	4.9
3.25	0.04	**34.03**	**0.38**	95.7	1.5	2490	59933
3.42	0.02	**35.87**	**0.16**	92.5	2.8	7.34	0.81
3.10	0.02	**32.50**	**0.22**	92.4	2.8	20.4	2.9
3.26	0.02	**34.13**	**0.22**	93.6	3.2	50	12
3.44	0.02	**36.04**	**0.18**	93.0	3.5	17.0	2.2
3.42	0.04	**35.84**	**0.43**	92.9	1.7	4.48	0.49
3.29	0.06	**34.51**	**0.58**	91.5	1.1	15.4	3.8
3.37	0.02	**35.28**	**0.26**	92.5	2.3	12.8	1.5
3.27	0.01	**34.29**	**0.15**	94.0	3.4	13.0	1.5
3.32	0.02	**34.83**	**0.22**	95.4	2.6	7.06	0.77
3.21	0.02	**33.68**	**0.23**	94.2	2.5	22.3	3.8
3.27	0.03	**34.32**	**0.32**	88.0	2.4	11.2	1.3
3.33	0.02	**34.85**	**0.17**	91.6	2.6	11.5	1.3

3.37	0.02	**35.29**	**0.20**	92.6	3.3	15.7	2.0
3.29	0.02	**34.45**	**0.18**	88.0	3.6	10.5	1.1
3.26	0.02	**34.19**	**0.26**	81.3	2.4	11.6	1.4
3.18	0.03	**33.35**	**0.28**	95.8	2.2	31.6	7.8
3.61	0.02	**37.81**	**0.26**	87.8	2.0	3.20	0.33
3.36	0.02	**35.22**	**0.22**	92.9	2.6	5.98	0.64
3.37	0.02	**35.27**	**0.20**	94.6	3.2	10.9	1.2
3.31	0.01	**34.65**	**0.15**	93.4	3.3	63	18
3.33	0.04	**34.91**	**0.44**	87.0	1.9	2.61	0.27
3.26	0.02	**34.15**	**0.20**	94.9	3.3	4.76	0.49
3.36	0.02	**35.22**	**0.16**	93.8	4.0	12.1	1.4
3.25	0.02	**34.09**	**0.18**	88.6	3.5	4.12	0.42
3.34	0.02	**35.02**	**0.26**	92.7	2.4	3.11	0.32
3.51	0.03	**36.78**	**0.28**	92.7	2.0	2.02	0.20
4.13	0.17	**43.16**	**1.79**	91.6	0.4	2.4	5.1
3.36	0.03	**35.20**	**0.36**	91.5	1.3	3.1	1.7
3.32	0.04	**34.84**	**0.40**	95.3	1.3	8.5	12.6
3.18	0.03	**33.33**	**0.29**	93.5	2.0	4.7	3.4
3.36	0.02	**35.26**	**0.24**	94.0	2.6	12	19
3.39	0.02	**35.47**	**0.20**	91.6	2.5	9.6	6.5
3.42	0.03	**35.86**	**0.31**	86.2	1.3	5.9	4.4
3.15	0.04	**33.08**	**0.46**	94.9	1.3	19	99
3.26	0.02	**34.19**	**0.24**	94.8	2.4	53	352
3.34	2.85	**35.03**	**29.63**	7.6	0.0	0.7	5.9
3.28	0.03	**34.36**	**0.27**	85.9	2.1	4.0	2.0
3.22	0.02	**33.73**	**0.19**	89.9	3.2	10.3	10.3
3.35	0.03	**35.07**	**0.33**	86.4	1.5	7.3	11.3
3.34	0.02	**35.02**	**0.21**	81.6	2.8	8.3	4.3
3.57	0.06	**37.33**	**0.58**	92.8	0.8	17	112

$^{40}Ar^*/^{39}Ar_{(K)}$	±2σ	**Age (Ma)**	**±2σ**	$^{40}Ar^*$ (%)	$^{39}Ar_{(K)}$ (%)	K/Ca	±2σ
4.13	0.03	**43.12**	**0.33**	96.9	2.8	257	576
4.08	0.03	**42.68**	**0.34**	94.8	2.8	359	1568
3.91	0.03	**40.88**	**0.30**	99.5	4.0	455	1335
3.92	0.03	**41.05**	**0.33**	97.6	3.0	96	78
3.87	0.07	**40.45**	**0.67**	93.3	1.6	97	179
3.95	0.02	**41.30**	**0.22**	97.4	5.0	95	58
4.15	0.06	**43.32**	**0.57**	85.5	1.6	5.8	1.0
3.97	0.02	**41.52**	**0.23**	99.0	4.4	51	23
3.86	0.02	**40.34**	**0.18**	98.7	4.9	382	764
4.35	0.02	**45.46**	**0.22**	98.7	4.0	1021	8175
3.93	0.03	**41.12**	**0.27**	97.0	3.6	55	27
4.53	0.06	**47.28**	**0.62**	98.2	1.7	-1978	83151
5.36	0.09	**55.78**	**0.93**	96.8	1.2	76	167
3.88	0.08	**40.62**	**0.80**	99.1	1.4	38	32
4.31	0.06	**45.04**	**0.65**	95.2	1.5	4.08	0.59
3.89	0.05	**40.67**	**0.54**	94.3	2.0	49	33
5.56	0.03	**57.87**	**0.31**	99.2	3.1	88	64
3.82	0.05	**39.94**	**0.52**	94.7	2.0	35	20
3.92	0.03	**40.94**	**0.31**	97.3	3.4	239	529
3.84	0.04	**40.20**	**0.42**	96.1	2.2	120	164
4.47	0.06	**46.68**	**0.60**	83.3	1.2	117	277
4.85	0.12	**50.60**	**1.24**	99.0	0.8	6	18
3.83	0.10	**40.09**	**1.08**	90.8	1.0	21	198
4.28	0.04	**44.72**	**0.42**	95.4	2.4	11	19
3.88	0.05	**40.54**	**0.57**	87.7	1.7	4.5	4.4
5.91	0.11	**61.45**	**1.16**	89.8	0.9	8	20
4.68	0.04	**48.79**	**0.40**	98.8	2.8	54	315
31.22	15.41	**303.34**	**137.81**	40.3	0.0	0.07	0.16
3.69	0.04	**38.62**	**0.45**	95.5	2.0	383	35263
3.93	0.09	**41.10**	**0.90**	86.5	1.4	7	20
5.25	0.03	**54.69**	**0.27**	98.8	3.8	11	15
4.14	0.03	**43.30**	**0.29**	98.1	3.9	-18	54
3.81	0.04	**39.86**	**0.39**	98.7	2.9	-32	198
3.87	0.05	**40.45**	**0.56**	96.1	1.8	11	42
3.85	0.04	**40.25**	**0.41**	97.6	1.9	39	541
3.86	0.03	**40.42**	**0.26**	97.9	3.5	26	101
3.96	0.02	**41.40**	**0.24**	96.8	4.8	29	99
3.86	0.05	**40.41**	**0.49**	99.5	2.3	16	68
4.69	0.02	**48.90**	**0.26**	96.6	4.2	28	86
6.81	0.28	**70.62**	**2.84**	103.1	0.4	1.6	3.7

Table SM 1. Ar-Ar in-situ data. Relative abundances.

	area	description	^{36}Ar	%1σ	^{37}Ar	%1σ	^{38}Ar	%1σ	^{39}Ar	%1σ	^{40}Ar	%1σ
	µm^2		[fA]		[fA]		[fA]		[fA]		[fA]	
CO24 (J = 0.00577542±0.00000347, ±1σ)												
101G	60x160	WM	0.0104	10.5	0.0075	861	0.2189	15	14.633	0.10	55.885	0.059
101H	60x160	WM	0.0097	8.9	0.0130	390	0.1031	36	7.697	0.16	34.085	0.082
101J	100x100	WM	0.0039	15.5	0.0375	139	0.1043	25	13.451	0.11	50.104	0.053
101K	60x160	WM	0.0011	56.6	0.0320	134	0.0528	59	9.463	0.15	35.398	0.076
101L	60x160	WM	0.0015	43.7	0.0759	48	0.0887	32	10.623	0.12	39.979	0.084
101N	60x160	WM	0.0016	41.7	0.0257	261	0.1591	16	13.896	0.10	52.904	0.063
101O	60x160	WM	0.0053	12.0	0.0025	2540	0.1105	29	11.100	0.12	47.786	0.080
101P	100x100	WM	0.0020	30.1	0.0073	956	0.1671	15	12.186	0.12	48.187	0.083
101R	60x160	WM	0.0436	1.6	0.0485	118	0.1383	18	12.604	0.09	61.110	0.044
101S	100x100	WM	0.1545	0.5	0.0159	362	0.2289	10	14.964	0.07	104.382	0.027
101T	60x160	WM	0.0021	30.0	0.0716	81	0.1336	26	10.482	0.10	40.004	0.069
101V	100x100	Kfs?	0.0350	2.0	0.1165	43	0.0866	33	6.972	0.21	61.019	0.064
101W	100x100	WM	0.0028	29.6	0.0065	925	0.1575	15	12.903	0.11	54.603	0.079
216B	~60x200	WM	-0.0003	220.5	0.5996	40	0.1050	29	5.798	0.22	23.947	0.171
216H	100x100	WM	0.0023	24.9	0.1543	177	0.0976	39	9.162	0.12	39.040	0.064
216I	60x160	WM	0.0097	7.1	0.2530	104	0.1286	28	8.648	0.17	34.163	0.097
216K	60x160	WM	0.0080	8.1	0.0690	486	0.1463	18	8.577	0.15	35.664	0.100
216L	60x160	WM	0.0162	4.5	0.1332	185	0.1219	25	8.935	0.18	39.048	0.092
216O	60x160	Kfs?	-0.0023	34.2	-0.0274	1256	0.1141	28	6.724	0.21	38.658	0.073
216P	100x100	WM(±Kfs?)	-0.0050	13.8	0.0894	573	0.1247	28	7.355	0.20	32.865	0.083
216R	100x100	WM	0.0063	9.4	0.1428	284	0.0775	38	6.523	0.20	28.071	0.105
216S	100x100	WM	0.0044	15.1	0.1416	250	0.1354	21	8.366	0.11	34.699	0.086
216U	100x100	Kfs	0.0346	2.0	0.6038	37	0.1980	14	12.462	0.11	180.459	0.019
216V	100x100	WM	0.0034	18.8	0.2614	133	0.0614	58	6.780	0.16	32.277	0.105
216X	60x160	WM	-0.0011	47.2	0.1469	207	0.0977	39	6.894	0.24	33.065	0.112
216Y	100x100	WM(±Kfs?)	-0.0008	71.9	0.1523	163	0.1430	27	11.750	0.15	53.590	0.072
216Z	100x100	Kfs?	0.0038	17.3	0.0604	556	0.1385	26	9.824	0.20	61.924	0.062
217E	~60x160	WM	0.0073	9.4	0.1630	197	0.0597	49	6.385	0.32	26.029	0.164
217F	30x200	Kfs?	0.0119	4.7	0.5410	60	0.1071	31	6.470	0.25	36.422	0.090
217H	~100x100	Kfs?	0.0167	3.3	0.1919	238	0.1298	25	10.295	0.15	56.088	0.053
217I	~100x100	Kfs?	0.0177	3.2	0.4439	98	0.0256	137	6.442	0.17	36.572	0.076
217K	~160x50	Kfs?	0.0060	12.2	-0.0259	1217	0.0836	50	3.046	0.46	17.851	0.247
217L	100x100	Kfs	0.0079	8.6	-0.0883	389	0.0620	73	4.201	0.32	23.179	0.158
217N	100x100	WM	0.0013	42.3	0.0985	388	0.1015	38	8.692	0.14	32.033	0.090
217O	50x200	WM	0.0004	139.8	0.1916	142	0.0499	76	4.936	0.28	18.744	0.230
217T	~60x160	WM	0.0124	4.8	0.0715	539	0.0962	32	7.087	0.25	29.908	0.121
217U	100x100	WM	0.0134	3.3	0.3041	91	0.0923	37	7.628	0.21	33.299	0.114
217W	100x100	WM	-0.0021	23.5	0.1228	291	0.0893	49	7.058	0.24	25.950	0.133
217X	100x100	WM	0.0025	25.6	0.3170	77	0.1139	32	7.646	0.20	29.098	0.123
218A	100x100	WM	0.0035	17.7	0.1586	164	0.0972	35	9.267	0.22	35.138	0.124
218B	100x100	WM	0.0056	9.1	0.1440	288	0.0497	66	7.908	0.22	32.399	0.123
218D	100x100	WM(±Kfs?)	0.0005	107.2	0.0919	391	0.0588	68	5.387	0.24	23.449	0.154
218E	100x100	WM	0.0022	21.4	0.1230	147	0.0393	122	4.557	0.32	18.821	0.176
218G	~160*65	Kfs?	0.0066	12.0	0.2895	83	0.1157	32	6.498	0.26	36.830	0.108
218H	100x100	WM	0.0058	12.5	0.1409	150	0.1206	31	9.227	0.23	37.782	0.091
218J	100x100	WM	0.0013	46.9	0.3835	75	0.1239	34	6.618	0.20	25.482	0.115
218K	100x100	WM	0.0044	14.2	0.3705	87	0.1203	27	7.774	0.16	32.940	0.111
218Q	60x160	WM	0.0026	30.3	0.0399	898	0.0808	44	4.787	0.29	19.622	0.182
218R	100x100	WM	0.0037	19.5	0.1152	202	0.0719	49	4.911	0.24	21.078	0.124

	area	description	^{36}Ar	%1σ	^{37}Ar	%1σ	^{38}Ar	%1σ	^{39}Ar	%1σ	^{40}Ar	%1σ
	µm^2		[fA]		[fA]		[fA]		[fA]		[fA]	
CO36 (J=0.00577996±0.00000231, ±1σ)												
84A	100x100	WM	0.0134	5.0	0.3587	7.94	0.1940	15	17.584	0.1	63.060	0.04
84B	100x100	WM	0.0048	13.1	0.0023	1203.51	0.0929	36	10.588	0.1	35.906	0.06
84C	100x100	WM	0.0187	2.6	1.4755	2.33	0.2302	12	20.425	0.1	75.577	0.04
84E	~200x60	WM	0.0166	4.1	0.5207	4.89	0.2463	11	20.071	0.1	67.299	0.04
84F	100x100	WM	0.0169	4.7	0.2520	11.18	0.2752	11	23.560	0.1	81.973	0.04
84G	100x100	WM	0.0214	3.3	0.7907	3.92	0.3375	8	25.376	0.0	93.870	0.03
84I	~100x100	WM	0.0107	7.6	1.4448	2.09	0.1372	31	12.221	0.1	44.987	0.07
84J	60x60	WM	0.0078	9.0	0.2672	11.14	0.0726	41	7.757	0.2	27.913	0.11
84N	100x100	WM	0.0149	4.5	0.6922	3.15	0.2343	11	16.699	0.1	60.798	0.05
84O	200x60	WM	0.0167	3.3	1.0071	2.49	0.3304	8	24.660	0.0	85.830	0.03
84Q	~200x60	WM	0.0099	6.6	1.4072	2.21	0.2499	14	18.754	0.1	65.353	0.06
84R	~200x60	WM	0.0117	5.6	0.4379	6.79	0.2106	15	18.463	0.1	62.959	0.05
84S	~100x100	WM	0.0252	3.5	0.8151	3.18	0.2127	17	17.174	0.1	63.865	0.05
84U	~100x100	WM	0.0192	2.5	0.8859	2.92	0.1727	16	19.197	0.1	69.682	0.04

84V	~100x100	WM	0.0209	3.6	0.7972	3.85	0.2449	14	23.686	0.1	86.167	0.04
84W	~100x100	WM	0.0393	1.9	1.3369	2.24	0.2774	10	26.452	0.0	98.845	0.04
84Z	~100x60	WM	0.0440	1.6	0.8061	3.69	0.2281	10	17.634	0.1	70.748	0.05
85A	100x100	WM	0.0072	9.8	0.2735	11.30	0.2199	13	16.303	0.1	54.146	0.06
85B	~300x30	WM	0.0243	2.3	2.3917	1.32	0.2165	14	14.452	0.1	59.391	0.05
85G	~100x60	WM	0.0161	4.0	1.6908	1.96	0.2177	12	19.086	0.1	69.024	0.04
85H	100x100	WM	0.0145	4.9	1.1291	2.76	0.2809	8	23.229	0.1	82.663	0.04
85I	100x100	WM	0.0181	2.9	0.2022	13.35	0.2641	11	24.008	0.1	84.997	0.03
85K	200x60	WM	0.0234	4.1	2.8140	0.95	0.1650	19	13.863	0.1	53.078	0.05
85L	100x100	WM	0.0139	5.5	2.6793	1.08	0.2473	11	24.051	0.1	82.528	0.04
85M	100x100	WM	0.0209	3.4	1.2726	2.71	0.3257	9	29.053	0.1	104.047	0.03
85O	100x100	WM	0.0355	2.0	3.2612	0.83	0.3183	15	25.368	0.0	93.080	0.04
85P	100x100	WM	0.0159	4.5	3.0275	0.87	0.2636	16	17.783	0.1	64.088	0.05
85Q	100x100	WM	0.0140	4.5	3.8033	0.67	0.2093	22	14.507	0.1	54.935	0.07
235A	160x60	WM	0.0036	20.9	0.6046	105.33	0.0373	75	2.770	0.6	12.478	0.21
235C	100x100	WM	0.0104	5.1	1.6528	26.06	0.1515	27	9.764	0.1	35.847	0.09
235D	100x100	WM	0.0050	11.3	0.5859	73.28	0.1017	35	9.451	0.1	32.961	0.09
235F	100x100	WM	0.0108	5.8	1.6621	36.61	0.2250	14	14.618	0.1	49.690	0.06
235G	100x100	WM	0.0129	5.3	0.7949	75.97	0.2720	11	18.580	0.1	66.484	0.04
235I	100x100	WM	0.0186	2.9	0.9965	33.30	0.2481	12	18.096	0.1	66.907	0.06
235J	~200x60	WM	0.0178	2.5	0.8791	37.38	0.1290	21	9.783	0.1	38.829	0.08
235O	100x100	WM	0.0049	12.8	0.2563	262.88	0.1599	19	9.126	0.1	30.332	0.11
235P	100x100	WM	0.0099	6.4	0.1753	335.10	0.2310	15	17.391	0.1	59.851	0.05
235R	100x100	WM	0.0214	3.4	0.1201	422.30	0.0372	101	0.157	7.9	6.897	0.32
235S	100x100	WM	0.0275	2.2	1.9890	24.27	0.1611	22	15.192	0.1	58.001	0.06
235U	100x100	WM	0.0282	2.4	1.2144	49.58	0.2712	13	23.625	0.1	84.561	0.04
235V	200x50	WM	0.0198	2.8	0.8121	76.57	0.1356	30	11.237	0.1	43.548	0.08
235X	200x50	WM	0.0520	1.3	1.3289	25.64	0.2993	9	20.704	0.1	84.820	0.04
235Y	100x100	WM	0.0054	9.4	0.1872	325.50	0.0968	29	6.058	0.2	23.266	0.14

	area	description	^{36}Ar	%1σ	^{37}Ar	%1σ	^{38}Ar	%1σ	^{39}Ar	%1σ	^{40}Ar	%1σ
	µm²		[fA]		[fA]		[fA]		[fA]		[fA]	
CO42 (J=0.00577784±0.00000347, ±1σ)												
91A	100x100	WM	0.0050	12.4	0.0253	111.68	0.1883	20	12.285	0.1	52.292	0.07
91B	100x100	WM	0.0087	6.9	0.0177	218.10	0.1802	18	11.981	0.1	51.621	0.09
91P	100x100	WM	0.0006	141.5	0.0202	146.70	0.1956	21	17.353	0.1	68.167	0.06
91Q	100x100	WM	0.0038	17.7	0.0720	40.06	0.1327	32	13.068	0.1	52.542	0.07
91S	100x100	WM	0.0063	11.6	0.0386	92.68	0.0911	31	7.044	0.2	29.189	0.13
91T	100x100	WM	0.0069	10.5	0.1198	29.82	0.2628	7	21.568	0.1	87.459	0.04
91U	100x100	WM	0.0167	3.7	0.6444	6.73	0.0648	39	7.098	0.2	34.419	0.11
91W	100x100	WM	0.0020	33.8	0.1960	22.08	0.2105	13	18.824	0.1	75.504	0.04
91X	100x100	WM	0.0028	20.2	0.0293	99.99	0.2388	16	21.127	0.1	82.518	0.04
91Y	100x100	WM	0.0028	21.0	0.0090	400.12	0.2143	12	17.441	0.1	76.909	0.04
92A	100x100	WM	0.0058	11.0	0.1488	24.06	0.2340	16	15.338	0.1	62.175	0.06
92B	50x50	WM	0.0018	39.3	-0.0020	2102.11	0.0960	27	7.453	0.2	34.365	0.10
92C	50x50	WM	0.0028	25.3	0.0346	109.15	0.0844	38	4.988	0.3	27.586	0.14
92I	50x50	WM	0.0005	147.8	0.0858	41.07	0.1262	32	6.193	0.2	24.261	0.14
92J	100x100	WM	0.0046	13.6	0.8148	5.25	0.0816	56	6.274	0.2	28.407	0.11
92K	100x100	WM	0.0065	11.0	0.0919	33.62	0.1593	29	8.537	0.2	35.208	0.11
92M	100x100	WM	0.0017	36.6	0.0800	36.18	0.1154	22	13.248	0.1	74.278	0.03
92N	100x100	WM	0.0061	11.7	0.1307	27.37	0.0170	160	8.739	0.2	35.247	0.10
92O	100x100	WM	0.0048	14.2	0.0321	110.57	0.1256	22	14.483	0.1	58.274	0.05
92Q	100x100	WM	0.0047	13.5	0.0426	68.20	0.1748	31	9.652	0.1	38.599	0.08
92R	~100x60	WM	0.0159	2.9	0.0242	118.97	0.0532	101	5.331	0.3	28.624	0.10
233C	100x100	WM	0.0006	110.1	0.3107	152.53	0.0480	105	3.539	0.4	17.350	0.38
233D	100x100	WM	0.0055	12.7	0.1102	479.74	0.0682	67	4.297	0.3	18.146	0.26
233F	100x100	WM	0.0070	9.0	0.4934	84.09	0.1544	16	10.329	0.2	46.358	0.11
233G	100x100	WM	0.0136	4.6	0.8773	48.81	0.0916	33	7.477	0.2	33.030	0.13
233I	100x100	Kfs?	0.0088	7.7	0.2768	133.51	0.0498	117	3.924	0.3	25.830	0.16
233J	100x100	WM	0.0020	36.5	0.1174	293.60	0.1624	37	11.871	0.1	56.194	0.07
233M	100x100	Pl	0.0095	6.4	0.4393	104.78	0.0293	120	0.061	22.5	4.676	0.71
233N	100x100	WM	0.0048	12.2	0.0122	4607.78	0.1102	30	8.777	0.1	33.918	0.10
233Q	~200x65	WM	0.0121	6.8	0.4346	134.25	0.1012	30	5.969	0.2	27.104	0.15
233R	100x100	WM	0.0033	19.1	0.7987	66.68	0.2088	14	16.404	0.1	87.185	0.04
233T	100x100	WM	0.0037	19.5	-0.4818	147.98	0.1890	16	16.672	0.1	70.385	0.04
233V	100x100	WM	0.0017	44.8	-0.2066	306.22	0.1713	21	12.596	0.1	48.634	0.06
233X	100x100	WM	0.0039	16.5	0.3795	198.79	0.0960	30	7.591	0.1	30.554	0.14
233Y	100x100	WM	0.0024	19.3	0.1122	691.54	0.1275	22	8.286	0.2	32.666	0.12
234A	100x100	WM	0.0037	15.6	0.3115	196.46	0.1691	28	15.054	0.1	59.392	0.06
234B	~100x100	WM	0.0085	9.1	0.3768	169.12	0.2299	22	20.868	0.1	85.339	0.04
234H	100x100	WM	0.0005	161.6	0.3347	217.40	0.1527	27	9.937	0.2	38.595	0.09
234I	100x100	WM	0.0094	7.1	0.3371	153.37	0.2474	17	17.916	0.1	86.906	0.05
234K	160x60	Kfs?	-0.0011	64.4	0.5661	113.63	0.0066	775	1.747	0.9	11.537	0.33

$^{40}Ar^*/^{39}Ar_{(K)}$	±2σ	Age (Ma)	±2σ	$^{40}Ar^*$ (%)	$^{39}Ar_{(K)}$ (%)	K/Ca	±2σ				
3.5978	0.0453	**37.64**	**0.47**	94.2	3.5	1037	17864	1	WM	**37.64**	**0.47**
4.0420	0.0685	**42.24**	**0.71**	91.3	1.9	313	2440	2	WM	**37.75**	**0.52**
3.6285	0.0282	**37.96**	**0.29**	97.4	3.2	190	530	3	WM	**37.96**	**0.29**
3.6980	0.0399	**38.68**	**0.41**	98.9	2.3	157	421	4	WM	**37.99**	**0.43**
3.7133	0.0373	**38.84**	**0.39**	98.7	2.6	74	72	5	WM	**38.40**	**0.46**
3.7631	0.0302	**39.36**	**0.31**	98.8	3.3	287	1499	6	WM	**38.57**	**0.57**
4.1527	0.0363	**43.38**	**0.37**	96.5	2.7	2330	118378	7	WM	**38.68**	**0.41**
3.8946	0.0322	**40.71**	**0.33**	98.5	2.9	881	16831	8	WM	**38.70**	**0.56**
3.8071	0.0339	**39.81**	**0.35**	78.5	3.0	138	325	9	WM	**38.84**	**0.39**
3.8828	0.0343	**40.59**	**0.36**	55.7	3.6	498	3598	10	WM	**38.98**	**0.73**
3.7483	0.0366	**39.20**	**0.38**	98.2	2.5	78	125	11	WM	**39.20**	**0.38**
7.2462	0.0686	**75.03**	**0.70**	82.8	1.7	32	27	12	WM	**39.28**	**0.48**
4.1568	0.0402	**43.42**	**0.42**	98.2	3.1	1045	19342	13	WM	**39.36**	**0.31**
4.1453	0.0738	**43.31**	**0.76**	100.4	1.4	5	4	14	WM	**39.39**	**0.78**
4.1774	0.0396	**43.64**	**0.41**	98.0	2.2	31	112	15	WM	**39.60**	**0.61**
3.6080	0.0499	**37.75**	**0.52**	91.3	2.1	18	38	16	WM	**39.81**	**0.35**
3.8715	0.0478	**40.48**	**0.49**	93.1	2.1	66	641	17	WM	**39.94**	**0.54**
3.8192	0.0518	**39.94**	**0.54**	87.4	2.2	36	132	18	WM	**40.07**	**0.42**
5.8428	0.0758	**60.74**	**0.78**	101.6	1.6	-130	3264	19	WM	**40.48**	**0.49**
4.6632	0.0607	**48.64**	**0.62**	104.4	1.8	44	500	20	WM	**40.55**	**0.45**
4.0060	0.0580	**41.87**	**0.60**	93.1	1.6	24	138	21	WM	**40.59**	**0.36**
3.9829	0.0491	**41.63**	**0.51**	96.0	2.0	31	156	22	WM	**40.71**	**0.33**
13.6460	0.0459	**138.81**	**0.45**	94.2	3.0	11	8	23	WM	**40.75**	**0.53**
4.6045	0.0596	**48.04**	**0.61**	96.7	1.6	14	37	24	WM	**41.09**	**1.05**
4.8368	0.0529	**50.43**	**0.54**	100.8	1.7	25	103	25	WM	**41.56**	**0.72**
4.5725	0.0332	**47.71**	**0.34**	100.3	2.8	41	133	26	WM	**41.63**	**0.51**
6.1780	0.0483	**64.17**	**0.49**	98.0	2.4	86	958	27	WM	**41.87**	**0.60**
3.7271	0.0702	**38.98**	**0.73**	91.4	1.5	21	82	28	WM	**42.24**	**0.71**
5.0767	0.0585	**52.89**	**0.60**	90.2	1.6	6	8	29	WM	**42.45**	**0.93**
4.9551	0.0363	**51.64**	**0.37**	90.9	2.5	28	135	30	WM	**42.46**	**0.52**
4.8521	0.0563	**50.59**	**0.58**	85.5	1.5	8	15	31	WM	**43.31**	**0.76**
5.2667	0.1541	**54.84**	**1.58**	89.9	0.7	-62	1518	32	WM	**43.38**	**0.37**
4.9483	0.1040	**51.57**	**1.07**	89.7	1.0	-25	196	33	WM	**43.42**	**0.42**
3.6311	0.0411	**37.99**	**0.43**	98.5	2.1	47	363	34	WM	**43.64**	**0.41**
3.7664	0.0754	**39.39**	**0.78**	99.2	1.2	14	39	35	WM(±Kfs?)	**45.08**	**0.66**
3.6870	0.0548	**38.57**	**0.57**	87.4	1.7	53	567	36	WM(±Kfs?)	**47.71**	**0.34**
3.8325	0.0404	**40.07**	**0.42**	87.8	1.8	13	24	37	WM	**48.04**	**0.61**
3.7559	0.0467	**39.28**	**0.48**	102.2	1.7	30	177	38	Kfs	**48.64**	**0.62**
3.7002	0.0541	**38.70**	**0.56**	97.2	1.8	13	20	39	WM	**50.43**	**0.54**
3.6708	0.0442	**38.40**	**0.46**	96.8	2.2	31	102	40	Kfs?	**50.59**	**0.58**
3.8783	0.0440	**40.55**	**0.45**	94.7	1.9	29	167	41	Kfs	**51.57**	**1.07**
4.3172	0.0638	**45.08**	**0.66**	99.2	1.3	31	243	42	Kfs?	**51.64**	**0.37**
3.9760	0.0695	**41.56**	**0.72**	96.3	1.1	20	58	43	Kfs?	**52.89**	**0.60**
5.3576	0.0793	**55.78**	**0.81**	94.5	1.6	12	20	44	Kfs?	**54.84**	**1.58**
3.8977	0.0513	**40.75**	**0.53**	95.2	2.2	35	104	45	Kfs?	**55.78**	**0.81**
3.7868	0.0588	**39.60**	**0.61**	98.3	1.6	9	14	46	Kfs?	**60.74**	**0.78**
4.0630	0.0507	**42.46**	**0.52**	95.9	1.9	11	19	47	Kfs?	**64.17**	**0.49**
3.9310	0.1014	**41.09**	**1.05**	95.9	1.2	64	1142	48	Kfs?	**75.03**	**0.70**
4.0626	0.0899	**42.45**	**0.93**	94.6	1.2	23	91	49	Kfs	**138.81**	**0.45**

$^{40}Ar^*/^{39}Ar_{(K)}$	±2σ	Age (Ma)	±2σ	$^{40}Ar^*$ (%)	$^{39}Ar_{(K)}$ (%)	K/Ca	±2σ			
3.35	0.02	**35.12**	**0.25**	93.5	2.4	26.0	4.9	1		**32.50**	**0.22**
3.25	0.04	**34.03**	**0.38**	95.7	1.5	2490	59933	2		**33.08**	**0.46**
3.42	0.02	**35.87**	**0.16**	92.5	2.8	7.34	0.81	3		**33.33**	**0.29**
3.10	0.02	**32.50**	**0.22**	92.4	2.8	20.4	2.9	4		**33.35**	**0.28**
3.26	0.02	**34.13**	**0.22**	93.6	3.2	50	12	5		**33.68**	**0.23**
3.44	0.02	**36.04**	**0.18**	93.0	3.5	17.0	2.2	6		**33.73**	**0.19**
3.42	0.04	**35.84**	**0.43**	92.9	1.7	4.48	0.49	7		**34.03**	**0.38**
3.29	0.06	**34.51**	**0.58**	91.5	1.1	15.4	3.8	8		**34.09**	**0.18**
3.37	0.02	**35.28**	**0.26**	92.5	2.3	12.8	1.5	9		**34.13**	**0.22**
3.27	0.01	**34.29**	**0.15**	94.0	3.4	13.0	1.5	10		**34.15**	**0.20**
3.32	0.02	**34.83**	**0.22**	95.4	2.6	7.06	0.77	11		**34.19**	**0.26**
3.21	0.02	**33.68**	**0.23**	94.2	2.5	22.3	3.8	12		**34.19**	**0.24**
3.27	0.03	**34.32**	**0.32**	88.0	2.4	11.2	1.3	13		**34.29**	**0.15**
3.33	0.02	**34.85**	**0.17**	91.6	2.6	11.5	1.3	14		**34.32**	**0.32**

3.37	0.02	**35.29**	**0.20**	92.6	3.3	15.7	2.0	15	**34.36**	**0.27**
3.29	0.02	**34.45**	**0.18**	88.0	3.6	10.5	1.1	16	**34.45**	**0.18**
3.26	0.02	**34.19**	**0.26**	81.3	2.4	11.6	1.4	17	**34.51**	**0.58**
3.18	0.03	**33.35**	**0.28**	95.8	2.2	31.6	7.8	18	**34.65**	**0.15**
3.61	0.02	**37.81**	**0.26**	87.8	2.0	3.20	0.33	19	**34.83**	**0.22**
3.36	0.02	**35.22**	**0.22**	92.9	2.6	5.98	0.64	20	**34.84**	**0.40**
3.37	0.02	**35.27**	**0.20**	94.6	3.2	10.9	1.2	21	**34.85**	**0.17**
3.31	0.01	**34.65**	**0.15**	93.4	3.3	63	18	22	**34.91**	**0.44**
3.33	0.04	**34.91**	**0.44**	87.0	1.9	2.61	0.27	23	**35.02**	**0.26**
3.26	0.02	**34.15**	**0.20**	94.9	3.3	4.76	0.49	24	**35.02**	**0.21**
3.36	0.02	**35.22**	**0.16**	93.8	4.0	12.1	1.4			
3.25	0.02	**34.09**	**0.18**	88.6	3.5	4.12	0.42	25	**35.07**	**0.33**
3.34	0.02	**35.02**	**0.26**	92.7	2.4	3.11	0.32	26	**35.12**	**0.25**
3.51	0.03	**36.78**	**0.28**	92.7	2.0	2.02	0.20	27	**35.20**	**0.36**
4.13	0.17	**43.16**	**1.79**	91.6	0.4	2.4	5.1	28	**35.22**	**0.16**
3.36	0.03	**35.20**	**0.36**	91.5	1.3	3.1	1.7	29	**35.22**	**0.22**
3.32	0.04	**34.84**	**0.40**	95.3	1.3	8.5	12.6	30	**35.26**	**0.24**
3.18	0.03	**33.33**	**0.29**	93.5	2.0	4.7	3.4	31	**35.27**	**0.20**
3.36	0.02	**35.26**	**0.24**	94.0	2.6	12	19	32	**35.28**	**0.26**
3.39	0.02	**35.47**	**0.20**	91.6	2.5	9.6	6.5	33	**35.29**	**0.20**
3.42	0.03	**35.86**	**0.31**	86.2	1.3	5.9	4.4	34	**35.47**	**0.20**
3.15	0.04	**33.08**	**0.46**	94.9	1.3	19	99	35	**35.84**	**0.43**
3.26	0.02	**34.19**	**0.24**	94.8	2.4	53	352	36	**35.86**	**0.31**
3.34	2.85	**35.03**	**29.63**	7.6	0.0	0.7	5.9	37	**35.87**	**0.16**
3.28	0.03	**34.36**	**0.27**	85.9	2.1	4.0	2.0	38	**36.04**	**0.18**
3.22	0.02	**33.73**	**0.19**	89.9	3.2	10.3	10.3	39	**36.78**	**0.28**
3.35	0.03	**35.07**	**0.33**	86.4	1.5	7.3	11.3	40	**37.33**	**0.58**
3.34	0.02	**35.02**	**0.21**	81.6	2.8	8.3	4.3	41	**37.81**	**0.26**
3.57	0.06	**37.33**	**0.58**	92.8	0.8	17	112	42	**43.16**	**1.79**

$^{40}Ar^*/^{39}Ar_{(K)}$	±2σ	Age (Ma)	±2σ	$^{40}Ar^*$ (%)	$^{39}Ar_{(K)}$ (%)	K/Ca	±2σ
4.13	0.03	**43.12**	**0.33**	96.9	2.8	257	576
4.08	0.03	**42.68**	**0.34**	94.8	2.8	359	1568
3.91	0.03	**40.88**	**0.30**	99.5	4.0	455	1335
3.92	0.03	**41.05**	**0.33**	97.6	3.0	96	78
3.87	0.07	**40.45**	**0.67**	93.3	1.6	97	179
3.95	0.02	**41.30**	**0.22**	97.4	5.0	95	58
4.15	0.06	**43.32**	**0.57**	85.5	1.6	5.8	1.0
3.97	0.02	**41.52**	**0.23**	99.0	4.4	51	23
3.86	0.02	**40.34**	**0.18**	98.7	4.9	382	764
4.35	0.02	**45.46**	**0.22**	98.7	4.0	1021	8175
3.93	0.03	**41.12**	**0.27**	97.0	3.6	55	27
4.53	0.06	**47.28**	**0.62**	98.2	1.7	-1978	83151
5.36	0.09	**55.78**	**0.93**	96.8	1.2	76	167
3.88	0.08	**40.62**	**0.80**	99.1	1.4	38	32
4.31	0.06	**45.04**	**0.65**	95.2	1.5	4.08	0.59
3.89	0.05	**40.67**	**0.54**	94.3	2.0	49	33
5.56	0.03	**57.87**	**0.31**	99.2	3.1	88	64
3.82	0.05	**39.94**	**0.52**	94.7	2.0	35	20
3.92	0.03	**40.94**	**0.31**	97.3	3.4	239	529
3.84	0.04	**40.20**	**0.42**	96.1	2.2	120	164
4.47	0.06	**46.68**	**0.60**	83.3	1.2	117	277
4.85	0.12	**50.60**	**1.24**	99.0	0.8	6	18
3.83	0.10	**40.09**	**1.08**	90.8	1.0	21	198
4.28	0.04	**44.72**	**0.42**	95.4	2.4	11	19
3.88	0.05	**40.54**	**0.57**	87.7	1.7	4.5	4.4
5.91	0.11	**61.45**	**1.16**	89.8	0.9	8	20
4.68	0.04	**48.79**	**0.40**	98.8	2.8	54	315
31.22	15.41	**303.34**	**137.81**	40.3	0.0	0.07	0.16
3.69	0.04	**38.62**	**0.45**	95.5	2.0	383	35263
3.93	0.09	**41.10**	**0.90**	86.5	1.4	7	20
5.25	0.03	**54.69**	**0.27**	98.8	3.8	11	15
4.14	0.03	**43.30**	**0.29**	98.1	3.9	-18	54
3.81	0.04	**39.86**	**0.39**	98.7	2.9	-32	198
3.87	0.05	**40.45**	**0.56**	96.1	1.8	11	42
3.85	0.04	**40.25**	**0.41**	97.6	1.9	39	541
3.86	0.03	**40.42**	**0.26**	97.9	3.5	26	101
3.96	0.02	**41.40**	**0.24**	96.8	4.8	29	99
3.86	0.05	**40.41**	**0.49**	99.5	2.3	16	68
4.69	0.02	**48.90**	**0.26**	96.6	4.2	28	86
6.81	0.28	**70.62**	**2.84**	103.1	0.4	1.6	3.7

1	WM	**38.62**	**0.45**
2	WM	**39.86**	**0.39**
3	WM	**39.94**	**0.52**
4	WM	**40.09**	**1.08**
5	WM	**40.20**	**0.42**
6	WM	**40.25**	**0.41**
7	WM	**40.34**	**0.18**
8	WM	**40.41**	**0.49**
9	WM	**40.42**	**0.26**
10	WM	**40.45**	**0.67**
11	WM	**40.45**	**0.56**
12	WM	**40.54**	**0.57**
13	WM	**40.62**	**0.80**
14	WM	**40.67**	**0.54**
15	WM	**40.88**	**0.30**
16	WM	**40.94**	**0.31**
17	WM	**41.05**	**0.33**
18	WM	**41.10**	**0.90**
19	WM	**41.12**	**0.27**
20	WM	**41.30**	**0.22**
21	WM	**41.40**	**0.24**
22	WM	**41.52**	**0.23**
23	WM	**42.68**	**0.34**
24	WM	**43.12**	**0.33**
25	WM	**43.30**	**0.29**
26	WM	**43.32**	**0.57**
27	WM	**44.72**	**0.42**
28	WM	**45.04**	**0.65**
29	WM	**45.46**	**0.22**
30	WM	**46.68**	**0.60**
31	WM	**47.28**	**0.62**
32	WM	**48.79**	**0.40**
33	WM	**48.90**	**0.26**
34	WM	**50.60**	**1.24**
35	WM	**54.69**	**0.27**
36	WM	**55.78**	**0.93**
37	WM	**57.87**	**0.31**
38	Kfs?	**61.45**	**1.16**
39	Kfs?	**70.62**	**2.84**
40	Pl	**303.34**	**137.81**

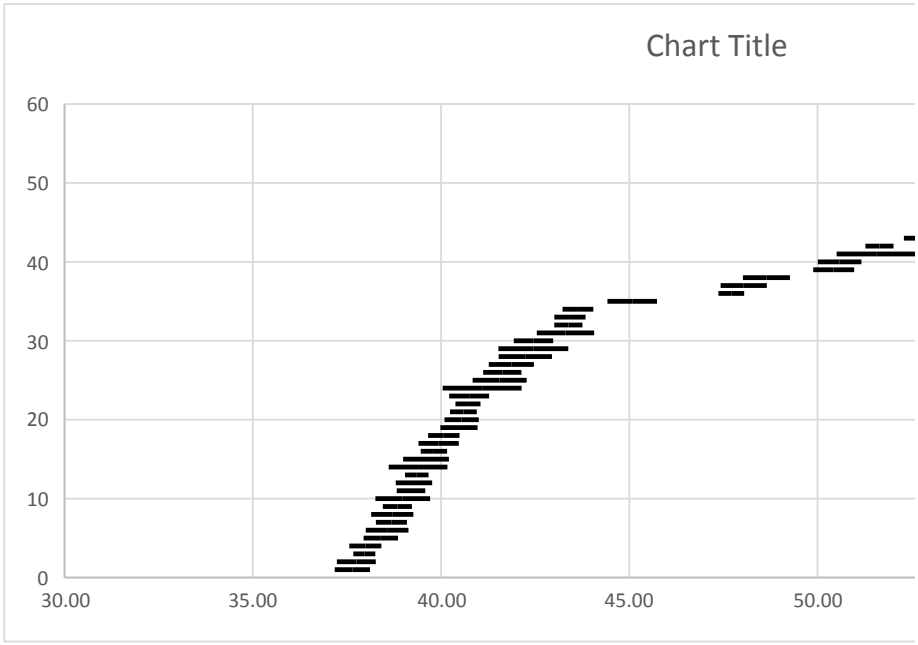
Chart Title
60
50
40
30
20
10
0
30.00
35.00
40.00
45.00
50.00

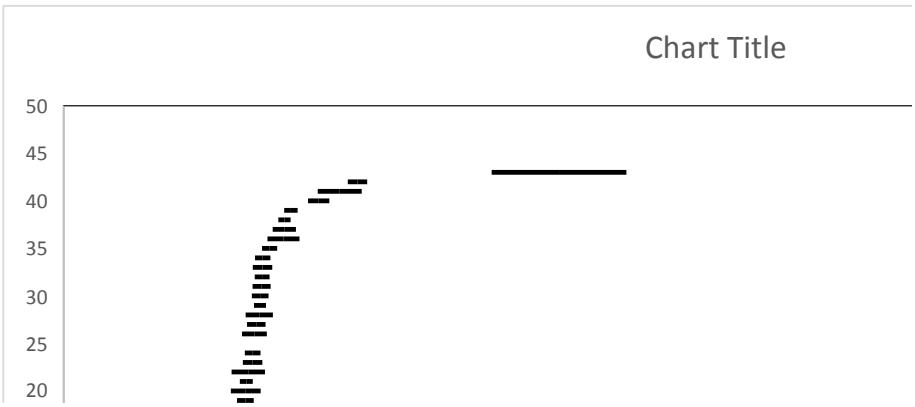
Chart Title
50
45
40
35
30
25
20

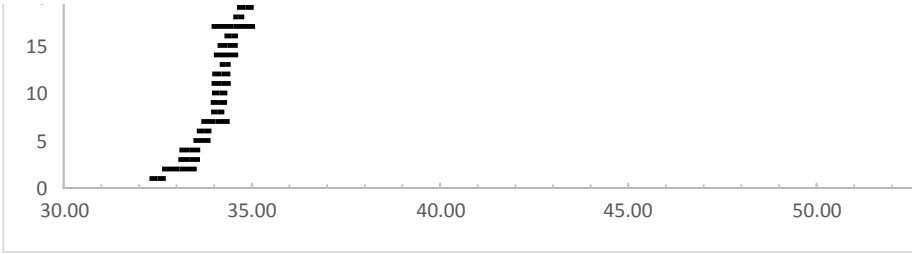
15
10
5
0
30.00
35.00
40.00
45.00
50.00

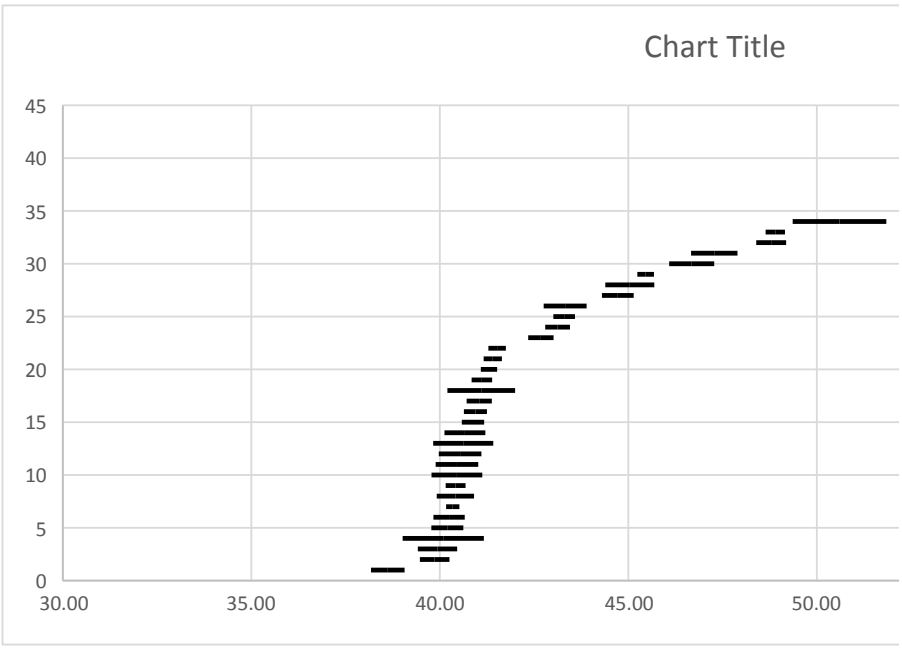
Chart Title
45
40
35
30
25
20
15
10
5
0
30.00
35.00
40.00
45.00
50.00

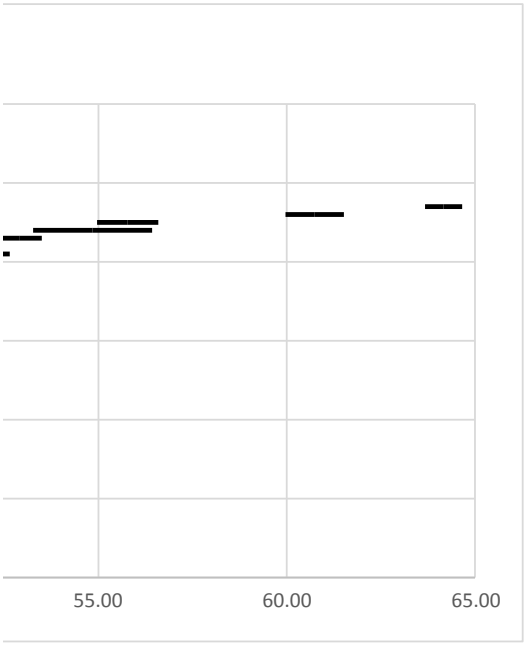
55.00
60.00
65.00

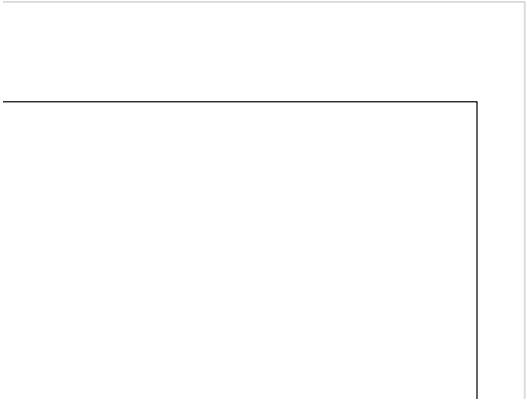

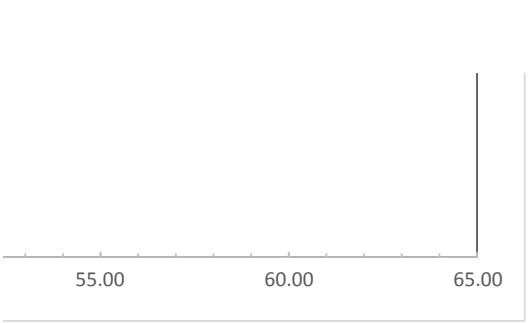
55.00
60.00
65.00

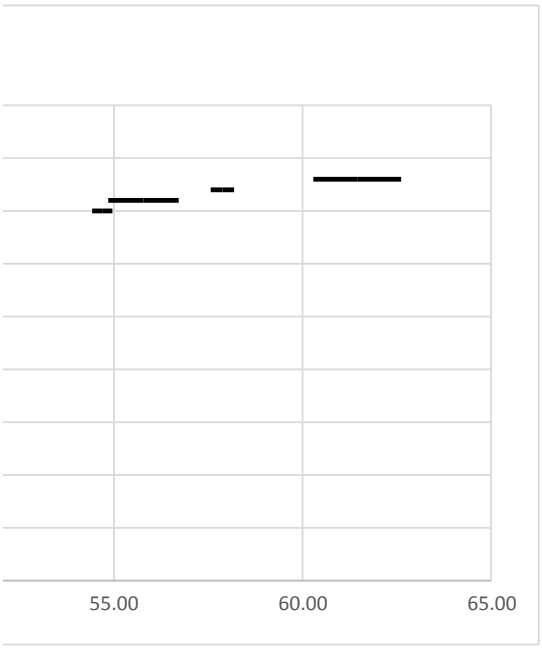
55.00
60.00
65.00